# Structure-directing effects in microheterogeneous ionic liquids

**DISSERTATION**

zur Erlangung des akademischen Grades

**Doctor Rerum Naturalium**

(Dr. rer. nat.)

an der Mathematisch-Naturwissenschaftlichen Fakultät

der Rheinischen Friedrich-Wilhelms-Universität Bonn

vorgelegt von

**M. Sc. Roman Elfgen**

aus Siegburg, Deutschland

Bonn, 2022

Angefertigt mit Genehmigung der Mathematisch-Naturwissenschaftlichen Fakultät der Rheinischen Friedrich-Wilhelms-Universität Bonn

---

| | |
|---|---|
| Erstgutachterin: | Prof. Dr. Barbara Kirchner |
| Zweitgutachter: | Prof. Dr. Thomas Bredow |
| Prüfungsdatum: | 20.12.2022 |
| Erscheinungsjahr: | 2023 |

*"What we know is a drop, what we don't know is an ocean."*

Isaac Newton

# Abstract

The man-made global climate change and contamination of the world's oceans with plastics demand for alternative sources and storage possibilities of energy, as well as for the development of more resource-efficient and sustainable procedures and materials. In that regard, the quest for alternative solvents and reaction media became of crucial importance, in particular to establish more efficient material synthesis routes and extraction processes. Ionic liquids (ILs) represent an interesting and promising material class with great potential to tackle these problems. The special properties of ILs are based on their molecular composition and resulting interactions between the particles. Despite the increasing number of studies in the field of ILs, their working principles at the molecular level are still far from being understood completely. State-of-the-art theoretical approaches, reaching from static calculations up to ab initio and classical molecular dynamics simulations, in combination with suitable analysis tools, are the methods of choice in order to gain a more detailed insight into the microscopic behavior of ILs.

This thesis focuses on the structural characterization of ILs and its potential for applications like the material synthesis in these solvents or their use as extractants for the removal of plastic nanoparticles from aqueous media. Thereby, much emphasis is placed on understanding the microheterogeneous structure, i.e. the segregation of polar and non-polar domains on the molecular level, and its impact and effects on the solvation of different molecules, as well as its potential to function as structure-directing or templating agents. In particular, the introduction of alkyl groups of different length leads to a tunability of the microheterogeneity and thus makes them promising candidates as potential reaction media and extractants.

In the first part, from carrying out an exhaustive theoretical study on a $Te_4Br_2$ molecule dissolved in two different ILs, one pure and the other mixed with $AlCl_3$, the IL's degree of microheterogeneity and the role of $AlCl_3$, their effects on the solvent structure and the

solvation of the $Te_4Br_2$ molecule, as well as the first steps of the reaction of the $Te_4Br_2$ molecule are elucidated. While, within the pure IL, a notable degree of microheterogeneity is observed, the $AlCl_3$-containing system is dominated by the formation of larger anionic species. For the $Te_4Br_2$ molecule dissolved in both ILs, significant Te-Br bond elongations compared to gas phase simulations are detected, inferring a solvation effect of the IL and a tendency towards the formation of a more ionic Te-Br species. However, only in the $AlCl_3$-containing system the $Te_4Br_2$ molecule undergoes a structural change upon the abstraction of a bromide ion and converts from an open form into a positively charged square-like species that is stabilized by the anionic Al-Cl-clusters.

In the second part, the microheterogeneity in ILs and its tunability are investigated in more detail, particularly with respect to its potential to act as template for selected solute molecules, i.e., *n*-butanol and *n*-dodecanol. It is observed that an elongation of the alkyl side chain attached to the cations of the IL leads to an increasing segregation of the non-polar from the polar moieties. Thereby, the cations order in a parallel way, confirming the tendency of microheterogeneous ILs to behave similar to surfactants in forming a non-spherical micelle-like structure. While the alcohol molecules tend to self-aggregate in the solvents with shorter side chains, they show a rising degree of dispersion when moving towards longer alkyl tails. Next to their association, the increasing order within the ILs comprising longer side chains is imprinted into the alignment of the alcohol molecules as well. In fact, the alkyl chain of the alcohol stretches out parallel to the alkyl groups of the IL cations, while their polar part anchors to the polar network of the IL. This behavior changes in degree, but does not dissipate when switching from *n*-dodecanol to *n*-butanol. Instead, the arrangement of the alcohol molecules is primarily determined by the structure of the IL itself, indicating an unambiguous template effect of the IL on the solute molecules solved in it.

Based on the findings from before, the third and last part deals with the question whether ILs are suitable solvents for the extraction of nanoplastic particles from aqueous media. By simulating a polyethylene nanoparticle in a set of ILs with varying anions and alkyl side chains of different length attached to the cations, it is found that the particle tends to disentangle into a loosely associated structure in order to increase its

contact surface area with the solvent. Thereby, the degree of disentanglement strongly depends on the degree of microheterogeneity present in the system. In contrast, within the non-polar molecular solvents tetrahydrofuran and toluene, the particle disintegrates into individual chains, indicating that by varying the side chain length and the anion of the IL the stability of the particles can be controlled and adjusted. By introducing polar units on the particles surface, which can in reality occur through natural oxidization processes, it is demonstrated that due to the amphiphilic nature of ILs these units can be solvated by suitable building blocks of the IL as well, implying that ILs should be capable of extracting plastic nanoparticles with varying complex structures. Modeling a phase transfer of a polyethylene nanoparticle from an aqueous to an IL phase reveals that this process is thermodynamically and kinetically favorable, indicating that employing ILs can indeed lead to promising processes to handle nanoplastic contamination.

# Contents

# Important abbreviations

| | |
|---|---|
| ADF | Angular distribution function |
| AIMD | Ab initio molecular dynamics |
| CC | Coupled cluster |
| CDF | Combined distribution function |
| CoM | Center of mass |
| CoR | Center of ring |
| $C_t/C_{term}$ | Terminal carbon atom |
| DDF | Distance distribution function |
| DF | Distribution function |
| DFT | Density functional theory |
| GGA | Generalized gradient approximation |
| GPW | Gaussian and plane waves |
| HF | Hartree-Fock |
| IL | Ionic liquid |
| LDA | Local density approximation |
| LJ | Lennard-Jones |
| MC | Monte-Carlo |
| MD | Molecular dynamics |
| MH | Microheterogeneity |
| MP | Møller-Plesset |
| NI | Number integral |
| PBC | Periodic boundary condition |
| PE | Polyethylene |
| PNP | Plastic nanoparticle |
| RDF | Radial distribution function |
| RTIL | Room-temperature ionic liquid |
| SCF | Self-consistent field |
| SDF | Spatial distribution function |
| SDG | Sustainable development goal |

# List of Figures

# List of Tables

# 1 Introduction

In 2015 the United Nations introduced 17 sustainable development goals (SDGs) to set an urgent call for action for all countries to build up global partnerships with the aim to develop new strategies that improve health and education, reduce inequality and spur economic growth, while tackling climate change and working to preserve the world's oceans and forests.[1] Besides many other important aspects, the SDGs tackle problems like the concerns about the long-term supply of fossil fuels and other resources like rare earth metals, the steadily rising air pollution with greenhouse gases and the increasing contamination of the oceans with plastics. All these man-made issues demand for alternative sources and storage possibilities of energy, as well as for the development of more resource-efficient and sustainable procedures and materials. Especially for the improvement or new development of energy devices like solar cells, batteries and super capacitors, or for establishing efficient extraction processes and less costly material synthesis routes, the quest for alternative solvents and reaction media became of crucial importance. In that regard, history has shown that the solution might not always lie in using a less toxic solvent, but in changing the way of its general working principles. Ionic liquids (ILs) provide an interesting and promising material class and have been shown to overcome a lot of issues related to conventional solvents. Thus, they have been the subject of enormous attention in recent years, both from scientific and technological points of view, and they also play the central role in this thesis.

The special properties of ionic liquids are based on their molecular composition and resulting interactions between the particles. Despite the growing number of studies in the field of ionic liquids, their working principle at the molecular level are still far from being understood completely, which is why further investigation is required. In that regard, state-of-the-art theoretical approaches, reaching from static calculation over ab initio molecular dynamics simulations up to classical molecular dynamics simulations

are the methods of choice in order to gain a more detailed insight into the microscopic behavior of ionic liquids that determine their macroscopic properties and eventually lead to advanced and sustainable applications.

To give a brief introduction into the topic of ionic liquids, the following section 1.1 deals with the fundamental aspects concerning these solvents, before taking into focus the great potential of the structure forming in distinct ILs (section 1.2), and tackling the question why theoretical methods are highly suitable to investigate such complex systems (section 1.3). Subsequently, the aim and scope of this thesis are introduced in section 1.4.

## 1.1 Ionic liquids – some basic aspects

As can be deduced from their name, ionic liquids are liquids that are entirely composed of mobile ions. The most simple ionic liquids are [A][X]-salts with a cation $[A]^+$ and an anion $[X]^-$, of which the cation is conventionally named first. Despite their ionic nature, these substances stand out due to their remarkable low melting point. This first unique property of ILs arises from the atomic structure, size, symmetry properties and the charge delocalization of the ions, which does not allow for forming a stable crystal lattice at moderate temperatures. One of the first ionic liquids, ethylammonium nitrate ($[EtNH_3][NO_3]$), with a melting point of only 12 °C, was synthesized by Walden in 1914.[2] Later in 1951, Hurley and Wier developed low-melting salts based on tetrachloroaluminate ($[AlCl_4]^-$) anions for the galvanization of aluminum.[3] During the 1970s and 1980s, these substances were mainly studied for electrochemical applications. In 1986, Fry and Pienta, as well as Boon, proposed ILs as solvents for the synthesis of organic substances.[4,5] In the 1990s, a criterion was introduced defining that the melting point of ionic liquids has to lie below 100 °C, which does not possess any physical meaning, but yet became popular, because it represents a condition under which the handling of ILs is much easier than the handling of substances that melt at higher temperatures. Moreover, it marks ionic liquids as promising and unique reaction media in terms of energy-saving. Many ILs even melt at ambient conditions and are henceforth denoted as room-temperature ionic liquids (RTILs). Up to today, the number of synthesized ionic liquids is steadily

increasing and the research in this area is further expanding. Earle and Seddon even estimated the number of existing low-melting salts to about one billion, so the potential to find a suitable IL for a specific application is nearly unlimited.[6]

In comparison to conventional organic solvents, the use of ionic liquids offers a multitude of advantages, which are determined by the combination of their special properties. In general ionic liquids possess a neglectable low vapor pressure, so they practically do not evaporate. This makes ILs suitable for the use in high-vacuum systems and at the same time it overcomes the issue of highly volatile substances that pollute the air and require costly ventilation techniques. Moreover, ionic liquids possess a wide liquid-range over up to 400 K, as well as a high thermal and electrochemical stability. They are miscible with substances of different polarity and can solve organic and inorganic substances, as well as unusual combinations of reagents and bring them into the same phase. These features offer many possibilities for the modification of already existing or the development of novel extraction processes. Another great potential poses the utilization of ILs for chemical syntheses and catalytic processes, because the charged nature as well as the IL structure can influence and control the reactions. Furthermore, mainly structural details in this context are presented separately in section 1.2.

The unique properties of ionic liquids are essentially based on the atomic composition of their building blocks and the interactions between them. ILs usually consist of large, asymmetric, organic cations with a high charge-delocalization and weakly basic, organic or inorganic anions. Most common are cations based on a heterocyclic ring structure, like imidazolium, pyridinum, pyrrolidinium or piperidinium systems, or simply a central phosphorus, nitrogen or sulfur atom (cf. Figure 1.1, blue highlighted part) with one or more alkyl side chains or otherwise functionalized groups attached to the ring structure or central atom (cf. Figure 1.1, red highlighted part). The anions are usually just halide ions, or contain halogen atoms, or are weakly basic organic compounds (cf. Figure 1.1, yellow highlighted part). Also certain anions can have functionalized groups attached to them. In addition to the forces present in conventional organic solvents, like hydrogen bonds, dipole-dipole and van der Waals forces, ILs possess attractive and repulsive electrostatic forces between the charged particles, making them miscible with polar substances. At

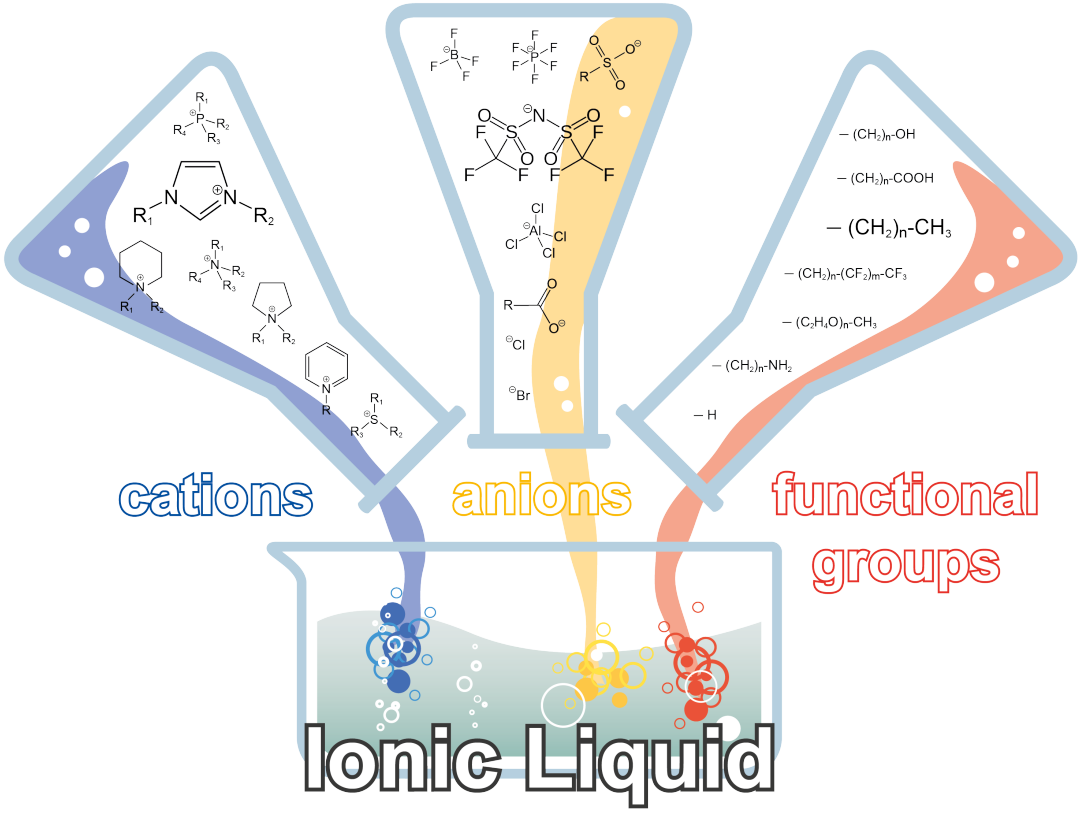


**Figure 1.1** Illustration of different building blocks of ionic liquids. Possible cations are highlighted in blue, anions in yellow. The letter R represents possible positions for the attachment of a functional group, for which some examples are depicted in red.

the same time, however, by adding non-polar groups like alkyl chains of different length, their ability of solving non-polar substances can be tuned. Due to the enormous number of possible combinations of cations, anions and additional functionalizations, the term "designer solvents" has been coined to describe the optimal adjustment of an ionic liquid for a desired application. Here, the independent choice of cations and anions determines the primary physico-chemical properties of the IL, while a functionalization usually serves as a fine-tuning parameter.

## 1.2 Microheterogeneity in ionic liquids

On the macroscopic level, ionic liquids consisting of $N$ particles and possessing a certain volume $V$ can usually be considered a homogeneous system with a uniform particle density

$\rho(r) = \frac{N}{V}$. On the molecular level, however, they show a clear structure, which has to be thoroughly characterized when aiming at fully understanding the ILs working principles and macroscopic properties. In the following, it is focused on a distinct structural motive, which arises from the introduction of alkyl side chains as functionalization, typically attached to the IL's cations. This makes the cation an amphiphilic molecule and leads to the segregation of the polar and non-polar units in the systems, due to the unfavorable mismatch of polar and non-polar groups, which rather tend to maximize the interactions to groups of their own chemical nature. Depending on the amount and size of these alkyl side chains, the non-polar units can form large non-polar domains within the otherwise polar medium. This phenomenon is denoted as microheterogeneity (MH).

The microheterogeneity in ionic liquids was externsively investigated in theoretical studies, in many cases with the help of molecular dynamics simulations.[7–15] In their study about the simulation of 1-butyl-3-methylimidazolium nitrate ($[C_4C_1Im][NO_3]$), using the coarse graining technique*, Wang and Voth could show that the presence of neutral side chains of the cations aggregate and form three-dimensional heterogeneous domains, whereas the charged headgroups of the cations and the anions are homogeneously distributed within the liquid due to the strong electrostatic interaction between them.[8] Later, Canongia Lopes and Pádua confirmed the formation of a microheterogeneous structure by analyzing 1-alkyl-3-methylimidazolium hexafluorophosphate ($[C_nC_1Im][PF_6]$) ILs with variating alkyl chain length. They showed, however, that the distribution of the charged units is not homogeneous, but instead they form a continuous three-dimensional network of ionic channels coexisting with the non-polar domains.[9] Here, the non-polar domains vary from evenly distributed, rather isolated microphases in the case of $[C_2C_1Im][PF_6]$ to larger connected phases in the case of $[C_{12}C_1Im][PF_6]$. In general, increasing the length of the side chain to longer than a butyl group results in the formation of continuous non-polar microphases. Experimental proof for the existence of nanoscale heterogeneities in ILs was provided in 2007 by Triolo et al., who performed

*Coarse graining represents a mesoscale modeling technique, where larger molecular units or even whole molecules are summarized in so-called *beads*. Due to the simplification, the accuracy of the molecule description is significantly reduced, as is the required computational effort. This technique is usually applied for the simulation of macromolecules, like for example polymers, proteins, liquid crystals, and so on.

X-ray diffraction experiments for 1-alkyl-3-methylimidazolium-based salts.[11] Moreover, it was found that the anions influence the MH as well,[12,15] as does the introduction of further side chain functionalizations. For example, side chain perfluorination increases the segregation behavior compared to their parent alkyl side chain analogues.[12,14,15] Since fluorous groups tend to segregate into a separate domain from both polar and non-polar units, their presence opens the possibility to build even three microphases. In this way, by adding long perfluorinated side chains to the anions, while simultaneously having cations with large alkyl groups, Triolo et al.,[16] and later Rebelo et al. created such "triphylic" ionic liquids.[17] The triphilicity can even be tuned by mixing ILs with alkyl and perfluoroalkyl side chains at the cations with different molar fractions.[14]

The self-organization in such ionic liquids arises from the diversity of intermolecular forces present in the system.[18,19] Thus, the polar and non-polar domains, respectively, possess their individual characteristics. While the polar domains are mostly governed by the strong electrostatic forces and show hydrogen bonding and dipole-dipole interactions, the non-polar domains are dominated by the weaker van der Waals and dispersive forces, which in sum can form a strong non-polar network as well (e.g. in the presence of long alkyl side chains).[20–25]

Based on this diversity of intermolecular interactions, Dupont coined the term "supramolecular fluids" in order to describe supraionic aggregates observed in ILs.[26] These features open new perspectives for the use of ILs as solvents, namely it highlights their ability to act as structure-directing agents or templates.[27] Such effects have already been discussed extensively for supramolecular systems, like template-assisted syntheses of rotaxanes, just to name one prominent example.[28,29] In general, a template possesses the function to organize other components of a system in a way that alternative reaction channels become possible, eventually leading to novel products that would not form as easily or at all without a template.[30] Thereby, structural information, which is initially stored in the template, is transferred to the product. Due to the structural motives forming in microheterogeneous ILs, the questions arise, if ILs are capable of acting as structure-directing agents or templates, and if so, how this property can be tuned and controlled and furthermore, how it can be used for specific applications.

In this context, structure-directing or template effects have been suggested, especially in the field of inorganic material synthesis.[27,31–33] Here, the IL ions were observed to incorporate into the forming solid state product, therefore leading to new materials through directing the structure during the synthesis.[33] For example, this phenomenon was found to occur during the synthesis of three-dimensional iodometallate networks,[34,35] zeolite-analogous compounds and metal-organic frameworks.[31,32] Due to the novelty in using ionic liquids as reaction media and at the same time as templates, Morris et al. proposed the term "ionothermal synthesis".[31,32] For this procedure, ILs with large organic cations are employed, which can directly act as templates to guide the synthesis pathway.

Another example where template effects might play a role is the liquid clathrate formation, which occurs upon mixing ILs with aromatic hydrocarbons.[36–38] In general, liquid clathrates are defined as liquid yet localized host-guest complexes that form due to associative interactions between the ionic liquid ions and the aromatic molecules.

The almost infinite variety of ionic liquids and the plethora of diverse interactions governing these materials, as well as the possibility to functionalize the ions to achieve a fine-tuning of their properties, constitute a completely different environment from that of conventional polar or non-polar molecular solvents. While some ILs are fully miscible with water, the introduction of non-polar groups that also leads to the formation of a microheterogeneous structure can make them sufficiently hydrophobic for applications in extracting substances from an aqueous phase.[39–41] In that regard, ILs have been successfully applied for separation and extraction processes of various different materials, reaching from small organic molecules to large bioactive compounds and from metal ions to metal complexes, with the potential to even increase extraction yields and purification factors as compared to those for traditional solvents.[42–51]

For the investigation of such complex phenomena, theoretical methods are ideal tools, because they allow for a direct insight into the microscopic level picture,[13] thus providing an in depth understanding of the governing structural features.

## 1.3 Theoretical methods to investigate ionic liquids

In general, there are many strong arguments for using computer-based methods to investigate chemical systems. For their simulation, no dangerous or toxic chemicals are needed, neither are tall, complex, sometimes dangerous (e.g., high pressures or temperatures) and expensive facilities. This makes computational chemistry a much more resource conserving, sustainable, and safer field of chemistry. What is needed in turn, however, is the availability of high-performance computation facilities[†] and suitable programs that are based on efficient algorithms. In that regard, the fast development and improvement of computers and, in particular, high-performance and massively parallel computation platforms[52,53] during the last few decades have opened up the possibility to apply more and more accurate methods for systems on larger time and size scales. Therefore, with respect to a "real" system, it became possible to provide more reliable predictions of the properties and governing processes of complex chemical systems, even under extreme conditions. Another reason for the high relevance of computational techniques, particularly in ionic liquid research, is of course the high number of possible ion combinations and IL mixtures, which makes an experimental investigation of different ILs suitable for any particular application extremely time-consuming.[13,54] Furthermore, from an experimental point of view, it is rather challenging to obtain structural information on liquids,[55] whereas atomistic simulations and calculations provide information on the molecular level, which is probably most important for drawing connections between structure, composition, and properties of ILs.[13,56,57] Thus, computational studies are of high value to guide the rational design of ILs for a given application.[58]

Among the existing methods, in this work, two molecular simulation types are employed, which have been steadily improved over the past decades and thus nowadays represent state-of-the-art tools that are widely used, especially for the investigation of complex liquid systems. Classical molecular dynamics (MD) simulations usually treat atoms as smallest units to build up the molecules and thus do not distinguish between nuclei and electrons. Instead, the intra- and intermolecular interactions are modeled via pre-defined

[†]Of course it has to be taken into consideration that such facilities are expensive, need space and demand for an efficient cooling system, which consumes a high amount of electric power.

potentials that contain different parameters which are atom-type-specific and have to be determined previously, mostly based on independent quantum chemical calculations or empirical data. Both the potentials and the parameters are summarized unter the term force field. Up to now, many elaborate force fields have been developed for the simulation of diverse molecular species, as well as for ionic liquids, for which in particular Canongia Lopes and Pádua have provided crucial contributions.[59–61] While on the one hand side the reduction in complexity for the description of the atoms allows for considering large systems consisting of several thousands of atoms (which is in many cases necessary to fully picture long-range effects like solvation or structure directing effects), it has the disadvantage on the other hand that changes in the electronic structure and thus chemical reactions cannot be captured in the course of the simulation. Ab initio molecular dynamics (AIMD) simulations explicitly treat the electronic structure problem by performing on-the-fly statical quantum mechanical calculations, for example based on density functional theory (DFT), hence, the electronic variables are considered as active degrees of freedom throughout the simulation and do not have to be parametrized beforehand. This allows for considering chemically complex systems in which the bonding pattern changes during the evolution of the system. Due to the higher complexity in the description of the system, of course a higher computational effort is required, which is why in the case of ab initio molecular dynamics simulations, usually only smaller system sizes compared to classical simulations can be afforded. Both methods, classical and ab initio molecular dynamics simulations, are introduced in more detail in chapter 2.

It can be seen that the choice of the simulation technique strongly depends on the type of information that is desired. With respect to ionic liquid research, classical molecular dynamics simulations using force fields have been mainly used to obtain a microscopic picture of both the liquid structure and the dynamics of the IL ions. Thereby, next to investigations to elucidate microheterogeneity,[7–10,12–15] this technique was also employed to understand ion pairing[62–64] and the ion pair and hydrogen bond dynamics in ILs,[25,65] as well as the solvation of lithium in the context of battery-research.[66–71]. AIMD simulations have also been used to investigate structural and dynamic properties of ILs, mainly with emphasis on short-range effects, providing even deeper insight and thus adding to the

knowledge obtained from classical MD simulations. [56,57,72–76] Moreover, this technique has been extensively employed to study spontaneous effects like the proton transfer, [77] or the structural diffusion (e.g. Grotthuss diffusion), mainly in protic ILs, [78] but also to investigate the absorption of gases like $CO_2$ and $SO_2$, [79–82] and to calculate spectroscopic properties like infrared, Raman and vibrational circular dichroism intensities for different kinds of ionic liquids and IL-mixtures. [83–85]

Another crucial point that follows directly is the question of how to gather the desired information from the simulation. For this purpose, the trajectory analyzer and visualizer tool TRAVIS has been developed in the Kirchner working group, [86,87] offering a multitude of different advanced analysis functions of which the ones most relevant for this work are described in more detail in chapter 2.

## 1.4 Aim and scope of this thesis

As mentioned before, there is an immense variation in the physicochemical properties of ILs based on the chemical nature of the constituent ions. Although a large number of structure-property relationships have already been established for some ILs and IL-mixtures, through both experimental and computational investigations, fully understanding their working principles on the molecular level and further optimizing suitable IL-based materials for a given application are still extremely important fields of research. Thus, the results collected for and explicated in this thesis aim to further elucidate the diverse interactions governing ILs that lead to their special structural properties and to establish a general understanding of how to tune these structural features for their application-oriented adjustment. For this purpose, state-of-the-art ab initio and classical molecular dynamics simulations are employed in combination with selected and suitable analysis tools.

The main objectives of this thesis are divided into three parts: the first part deals with a concrete example for the near room-temperature material synthesis in ionic liquids. Based on an according experimental setup, the simulation of a $Te_4Br_2$ molecule, solved in either pure 1-ethyl-3-methylimidazolium chloride ($[C_2C_1Im][Cl]$) or the 1-ethyl-

3-methylimidazolium chloride/aluminum chloride mixture ($[C_2C_1Im][Cl]\cdot 1.3AlCl_3$), is performed with the aim to elucidate the complex solvent structure, including the IL's degree of microheterogeneity and the role of $AlCl_3$, as well as their effects on the solvation of the $Te_4Br_2$ molecule. By performing AIMD simulations, it is moreover possible to investigate the first steps of the reaction of the $Te_4Br_2$ molecule to eventually form the desired $Te_2Br$ material.

The second part comprises an extended and systematic study on the microheterogeneity in ionic liquids and its potential to function as structure-directing motive or template for selected solute molecules. By conducting classical MD simulations on the imidazolium based ILs 1-alkyl-3-methylimidazolium bis(trifluoromethylsulfonyl)imide considering ethyl, butyl, hexyl and octyl side chains attached to the cations ($[C_xC_1Im][NTf_2]$, x = 2, 4, 6, 8), mixed with either *n*-dodecanol or *n*-butanol, and using selected and suitable analysis tools, it is possible to reveal the correlation between the IL's degree of microheterogeneity and its potential to function as a template.

Lastly, in the third part, it is investigated in a systematic manner, whether the amphiphilic nature of selected ILs, which also leads to the formation of a microheterogeneous structure, can be used for the extraction of plastic nanoparticles from aqueous media. To do so, as a first step, classical MD simulations are carried out on pristine and oxidized polyethylene nanoparticles (consisting of 16 $C_{72}H_{144}$ chains) solved in 1-alkyl-3-methylimidazolium bis(trifluoromethylsulfonyl)imide considering ethyl, butyl, hexyl and octyl side chains attached to the cations ($[C_xC_1Im][NTf_2]$, x = 2, 4, 6, 8) and 1-alkyl-3-methylimidazolium tetrafluoroborate with either ethyl or octyl groups attached to the cations ($[C_xC_1Im][BF_4]$, x = 2, 8). In order to gain a general understanding of the particle's interactions with different potential extraction media, these simulations are compared to simulations of a pristine polyethylene particle in solvents of different polarity. In a second step, an extraction process is modeled by simulating the phase transfer of a polyethylene nanoparticle from an aqueous phase to an IL phase (either $[C_2C_1Im][NTf_2]$ or $[C_8C_1Im][NTf_2]$), serving to reveal the thermodynamics and mechanism of this process.

# 2 Methodology

The accurate simulation of complex chemical systems governing a multitude of molecular interactions is steadily developing as an interdisciplinary field that combines the theoretical fundamentals of chemistry and computer science. Thereby, computational calculations can add deeper insight into — resulting in a better understanding of — experimental findings, which are in turn needed in order to validate and improve the underlying models. For the scope of this thesis two simulation techniques play a major role: classical molecular dynamics and ab initio molecular dynamics. As it can already be deduced from their names, both methods share many basic principles, but differ significantly in the description of the interatomic interactions of a system, which is directly related to their individual strengths and weaknesses.

Classical MD simulations typically consider atoms as smallest units to compose the molecules in a system and use predefined potentials and parameters, either based on independent quantum chemical calculations or empirical data, to describe the interactions between the atoms. Usually, the overall interaction is decomposed into intra- and intermolecular terms, which have to be represented by suitable functional forms. After several decades of extensive research, very elaborate interaction models are accessible nowadays, making classical MD simulations an overwhelmingly successful tool, especially for the simulation of large many-body condensed matter systems.[9,13,14,47,57,64,88] The atomistic point of view and the need to construct fixed, predefined potentials, however, is accompanied by serious drawbacks: i) systems possessing many different atom and molecule types give rise to a myriad of different interactions that have to be parametrized, ii) changes in the electronic structure and, thus, the bonding pattern of a system can not be captured in the course of the simulation and iii) parameters specifically elaborated for a certain species are not necessarily transferable to another system, typically leading to an enormous effort to adjust or newly parametrize the potentials.

In that regard, AIMD simulations add great value to the field of realistic computer simulations.[52,53,77–79,83–85] The basic idea here is to compute the forces acting on the particles from electronic structure calculations that are performed on-the-fly as the molecular dynamics trajectory is generated. Thus, the electronic variables are not included beforehand by parametrized potentials, but they are considered as active degrees of freedom throughout the simulation. In this way, given that suitable approximate solutions to the many-electron problem are available, also chemically complex systems, in which the electronic structure changes during the temporal evolution of the system, can be easily handled. This, however, shifts the approximation from the level of devising an interaction potential to selecting a particular approximation for solving the Schrödinger equation. Therefore, due to an increased computational effort, usually only smaller systems as compared to classical MD simulations can be afforded.

The basics of both simulation techniques are elucidated in the following two sections, starting with their derivation from quantum mechanics (section 2.1) and then moving over to the fundamental aspects of molecular simulations (section 2.2), including a general introduction into molecular dynamics (subsection 2.2.1) before differentiating the treatment of interactions, so opposing classical (subsection 2.2.2) and ab initio (subsection 2.2.3) simulations. Further simulation details are discussed in section 7.1 in the appendix.

Subsequently, it has to be discussed how to properly analyze molecular dynamics trajectories. Here, special attention is put on the investigation of structural properties (section 2.3), focusing on three analysis tools in more detail: radial distribution functions (section 2.3.1), spatial distribution functions (section 2.3.2) and the domain analysis (section 2.3.3).

## 2.1 Starting from quantum mechanics

### 2.1.1 The Schrödinger equation

The theory of quantum mechanics leads back to the time-dependent Schrödinger equation, which was formulated by Erwin Schrödinger and first published in 1926.[89] The first

representation of this equation is a linear partial differential equation of second order and is today denoted as the fundamental equation of quantum mechanics. For the easy case of a hydrogen atom its form is:

$$i\hbar\frac{\partial}{\partial t}\Psi(r,t) = \left(-\frac{\hbar^2}{2m}\Delta + \hat{U}(r,t)\right)\Psi(r,t). \tag{2.1}$$

Here, $\hbar = \frac{h}{2\pi}$, with the Planck's constant $h \approx 6.626 \cdot 10^{-34}$ Js, $m$ is the mass of a particle, $r$ its position, $\hat{U}$ is the potential energy operator, $\Delta$ the Laplacian operator and $t$ is the time. The complex valued solution $\Psi(r,t)$ is called wavefunction. The so-called Hamiltonian

$$\hat{H}(r,t) = -\frac{\hbar^2}{2m}\Delta + \hat{U}(r,t) \tag{2.2}$$

determines the dynamics and the possible energies of the system. For the Hamiltonian of a system composed of $N$ particles it further applies:

$$\hat{H} = \hat{K} + \hat{U}, \tag{2.3}$$

where $\hat{K} = \sum_{i=1}^{N} \frac{\hbar^2}{2m_i}\Delta_i$ is the operator for the kinetic energy and $\hat{U} = \sum_{i=1}^{N}\sum_{j>i}^{N}\hat{U}_{ij}$ is the operator for the potential energy in the system. Here, index $i$ refers to a single particle and index $ij$ refers to the interaction of two particles $i$ and $j$. In general, the Schrödinger equation describes the behavior of a quantum mechanical system. If the Hamiltonian is independent of time, so for $\bar{H}(r,t) = \bar{H}(r)$, together with the variable separation $\Psi(r,t) = \Phi(r)\exp(-iEt/h)$, the time-independent Schrödinger equation results:

$$\hat{H}(r)\Phi(r) = E\Phi(r). \tag{2.4}$$

This equation describes the wave-particle duality of the electrons. The time-dependent factor $\exp(-iEt/h)$ is a phase factor. Equation 2.4 represents an eigenvalue problem with $E$ being the energy eigenvalues and $\Phi(r)$ the according eigenfunctions. The solutions $\Psi$ are initially not physically interpretable. Through normalization, however,

$$\int_{\mathbb{R}^3} |\Psi(r,t)|^2 d^3r = 1, \tag{2.5}$$

the probability for finding a particle at a certain point in space $r$, $|\Psi|^2$, is obtained.

Unfortunately, the Schrödinger equation is only solvable exactly for very easy potentials and also only for simple particles, like the hydrogen atom. If the Hamiltonian and the solution of the Schrödinger equation was known for any given system, then any approximation model would be needless. In reality, however, this is not the case; practically it is impossible to only approximatively solve the Schrödinger equation for 'larger' systems, i.e., for systems consisting of several hundred atoms. Moreover, in quantum mechanics all nuclei and electrons of a system must be considered.

The first approximation of the Schrödinger equation leads back to Born and Oppenheimer in 1927. The Born–Oppenheimer approximation is based on the assumption to separate the movement of the atomic nuclei and electrons from each other:

$$\Psi_{\text{tot}} = \Phi_n(R)\Phi_e(R,r), \tag{2.6}$$

where $n$ stands for the nuclei and $e$ for the electrons. $R$ represents the positions of the nuclei and $r$ the positions of the electrons. The approximation approach consists of two steps:

i) The configuration of the nuclei is fixed and only the electronic Schrödinger equation

$$\hat{H}_e\Phi_e(R,r) = E_e(R)\Phi_e(R,r) \tag{2.7}$$

is solved. Based on equation 2.3, the same is valid for the Hamiltonian:

$$\hat{H}_{\text{tot}} = \hat{H}_e + \hat{K}_n,\ \hat{H}_e = \hat{K}_e + \hat{U}_{nn} + \hat{U}_{ne} + \hat{U}_{ee}. \tag{2.8}$$

Thus, the kinetic energy with respect to the nuclei $\hat{K}_n$ is subtracted from $\hat{H}_{\text{tot}}$.

ii) Now $\hat{K}_n$ is introduced again to yield the nuclear Schrödinger equation:

$$(\hat{K}_n + E_e(R))\Phi_n(R) = E_{\text{tot}}\Phi_n(R) = \hat{H}_{\text{tot}}\Phi_n(R). \tag{2.9}$$

The solutions to equation 2.9 are so-called energy hyper-surfaces, which describe the po-

tential energy in dependence of the positions of all nuclei. The calculation of such energy hyper-surfaces and wavefunctions using quantum mechanical methods represents its own scientific field. In that regard a multitude of different approaches exits to reduce the corresponding high computational effort: the Hartree–Fock (HF) method considers interactions between one electron and an electron 'cloud' instead of interactions between single atoms.[90] The Møller–Plesset (MP) method improves on the HF method by adding electron correlation effects by means of Rayleigh—Schrödinger perturbation theory, usually to second (MP2), third (MP3) or fourth (MP4) order.[91] Accordingly, the computational effort required for the MP-techniques is much higher as compared to the HF technique, but of course much higher accuracy can be achieved. For Coupled-Cluster (CC) methods, the wavefunction is approximated by a series of exponential functions.[92] The first non-constant element of the series describes single excitations, the second one double excitations, the third one triple excitations of electrons and so on. The more excitations are included, the more accurate the method. However, excitations higher than double excitations can be neglected in many cases.

### 2.1.2 Density functional theory

A further group of very sophisticated methods to solve the electronic structure problem can be summarized under the term density functional theory (DFT). Using DFT, a good compromise between computational effort and accuracy can be achieved. This group of methods is based on the seminal work by Hohenberg and Kohn,[93] in which they present two theorems that originally hold for non-degenerate ground states.

The first Hohenberg–Kohn theorem shows that the ground state electronic energy and further electronic properties, as well as the wave function can be uniquely determined by the electron density $\rho$, which is solely dependent on the three spatial coordinates $x$, $y$ and $z$, regardless of the number of electrons or their spin-coordinates, thus reducing the many-body problem. Based on this, and in analogy to the electronic Hamiltonian $\hat{H}_e$ introduced in equations 2.7 and 2.8, the electronic energy can be rewritten as a functional

of the electron density $\rho(r)$:

$$E[\rho(r)] = K[\rho(r)] + U_{ee}[\rho(r)] + U_n[\rho(r)],\ U_n[\rho(r)] = \int \rho(r)\upsilon_{\text{ext}}(r)\mathrm{d}r. \tag{2.10}$$

It can be seen that only $U_n[\rho(r)]$ depends on the nuclear coordinates, since it comprises the attractive Coulombic interaction between the nuclei $R$ and electrons $r$ as well as the nuclear Coulomb repulsion, expressed by the external potential $\upsilon_{\text{ext}}(r)$:

$$\upsilon_{\text{ext}}(r) = \frac{e^2}{4\pi\varepsilon_0}\left(-\sum_{i=1}^{N-1}\frac{q_i}{|r-R_i|} + \sum_{i=1}^{N-1}\sum_{j=i+1}^{N}\frac{q_i q_j}{|R_i - R_j|}\right), \tag{2.11}$$

with the nuclear charges $q_i$ and $q_j$, $i,j = 1,...,N$ and the vacuum permittivity $\varepsilon_0 \approx 8.854 \cdot 10^{-12}$ Fm$^{-1}$. The two functionals $K[\rho(r)]$ and $U_{ee}[\rho(r)]$, representing the kinetic energy and the electron-electron interaction, respectively, are valid for any system and thus universal expressions, whose general forms remain unknown for now.

The second Hohenberg–Kohn theorem introduces the variational principle to DFT, according to which the energy of any trial electron density can not be lower than the exact ground state energy. It is hence possible to calculate the ground state energy by varying a trial electron density until the energy of a system reaches the global minimum. Unfortunately, the Hohenberg–Kohn theorems do not provide any way to do so, which is why they were further developed by Kohn and Sham.[94] Up to now the Kohn–Sham method represents a widely used approach in the field of DFT. It is based on the consideration of a fictive reference system consisting of non-interacting electrons, possessing the same electron density $\rho_{\text{ref}}(r)$ as the system with interacting electrons. Therein, the non-interacting electrons occupy so-called Kohn–Sham orbitals $\theta_i(r)$, and the electron density can be determined according to:

$$\rho_{\text{ref}}(r) = \rho(r) = e\sum_{i=1}^{N}|\theta_i(r)|^2. \tag{2.12}$$

Since a system's overall wave function is exactly given by a single Slater-determinant of the Kohn–Sham orbitals, the kinetic energy of the reference system $K_{\text{ref}}[\{\theta_i(r)\}]$ is

calculated according to:

$$K_{\mathrm{ref}}[\{\theta_i(r)\}] = -\frac{\hbar^2}{2m_e}\sum_{i=1}^{N}\langle\theta_i(r)|\nabla^2|\theta_i(r)\rangle, \tag{2.13}$$

with the mass of an electron $m_e$. As a next step the classical Coulomb repulsion

$$J[\rho(r)] = \frac{1}{4\pi\varepsilon_0}\frac{1}{2}\iint\frac{\rho(r_1)\rho(r_2)}{|r_1 - r_2|}\mathrm{d}r_1\mathrm{d}r_2 \tag{2.14}$$

is separated from the electron-electron interaction $U_{ee}[\rho(r)]$, to yield the final expression for the electronic energy:

$$E[\{\theta_i(r)\}] = K_{\mathrm{ref}}[\{\theta_i(r)\}] + J[\rho(r)] + E_{\mathrm{XC}}[\rho(r)] + U_n[\rho(r)]. \tag{2.15}$$

Here, the exchange-correlation functional $E_{\mathrm{XC}}[\rho(r)]$ includes all unknown contributions to the energy, concerning the electron-electron interactions, namely the kinetic correlation energy, the exchange energy, the Coulombic correlation energy and a self-interaction correction part.

According to the second Hohenberg–Kohn theorem from above, the Kohn–Sham orbitals are determined by minimizing the electronic energy with respect to the orbitals. Therefore, however, the orbitals have to be orthonormal. Applying the Lagrange multiplier method leads to the Kohn–Sham equation:

$$\left(-\frac{\hbar^2}{2m_e}\nabla^2 + \upsilon_{\mathrm{ext}}(r) + \frac{1}{4\pi\varepsilon_0}\int\frac{\rho(r_1)}{|r - r_1|}\mathrm{d}r_1 + \frac{\delta E_{\mathrm{XC}}[\rho(r)]}{\delta\rho(r)}\right)\theta_i(r) = \epsilon_i\theta_i(r), \tag{2.16}$$

where $\epsilon_i$ represents to orbital energies. Due to the fact that $J[\rho(r)]$ and $E_{\mathrm{XC}}[\rho(r)]$ depend on the orbitals through the electron density, the Kohn–Sham equations are non-linear and thus usually solved iteratively.

A crucial point in DFT represents the accurate determination of the exchange-correlation functional $E_{\mathrm{XC}}[\rho(r)]$, which is hitherto unknown. For this purpose, approximations have to be made for which the functional is typically divided into an exchange

and a correlation part:

$$E_{\mathrm{XC}}[\rho(r)] = E_{\mathrm{X}}[\rho(r)] + E_{\mathrm{C}}[\rho(r)]. \tag{2.17}$$

In principle the exchange part could be evaluated analog to the Hartree–Fock method using the Kohn–Sham orbitals, but combined with approximations for the correlation part, the exact exchange often yields only poor results for molecular properties. Thus, other techniques are used, which are in general based on successful error-cancellation approaches and furthermore avoid the demanding evaluation of exchange integrals.

Over the years many popular families of techniques to model the exchange-correlation energy have been developed, some of which are introduced briefly in the following.

Local density approximation (LDA) methods are based on the assumption that the electron density is a function that changes only marginally, so it can be locally treated as an uniform electron gas.[95,96] In this way, an exact expression for the calculation of the exchange energy can be derived, while for the correlation energy, it is impossible to find an analytic expression, even for simple systems. In the latter case, performing Monte Carlo (MC) simulations,[97,98] using fitting functions,[99] or neglecting the correlation part and adjusting prefactors in the exchange energy calculation[100] can yield better agreement with experimental results. Moreover, using the extended local spin density approximation (LSDA), open-shell systems can be treated as well.[99,100]

Since the consideration of an uniform electron gas does not provide an ideal description of molecular systems, more advanced functionals deal with the gradient of the electron density and are therefore denoted as generalized gradient approximation (GGA) techniques. Prominent examples in that regard are the Becke (B) exchange functional[101] and the Lee/Yang/Parr (LYP) correlation functional,[102] which contain empirical parameters fitted to the Hartree–Fock data for noble gases. Both functionals are commonly combined to yield the exchange-correlation functional BLYP. Other examples are the Perdew/Wang (PW91) exchange-correlation functional[103] and its successor, the Perdew/Burke/Ernzerhof (PBE) functional,[104] which are free of empirical parameters. The Tao/Perdew/Staroverov/Scuseria (TPSS) exchange-correlation functional[105] deals with higher derivatives of the electron density and thus represents an extension of the standard GGA functionals,

denoted as meta-GGA technique.

As stated before, it is also possible to use the Kohn–Sham orbitals in order to determine the exchange part as it is done in Hartree–Fock theory. For a system of non-interacting electrons this would provide the exact exchange-correlation energy, since there is no correlation energy. Based on this, so-called hybrid functionals use the exact HF-exchange for a part of the exchange-correlation energy, while the remaining parts are calculated using the functionals introduced above. The resulting hybrid functionals usually differ in the amount of exact exchange taken into account, which therefore constitutes another empirical parameter. Very popular are the Becke three-parameter functionals (B3):[106] The original one is based on the B exchange part and the PW91 correlation part. Later the PW91 correlation was replaced by the LYP analogon, creating the nowadays widely applied B3LYP hybrid functional.[107] In the same way, the PBE0 functional has been developed as a hybrid version of PBE,[108] however, in contrast to B3LYP, with a fixed amount of exact exchange, so again without any parameters fitted to experimental data. Also hybrid versions of meta-GGA functionals, such as TPSSh evolved from its non-hybrid successor.[109]

Another crucial point for all exchange-correlation functionals in the framework of DFT is the lack of a proper description of dispersion interactions. Besides some approaches like, e.g., the usage of non-local van der Waals functionals[110,111] or dispersion-corrected atom-centered potentials,[112,113] the DFT-D method and its extensions represent the most commonly used ones.[114–116] In DFT-D an empirical correction term $E_{\mathrm{disp}}$ is added to the final energy of the system:

$$E_{\mathrm{disp}} = -\sum_{i=1}^{N}\sum_{j=i+1}^{N}\sum_{n=6,8,10,\ldots} s_n \frac{C_n^{ij}}{r_n^{ij}} f_{\mathrm{damp}}(r_{ij}), \quad i,j = 1,...,N. \tag{2.18}$$

Here, the sum over all atom pairs $ij$ is taken, $C_n^{ij}$ is the n$^{\mathrm{th}}$-order dispersion coefficient for the pair $ij$, $r_{ij} = |R_i - R_j|$ is the distance between atoms $i$ and $j$, $s_n$ represents a global scaling factor which is adjusted to the underlying exchange-correlation functional and $f_{\mathrm{damp}}$ is a so-called damping function serving to avoid small-distance singularities and double-counting effects at intermediate distances.[116] In case of DFT-D3, the sum

over $n$ (cf. equation 2.18) is truncated after $n = 8$ and the dispersion coefficients $C_n^{ij}$ are determined via time-dependent density functional theory (TD-DTF).[115]

As a final building block for understanding the entire DFT procedure, it has to be clarified how to properly solve the Kohn–Sham equations (2.16). This is usually achieved by expressing the Kohn–Sham orbitals $\theta_i(r)$ as linear combinations of a finite set of $n$ predefined basis functions $\phi_i(r)$:

$$\theta_i(r) = \sum_{j=1}^{n} C_{ij}\phi_j(r). \tag{2.19}$$

Based on this the Kohn–Sham equations can be transformed from their differential form (cf. equation 2.16) into an according matrix representation:

$$\mathrm{KC} = \mathrm{SC}\epsilon. \tag{2.20}$$

Here, K is the Kohn–Sham matrix possessing the elements:

$$\left\langle \phi_i(r) \left| -\frac{\hbar^2}{2m_e}\nabla^2 + \upsilon_{\mathrm{ext}}(r) + \frac{1}{4\pi\varepsilon_0}\int \frac{\rho(r_1)}{|r - r_1|}\mathrm{d}r_1 + \frac{\delta E_{\mathrm{XC}}[\rho(r)]}{\delta\rho(r)} \right| \phi_i(r) \right\rangle, \tag{2.21}$$

S is the so-called overlap matrix with the elements:

$$S_{ij} = \langle \phi_i(r) | \phi_j(r) \rangle, \tag{2.22}$$

C is the matrix of the coefficients from the basis expansion displayed in equation 2.19 and $\epsilon$ is a diagonal matrix containing the orbital energies $\epsilon_i$ on its main diagonal. Following this approach, the task of determining the Kohn–Sham orbitals is broken down to finding the suitable coefficients $C_{ij}$. Equation 2.20 represents a typical eigenvalue problem, however, since the Kohn–Sham matrix K is dependent on the coefficients C, an iterative procedure is required. To do so, the coefficients C are initially guessed to evaluate the Kohn–Sham matrix K, and then new coefficients are calculated via solving the eigenvalue problem to evaluate the new Kohn–Sham matrix and so on, until a certain threshold is reached beyond which the change in the coefficients is so small that it can be tolerated with respect

to the accuracy of the desired properties to be calculated. Due to the self-consistency of this approach the procedure is denoted as self-consistent field (SCF) method.

Severals different types of basis functions $\phi_i(r)$ have been proposed so far, with Gaussian type orbitals (GTOs) being probably the most frequently used ones in the field of quantum chemistry. Their general form tries to mimic the atomic orbitals of individual atoms and thus can be written as:

$$\phi(r) = N\xi(r - r_0) \sum_{k=1}^{m} d_k \exp\left(-\zeta_k |r - r_0|^2\right), \tag{2.23}$$

with the normalization constant $N$, the term $\xi(r - r_0)$, which contains the angular momentum dependence, the center of the basis function $r_0$, usually located at the position of the corresponding nucleus. The expansion coefficients $d_k$ and the orbital exponents $\zeta_k$ are usually optimized for a given basis set but remain unchanged during the SCF procedure. The most striking advantages of the GTO basis sets are good results for only small basis set sizes and the straight description of all electrons in the system. On the other hand, the fact that the basis functions are not generally orthogonal can lead to linear dependencies that cause problems in the SCF procedure and common problems related to the position dependence of the basis functions, like the basis set superposition error or Pulay forces, have to be taken care of.

Another approach, originally steaming from solid state physics, is the usage of plane wave basis sets. The underlying motivation is that the periodicity of a crystalline solid imposes the same periodicity on the electron density, suggesting basis functions according to:

$$\phi(r) = \frac{1}{\sqrt{\Omega}} \exp(\mathrm{iG} \cdot r). \tag{2.24}$$

Here, $\Omega$ is the volume of the periodic cell and the wave vector G has to satisfy the periodic boundary conditions. In most cases, the basis set expansion (cf. equation 2.19) incorporates all wave vectors up to a certain cutoff. Since the plane waves are independent of the nuclear positions, the basis set superposition error and Pulay forces do not occur and furthermore, the overlap matrix S is easy to calculate, because all basis functions are orthogonal. Although a plane waves basis set implies the usage of periodic boundary

conditions (see subsection 7.1.3 in the appendix for more details), gas phase calculations are still possible, if only the cell size is large enough, so that a molecule does not interact with its mirror image in a neighboring cell. This, however, leads to the fact that a large number of basis functions is used to describe also the empty part of the system. Another drawback of the plane waves method lies in the necessity of choosing a high cutoff in order to describe the rapid oscillations of the wave function due to a nodal orbital structure. A common way to overcome this problem is the application of so-called pseudopotentials. Pseudopotentials aim to smoothen the nodal structure for the inner orbitals close to the nuclei, which do not participate in chemical bonding, by combining the Coulomb potential of the nuclei and the effective interaction potential of the core electrons, and it replaces the Coulomb attraction of the nuclei in the external potential $v_{\text{ext}}(r)$ (cf. equation 2.11). In this way, lower cutoffs are sufficient for an adequate description of the electronic structure, reducing computational costs drastically.

A special implementation of DFT, the Gaussian and plane waves method, is discussed in the context of ab initio molecular dynamics simulations, in subsection 2.2.3.

## 2.2 Molecular simulations

The afore described quantum chemical methods serve as powerful techniques to calculate, for example, the electronic structure or energy minima for single molecules, ground states of individual atoms and molecules, excited states, and transition states that occur during chemical reactions. Thereby, one of the major goals of quantum chemistry is to reach an increased accuracy of the results for small molecular systems, and improving the scalability of the underlying methods to larger molecules to be processed, which is usually limited, since the computation time required rises as a power of the number of atoms.

Chemical processes, however, mostly take place in the condensed phase, especially in liquid media. Here, a multitude of further effects play a role, e.g. structural and dynamic effects, giving rise to a complex many-body problem, which has to be tackled when aiming at fully understanding the chemical processes on the molecular level. This, for example, comprises the role of solvation effects, which can have a strong influence on the reaction

kinetics and thermodynamics or on the stability, structure and orientation of a substrate in a medium. Investigating such effects demands for evaluating the temporal development of a system, as well as for the possibility to consider larger systems together with good approximations to describe both short-range and long-range interactions as accurately as possible.

Molecular simulations aim to capture the evolution of a chemical system over time, to predict time-dependent system properties or structural motives that occur after a certain time, when the system is equilibrated. To do so, the movement of the particles is described using a fundamental equation from classical mechanics, the Newtonian equation of motion, which was invented by Isaac Newton in 1687 and first published in 1726.[117] According to the second Newtonian law it is formulated:

$$F = m \cdot a, \tag{2.25}$$

or in words: the force $F$ is equal to mass $m$ times acceleration $a$. Since the acceleration is the second time derivative of the position and the force is the negative gradient of the (position-dependent) potential energy, the second Newtonian law can be reformulated according to:

$$-\nabla_i U_{\text{pot}}(r^N) = m_i \frac{d^2 r_i^N}{dt^2}(r^N), \quad i = 1, ..., N. \tag{2.26}$$

Here, $r^N \in \mathbb{R}^{3N}$ comprises the spatial positions of all $N \in \mathbb{N}$ particles of the system. The index $i$ refers to a distinct particle $i \in \{1, ..., N\}$. Thus, $-\nabla_i U(r) = f_i(r)$ is the force acting on particle $i$, so the i$^{\text{th}}$ entry of the negative potential gradient, and $m_i$ its mass. Instead of the Hamiltonian $\hat{H}$, here, the total energy $U_{\text{tot}}$ is considered:

$$U_{\text{tot}} = U_{\text{pot}} + U_{\text{kin}}, \tag{2.27}$$

where $U_{\text{kin}} = \frac{1}{2} \sum_{i=1}^{N} m_i v_i^2$ is the kinetic energy, which is dependent on the particle velocities $v_i$, $i = 1, ..., N$, and $U_{\text{pot}}$ is the potential energy.

In this work simulations of condensed matter systems, namely liquid systems, are taken into focus. In this regard the first in silico experiment, so the first molecular simulation was based on the Monte Carlo procedure, which was introduced by Metropolis and Ulam

in 1949 and first published in the frame of an experimental study in 1953.[97,98] Later the molecular dynamics (MD) technique was developed, which approximatively solves the Newtonian equation of motion on the molecular level with the aim to determine the dynamic properties of a many-particle system. At first this method was introduced for hard-sphere particles by Alder and Wainwright.[118,119] Thereby, the particles move with constant velocity between perfect-elastic collisions, enabling to exactly solve the dynamic problem without approximation. One year later Alder and Wainwright published a study about a small number of elastic spheres.[120] For so-called Lennard-Jones particles the force changes continuously as the particles move. This leads to the necessity that the Newtonian equation of motion has to be solved iteratively. This was first successfully executed by Rahman[121] followed by numerous further studies with respect to the simulation of Lennard-Jones particles, like for example by Verlet[122,123] and Nicolas et al.[124]

### 2.2.1 Molecular dynamics

Up to now the molecular dynamics procedure has been widely used in important scientific applications, cf. for example Allen and Tildesley,[125] Van Gunsteren and Berendsen,[126] Jensen[127], Frenkel and Smit[128], Hülsmann,[129] and Marx and Hutter.[130] All existing techniques related to MD simulations are based on solving the time-discretized Newtonian equation of motion (cf. equation 2.26). This means that the time-dependent position coordinates and velocities have to be calculated, which are saved within a so-called *trajectory*.

For solving such simple time-dependent differential equations numerically, the position and time are usually discretized such that the solution for a future time $t$ is predicted from functional values from previous times. Such finite difference methods typically go back to a Taylor series expansion, which also define the order of the numeric algorithm. In general, suitable algorithms should meet the following demands: they should

1. fulfill the laws of energy and momentum conversation and be time-reversible,
2. describe the 'real' trajectory as accurately as possible,
3. be applicable of larger time step width $\Delta t$,

4. require only little computational cost and memory space and

5. be easy to implement.

In the field of MD simulations the Verlet algorithm and its variants, developed by Loup Verlet,[122,123] represent the most commonly used methods for solving the Newtonian equation of motion. Here, a system composed of $N$ particles is considered, for which $R_i(t)$ describes the coordinates of particle $i$ at time $t$. The basis of the Verlet algorithm is given by a forward-backward Taylor series expansion of $R_i$:

$$R_i(t+\Delta t) = R_i(t) + \Delta t\frac{dR_i}{dt}(t) + \frac{1}{2}\Delta t^2\frac{d^2R_i}{dt^2}(t) + \frac{1}{6}\Delta t^3\frac{d^3R_i}{dt^3}(t) + \mathcal{O}(\Delta t^4), \quad (2.28)$$

$$R_i(t-\Delta t) = R_i(t) - \Delta t\frac{dR_i}{dt}(t) + \frac{1}{2}\Delta t^2\frac{d^2R_i}{dt^2}(t) - \frac{1}{6}\Delta t^3\frac{d^3R_i}{dt^3}(t) + \mathcal{O}(\Delta t^4). \quad (2.29)$$

Upon addition of equation 2.28 and 2.29 and inserting the Newtonian equation of motion given in equation 2.26, we receive the calculation rule for the classical Verlet algorithm, which possesses an order of four:

$$R_i(t+\Delta t) = 2R_i(t) - R_i(t-\Delta t) + \Delta t^2\frac{d^2R_i}{dt^2}(t) + \mathcal{O}(\Delta t^4), \quad (2.30)$$

where $\frac{d^2R_i}{dt^2}(t) = -\frac{1}{m_i}\nabla U(R_i(t))$ with $m_i$ being the mass of particle $i$ and the underlying (position-dependent) potential $U(R_i(t))$. It has to be noted that for the classical Verlet algorithm the velocities of the particles cancel out. In a second step the velocities can be determined, however, only based on the current time step $t$. Thus, subtracting equation 2.29 from equation 2.28 leads to the central differences of $v(t)$, possessing an order of two:

$$v_i(t) = \frac{R_i(t+\Delta t) - R_i(t-\Delta t)}{2\Delta t} + \mathcal{O}(\Delta t^2). \quad (2.31)$$

Due to the fact that $R_i(t+\Delta t)$ and $R_i(t-\Delta t)$ play the same role in equations 2.30 and 2.31, respectively, the classical Verlet algorithm is time-reversible.

One variant of the Verlet algorithm, which is used in many simulation tools, is the so-called Leap Frog Verlet, developed by Hockney and Potter.[131,132] Here, the velocity at time $t$ is replaced by the velocity at time $t + \frac{\Delta t}{2}$, which is estimated by the central

difference:

$$v_i\left(t+\frac{\Delta t}{2}\right) = v_i\left(t-\frac{\Delta t}{2}\right) + \Delta t a_i(t). \tag{2.32}$$

Thus, the resulting calculation rule is given by:

$$R_i(t+\Delta t) = R_i(t) + \Delta t v_i\left(t+\frac{\Delta t}{2}\right) = R_i(t) + \Delta t\left(v_i\left(t-\frac{\Delta t}{2}\right) + \Delta t a_i(t)\right), \tag{2.33}$$

and the current velocity is determined as the average of both half time steps:

$$v_i(t) = \frac{v_i\left(t+\frac{\Delta t}{2}\right) + v_i\left(t-\frac{\Delta t}{2}\right)}{2}. \tag{2.34}$$

This algorithm is called Leap Frog Verlet because the velocities are leaping over the current time step $t$, so they go over from $t-\frac{\Delta t}{2}$ to $t+\frac{\Delta t}{2}$.

Another variant of the classical Verlet algorithm is the Velocity-Verlet algorithm, which was developed by Swope et al. and is solely based on the particle velocities.[133] The Velocity-Verlet algorithm possesses the following shortened form:

$$v_i(t+\Delta t) = v_i(t) + \frac{\Delta t}{2}(a_i(t) + a_i(t+\Delta t)). \tag{2.35}$$

Here, the actual calculation rule is composed of two steps:

$$v_i\left(t+\frac{\Delta t}{2}\right) = v_i(t) + \frac{\Delta t}{2}a_i(t), \tag{2.36}$$

$$v_i(t+\Delta t) = v_i\left(t+\frac{\Delta t}{2}\right) + \frac{\Delta t}{2}a_i(t+\Delta t). \tag{2.37}$$

Equation 2.37 is resulting from:

$$v_i\left(t+\frac{\Delta t}{2}\right) = v_i(t+\Delta t) - \frac{\Delta t}{2}a_i(t+\Delta t), \tag{2.38}$$

with the acceleration $a_i$ at time $t+\Delta t$ being determined according to the classical Verlet algorithm (equation 2.30).

The Verlet algorithm and its variants meet the demands formulated at the beginning of this subsection (cf. for example Allen and Tildesley[125]), and possess a rather low

complexity, which is why they are widely used for state-of-the-art MD simulations.

At this point the core of any molecular dynamics scheme is reached, leading to the question how to describe — or in practice how to approximate — the interatomic interactions. In this work it is focused on two techniques that differ exactly in answering this question: classical MD simulations and AIMD simulations. The technical details of both methods are introduced in the following two subsections 2.2.2 and 2.2.3.

### 2.2.2 Classical molecular dynamics simulations

In classical molecular dynamics simulations another important approximation is made: it is not distinguished between electrons and nuclei, but the atom itself represents the smallest unit in the system, from which all particles are built. For the description of intra- and intermolecular interactions of the atoms in the system, a so-called *force field* is introduced, which in relation to MD simulations means an *ansatz* function with corresponding parameters that is required to calculate a force as a negative spatial gradient of a potential. Thus, the aim is to determine a set of parameters for each atom type, that describe the bond length, angles, improper torsions and dihedral angles, as well as the intermolecular interactions, which are for example based on dispersion and electrostatic forces, as accurately as possible. Of course the number of atom types must be by far larger than the number of elements in the periodic table, because atoms of the same element may differ in their chemical environment and hybridization state. In the following the single force field contributions, as well as two examples for prominent total potentials are introduced.

#### Intramolecular potentials

The description of the intramolecular potentials is mostly based on geometric criteria and comprises for example the change of bond lengths and bond angles between atoms within a molecule. Here, bond angles between three atoms or dihedral angles between four atoms are taken into consideration, as well as special cases of angles, which are for example given if an atom is $sp^2$-hybridized. Except for the dihedral angles, intermolecular interactions

are in most cases described by harmonic potentials $U(r)$, for which it can be defined:

$$\Delta U(r) = 0, \tag{2.39}$$

with $\Delta$ being the Laplace operator.

The bond length potential is defined as follows:

$$U_{\mathrm{b}}(r) = \frac{k_r}{2}(r - r^0)^2, \tag{2.40}$$

where $r^0$ is the equilibrium distance for a given bond length $r$ (cf. Figure 2.1 a)) and $k_r$ is the force constant.

Analogously, the bond angle potential can be written as:

$$U_{\mathrm{a}}(\phi) = \frac{k_\phi}{2}(\phi - \phi^0)^2, \tag{2.41}$$

with the equilibrium angle $\phi^0$ for a given bond angle $\phi$ (cf. Figure 2.1 a)) and the corresponding force constant $k_\phi$.

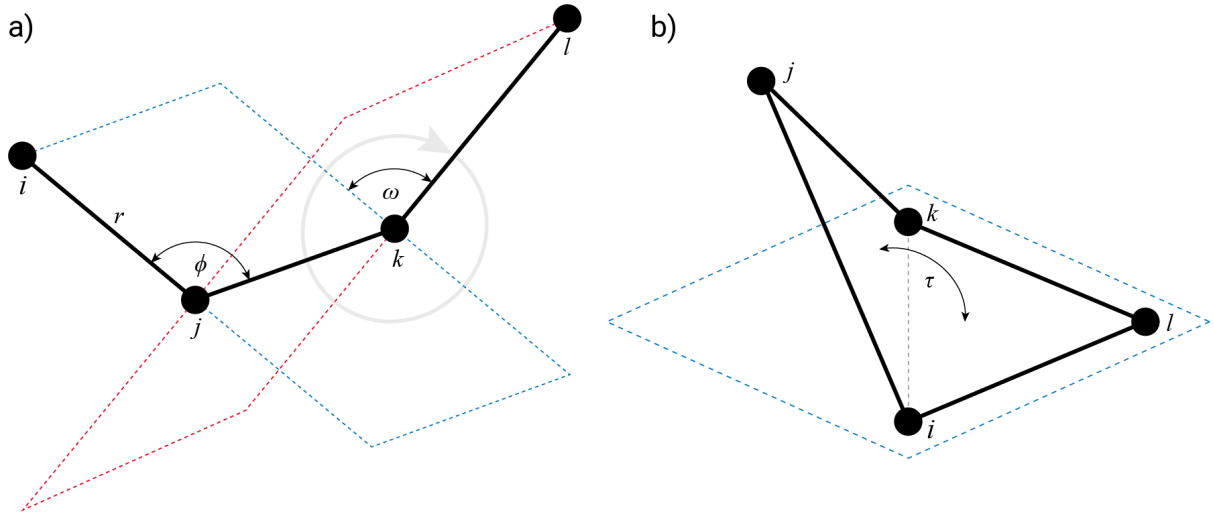


**Figure 2.1** Ball-and-stick models to illustrate intramolecular interactions. a) Left: $r$ is the bond length between atoms $i, j$, $\phi$ the bond angle between atoms $i, j, k$ and $\omega$ is the dihedral angle between the two planes (displayed by blue and red dotted lines) that are spanned by atoms $i, j, k$ and $j, k, l$, respectively. The gray arrow represents the theoretically possible rotation around the bond between atoms $j, k$. b) Right: Improper dihedral angle $\tau$ between the plain (displayed by the blue dotted lines) that is spanned by the atoms $i, l, k$ and the out-of-plane atom $j$.

The dihedral angle $\omega$ (cf. Figure 2.1 a)) describes the conformation between four atoms $i,\ j,\ k$ and $l$ and can be rationalized as the angle between the plain spanned by the atoms $i,\ j$ and $k$ and the plain spanned by the atoms $j,\ k$ and $l$. Such angles are represented by a special potential, which depends on $\omega \in [0°, 360°]$ or $\omega \in [-180°, 180°]$. Due to the fact that this is a rotation potential, it has to be periodic as well. The chemical motivation for this can be deduced from the following example: in case of an $sp^3$-hybridized terminal carbon atom of carbon hydrogen compounds the bonded hydrogen atoms can rotate continuously around the carbon atom. After a rotation for 120° the resulting geometry is equivalent to the former geometry. For $sp^2$-hybridized carbon atoms this is the case after a 180° rotation. Since the barrier for the rotation is usually not high, strong deviations from the minimum $\omega_0$ are possible. Due to the periodicity the potential can be expressed by a Fourier series:

$$U_{\mathrm{d}}(\omega) = \sum_{n=1}^{m} V_n \cos(n\omega),\ m \in \mathbb{N}. \tag{2.42}$$

Here, $\frac{2\pi}{n}$ describes the periodicity and $V_n,\ n = 1, ..., m,\ m \in \mathbb{N}$, are the rotation constants for dihedral angle $\omega$, which describe the rotational barrier around the axis of atoms $j$ and $k$. Usually, the point of origin is shifted for the dihedral angle potential:

$$U_{\mathrm{d}}(\omega) = \frac{V_1}{2}(1 + \cos(\omega)) + \frac{V_2}{2}(1 + \cos(2\omega)) + \frac{V_3}{2}(1 + \cos(3\omega)) + ... \ . \tag{2.43}$$

Here, the sign of the cosine term is chosen in a way, that the minimum is located at $\omega = 180°$ for the one-fold rotation term, at $\omega \in \{0°, 180°\}$ for the two-fold term, at $\omega \in \{60°, 180°, 300°\}$ or $\omega \in \{-60°, 60°, 180°\}$ in case of the three-fold term and so on. Due to the factor $\frac{1}{2}$ the Fourier coefficients represent direct rotational barriers. The case $V_n < 0$ is not excluded.

In case of $sp^2$-hybridized carbon atoms or if the atoms are connected as shown in Figure 2.1 b), so there are bonds between atoms $i$ and $l$, $k$ and $l$, $i$ and $j$ as well as $k$ and $j$, a special situation arises. Since atom $j$ is looming out of the plane that is spanned by the atoms $i,\ k$ and $l$, it is denoted as out-of-plane atom. The resulting angle deformation would lead to too high force constants, which is why a separate term

is introduced: the potential of improper dihedral angles. This is again expressed by an harmonic potential:

$$U_{\mathrm{id}}(\tau) = \frac{k_\tau}{2}(\tau - \tau^0)^2. \tag{2.44}$$

Here, $\tau^0$ is the equilibrium angle for the given improper dihedral angle $\tau$ and $k_\tau$ is the according force constant.

### Intermolecular potentials

The intermolecular potentials can be divided into short-range terms, which describe forces that are based on dispersion and repulsion effects, and long-range terms, which comprise electrostatic effects. Both types have to be taken into consideration to describe the forces between atoms that are not chemically bound to each other.

Starting from the short-range interactions there are different alternatives to describe the interactions of chemically non-bonded and uncharged atoms with the most prominent example probably being the Lennard-Jones (LJ) potential, which is shown in Figure 2.2 and goes back to Lennard-Jones (1931).[134] Please note that depending on how the LJ potential is defined, it can contain long-range parts as well. As can be seen, the potential consists of an attractive part and a repulsive part. At larger distance between two interaction sites the attractive part dominates and the particles approach each other. The closer the sites approach each other the more energy is released, meaning that the potential becomes more negative. At a certain position the potential reaches a minimum at which the attractive and the repulsive forces are in balance. The distance $r$ at the minimum is therefore denoted as the equilibrium distance between the particles. If the interacting sites come even closer, the repulsive part dominates, which is based on the Pauli repulsion principle. The latter one originally states that electrons of opposite spin but otherwise equal quantum numbers reject each other if their orbitals overlap. Thus, the potential increases and approaches infinity for very small distances.

The attractive part of the LJ-potential is described by the London formula, which assumes that the attractive force can be expressed by a negative $r^{-6}$-term:

$$U_{\mathrm{att.}}(r) = -\frac{C_6}{r^6}. \tag{2.45}$$

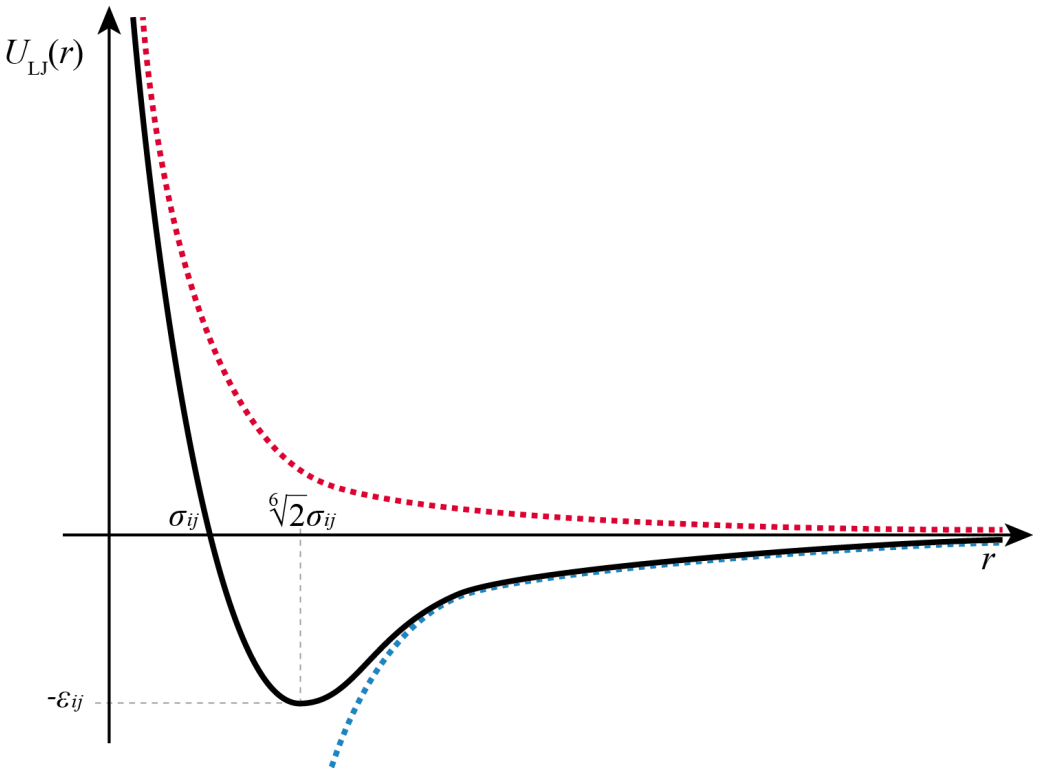


**Figure 2.2** Schematic representation of the Lennard-Jones potential $U_{\mathrm{LJ}}(r)$ as a function of distance $r$ between two particles $i$ and $j$, resulting from the sum of an attractive potential (blue dotted line) and a attractive potential (red dotted line). The zero-crossing point of the LJ-potential is located at $(\sigma_{ij}|0)$ and its minimum lies at $(\sqrt[6]{2}\sigma_{ij}|-\varepsilon_{ij})$, in which $\sigma_{ij}$ can be interpreted as the interaction radius of the interaction sites $i$ and $j$ and $-\varepsilon_{ij}$ as the depth of the potential minimum.

The term here denoted as $C_6$ is often only hardly accessible and depends for example on the ionization energy. The repulsive part is expressed by a positive $r^{-12}$-term:

$$U_{\mathrm{rep.}}(r) = +\frac{C_{12}}{r^{12}}. \tag{2.46}$$

This term is not motivated physically, but numerically, simply because $(r^{-6})^2 = r^{-12}$. In total the (12,6)-Lennard-Jones potential for a distance $r$ between two interaction sites arises from equations 2.45 and 2.46:

$$U_{\mathrm{LJ}}(r) = 4\varepsilon_{ij}\left[\left(\frac{\sigma_{ij}}{r}\right)^{12} - \left(\frac{\sigma_{ij}}{r}\right)^{6}\right],\ \varepsilon_{ij}, \sigma_{ij} \geq 0. \tag{2.47}$$

The two parameters $\varepsilon_{ij}$ and $\sigma_{ij}$ can be interpreted when considering the properties of the LJ-potential curve shown in Figure 2.2:

i) $U_{\mathrm{LJ}}(\sigma_{ij}) = 0$, i.e., $\sigma_{ij}$ is the zero-crossing point of the LJ-potential and can be interpreted as the interaction radius of the two interaction sites.

ii) $U'_{\mathrm{LJ}}(\sqrt[6]{2}\sigma_{ij}) = 0 \wedge U''_{\mathrm{LJ}}(\sqrt[6]{2}\sigma_{ij}) > 0$, i.e., at the position $r = \sqrt[6]{2}\sigma_{ij}$ the LJ-potential possesses a minimum.

iii) $U_{\mathrm{LJ}}(\sqrt[6]{2}\sigma_{ij}) = -\varepsilon_{ij}$, i.e., $\varepsilon_{ij}$ represents the depth of the potential minimum.

The parameters $\varepsilon_{ij}$ and $\sigma_{ij}$ are determined via combination rules from the parameter pairs $\varepsilon_i, \sigma_i$ and $\varepsilon_j, \sigma_j$, which correspond to the particles $i$ and $j$, via combination rules. Commonly used are the Lorentz–Berthelot formulas,[135,136] based on the geometric average for $\varepsilon_{ij}$ and the arithmetic average for $\sigma_{ij}$:

$$\varepsilon_{ij} = \sqrt{\varepsilon_i \varepsilon_j}, \tag{2.48}$$

$$\sigma_{ij} = \frac{1}{2}\left(\sigma_i + \sigma_j\right). \tag{2.49}$$

Depending on the force field other combinations are possible, e.g., for $\sigma_{ij}$ the geometric average can be used as well.

In most cases the force fields used in this work are based on the (12,6)-Lennard-Jones potential to describe the short range interactions of the particles. The reason for this is probably due to the fact that it has been shown to represent a good approximation of the real intermolecular interactions (cf. Allen and Tildesley[125]). Moreover, the LJ-potential is mathematically easy to handle and does not require numerically demanding function evaluations. Another potential, based on an exponential term and thus requiring a higher computational effort, is the Morse potential.[137] Here, the exponential term allows for the inclusion of higher-order interactions than dipole-interactions. A third, popular potential is the Buckingham potential.[138] The motivation for this potential lies in the assumptions that the repulsive part is based on the overlap of waves and that the electron density is proportional to $\exp(-r)$. Therefore, the Buckingham potential differs from the LJ-potential with respect to the repulsive term. For more detail about the Morse and Buckingham potential see for example Jensen.[127]

For the description of long-range interactions based on the partial charges of the atoms, the electrostatic potential or Coulomb potential is used. In contrast to the LJ-potential,

it comprises a $r^{-1}$-term:

$$U_{\mathrm{C}}(r) = \frac{q_i q_j}{4\pi\varepsilon_0 r}, \tag{2.50}$$

with the charges $q_i$ and $q_j$, $i, j = 1, ..., N$ for two atoms, their distance $r$ and the vacuum permittivity $\varepsilon_0$. The Coulomb potential originates from the Coulomb law,[139] which represents a to date consistently confirmed law of nature for point charges. Partial charges within a molecule, which can be summed up to yield the total charge of the molecule, do not change in the course of a simulation. Therefore, their determination has to take place in the equilibrium state and the charges have to be localized in the atom centers. Most methods to calculate the atomic charges are based on quantum mechanical methods, like for example the CHELPG (**ch**arges from **el**ectrostatic **p**otentials using a **g**rid) method.[140]

### Total potential

A total potential or force field is composed of the previously introduced potential terms by a simple addition of the single components. The individual terms are considered to be independent and cross-correlations — if required — can be included by adding the according coupling terms. Most force fields differ only insignificantly with respect to the definition of the single potential terms.

The AMBER (**a**ssistent **m**odel **b**uilding and **e**nergy **r**efinement) potential was developed by Weiner et al.,[141] in particular for the simulation of biomolecules like proteins and nucleic acids. It is given by the following form:

$$\begin{aligned} U_{\mathrm{AMBER}}(r^N) &= \sum_{\text{bonds btw. } i,j} K_r^{ij}(r_{ij} - r_{ij}^0)^2 + \sum_{\text{angles btw. } i,j,k}^{N} K_\phi^{ijk}(\phi_{ijk} - \phi_{ijk}^0)^2 \\ &+ \sum_{\text{dihedrals } \omega} \frac{V_n}{2}(1 + \cos(n\omega) - \gamma) \\ &+ \sum_{i=1}^{N-1}\sum_{j=i+1}^{N} \left\{ 4\varepsilon_{ij}\left[\left(\frac{\sigma_{ij}}{r}\right)^{12} - \left(\frac{\sigma_{ij}}{r}\right)^{6}\right] + \frac{q_i q_j}{4\pi\varepsilon_0 r}\right\}. \end{aligned} \tag{2.51}$$

Here, $r^N$ is a three-dimensional position vector. It must be noted that for the force constants regarding the bonds and angles $K_r$ and $K_\phi$ are used instead of $\frac{k_r}{2}$ and $\frac{k_\phi}{2}$ (cf.

equations 2.40 and 2.41). This, however, does not mean that the factor $\frac{1}{2}$ is neglected, but it is already included in the constants. In case of the dihedral angles the afore mentioned shift of the point of origin is performed and, additionally, a shift parameter $\gamma$ is introduced for the cosine terms.

The OPLS-AA (**o**ptimized **p**otential for **l**iquid **s**imulations - **a**ll-**a**tom) potential, developed by Jorgensen et al.,[142] is one of the younger potentials and possesses the following form:

$$\begin{aligned} U_{\mathrm{OPLS-AA}}(r^N) &= \sum_{\text{bonds btw. } i,j} K_r^{ij}(r_{ij}-r_{ij}^0)^2 + \sum_{\text{angles btw. } i,j,k}^{N} K_\phi^{ijk}(\phi_{ijk}-\phi_{ijk}^0)^2 \\ &+ \sum_{\text{dihedrals } \omega} \frac{V_1}{2}(1+\cos(\omega)) + \frac{V_2}{2}(1+\cos(2\omega)) + \frac{V_3}{2}(1+\cos(3\omega)) \\ &+ \frac{V_4}{2}(1+\cos(4\omega)) + \sum_{i=1}^{N-1}\sum_{j=i+1}^{N}\left\{4\varepsilon_{ij}\left[\left(\frac{\sigma_{ij}}{r}\right)^{12}-\left(\frac{\sigma_{ij}}{r}\right)^{6}\right]+\frac{q_i q_j}{4\pi\varepsilon_0 r}\right\} f_{ij}. \end{aligned} \tag{2.52}$$

Here, analogously to the AMBER potential, the bisected force constants $K_r$ and $K_\phi$ are used and for the dihedral angles it is explicitly assumed that $m = 4$, i.e., potential terms of lower periodicity are neglected. A specialty of the OPLS-AA force field is the scaling factor $f_{ij}$. In this context it has to be stated that intermolecular interactions can also occur within a molecule, namely when atoms are separated by three or more bonds from each other. Since four atoms are needed for three bonds, the interactions are also denoted as 1-4-interactions. In this case $f_{ij}$ equals 0.5. For two atoms that are separated by more than three bonds $f_{ij}$ equals 1.

For the description of the ionic liquid cations' and anions' intra- and intermolecular interactions considered within this work, the force field parameters were chosen according to Canongia Lopes and Pádua,[59,60] who developed the parameters based on the OPLS-AA/AMBER framework and on the OPLS-AA model, which is oriented towards the calculation of equilibrium thermodynamic and structural properties.[142,143]

All classical MD simulations presented in this work were performed using the LAMMPS (Large-scale Atomic/Molecular Massively Parallel Simulator) simulation software (Version 12$^{\text{th}}$ April 2013).[144]

### 2.2.3 Ab initio molecular dynamics simulations

The basic idea of ab initio molecular dynamics simulations is that the forces are calculated at the level of the many-body problem of interacting electrons and nuclei forming atoms and molecules as they are considered within the framework of quantum mechanics, whereas the dynamics is described according to classical dynamics and statistical mechanics. Since the seminal contribution of Car and Parinello[145], which is why AIMD is often referred to as "Car–Parinello" or just "CP simulations",[130] many more techniques to include the electronic structure in molecular dynamics simulations have been developed, like the Ehrenfest or the Born–Oppenheimer methods. The AIMD simulations presented in the frame of this work are performed using the Born–Oppenheimer method, which is why in the following the focus is put on the according characteristics and details.

The Born–Oppenheimer method starts by separating the nuclear and electronic degrees of freedom from each other via solving the static electronic structure problem in each molecular dynamics step in which the nuclear positions are fixed at that instant of time. Therefore, the electronic structure part is reduced to solving the time-independent Schrödinger equation, while at the same time the nuclei are propagated in time according to classical mechanics. In this way, the time-dependence of the electronic structure is dictated by its parametric dependence on the classical dynamics of the nuclei. Thus, the Born–Oppenheimer MD method to calculate the electronic ground state can be readily expressed by:

$$M_I \ddot{R}_I(t) = -\nabla_I \min_{\Psi_0} \{\langle \Psi_0 | \hat{H}_e | \Psi_0 \rangle\}, \tag{2.53}$$

$$\hat{H}_e \Psi_0 = E_0 \Psi_0, \tag{2.54}$$

where $M_I$ is the mass of the respective nucleus $I$ and $\ddot{R}_I(t)$ is the second time derivative of the nucleus position, so its acceleration. The expectation value $\{\langle \Psi_0 | \hat{H}_e | \Psi_0 \rangle\}$ has to be minimized for each MD step. When using DFT to determine the electronic contribution in terms of the effective one-particle Hamiltonian $\hat{H}_e$, the according Kohn–Sham operator

$H_e^{\mathrm{KS}}$ can be inserted:

$$M_I \ddot{R}_I(t) = -\nabla_I \min_{\phi_i}\{\langle \Psi_0 | H_e^{\mathrm{KS}} | \Psi_0 \rangle\} = -\nabla_I \min_{\phi_i}\{E^{\mathrm{KS}}\}, \tag{2.55}$$

$$H_e^{\mathrm{KS}} \phi_i = \epsilon_i^{\mathrm{KS}} \phi_i, \tag{2.56}$$

where equation 2.56 is analogue to the Kohn–Sham equation 2.16, replacing the Kohn–Sham orbitals $\theta_i$ by the auxiliary basis functions $\phi_i$. Thus, the Kohn–Sham energy minimum represents the electronic ground state energy of a system with nuclei at fixed positions $R_I$.

In the late 1980s and early 1990s, the combination of the Born–Oppenheimer propagation scheme with DFT,[146] in conjunction with effective orbital prediction methods[147,148] and parallelization strategies[149], have led to great success in the ab initio simulation of condensed matter. Ever since, accelerated by the continuous improvement of quantum chemistry electronic structure codes and computational resources,[150] AIMD approaches nowadays represent a well-established and powerful tool in the wide field of material science.[130,151]

The AIMD simulations presented in this work are performed using the CP2K software package,[152] which is based on a particular implementation of DFT, namely the Gaussian and plane waves (GPW) method[153] combined with the QUICKSTEP module.[154] Within this approach, the Kohn–Sham orbitals are expanded in terms of GTO basis functions (cf. subsection 2.1.2), but an auxiliary basis of plane waves is added for a second description of the electron density. For the conversion between both descriptions, the electron density emanating from the GTO basis is projected onto a real-space grid with a spacing determined by the cutoff chosen for the plane waves and the plane waves coefficients are obtained from a discrete Fourier transformation. In order to reduce the cutoff for the plane waves, the Goedecker/Teter/Hutter (GTH) pseudopotentials[155–157] are employed as discussed in subsection 2.1.2. The characteristics of these kind of pseudopotentials are that they are norm-conserving and separable and they allow for an analytic calculation of the corresponding matrix elements in the GTO basis set due to their dual-space Gaussian form. The kinetic energy contributions to the Kohn–Sham matrix are evaluated in the GTO basis as well, whereas the Coulomb interactions and the exchange-correlation po-

tential can be more accurately calculated through the plane waves representation of the electron density. Overall, this leads to a construction scheme for the Kohn–Sham matrix that scales only linearly with the size of the system considered.

The usage of GTH pseudopotentials leads to an extinction of the electron density at the positions of the nuclei, with the exception of hydrogen atoms. Thus, many GGA exchange-correlation functionals, which contain electron density terms in the denominator, run into numerical problems. In order to avoid this effect, several smoothing options have been developed and implemented into the CP2K code.[154]

Another specialty of the CP2K package concerns the SCF procedure, which usually relies on the diagonalization of a matrix as discussed in subsection 2.1.2. Alternatively, CP2K uses a direct minimization of the electronic energy (equation 2.15) combined with the basis set expansion (equation 2.19). Here, the energy is a function of the expansion coefficients $E(\mathrm{C})$, and the orthonormality constraint is given by:

$$\mathrm{C}^{\mathrm{T}}\mathrm{SC} = \mathrm{I}, \tag{2.57}$$

with C and S being analogously defined as in equations 2.19 and 2.22, respectively, and the according identity matrix I. Due to the non-linearity of the constraint, the minimization would lead to a curved geodestric, which can be avoided by introducing new set of variables X,[158] to fulfill a linear constraint:

$$\mathrm{X}^{\mathrm{T}}\mathrm{SC}_0 = 0. \tag{2.58}$$

Here, $\mathrm{C}_0$ represents constant initial coefficients that satisfy the original constraint $\mathrm{C}_0^{\mathrm{T}}\mathrm{SC}_0 = \mathrm{I}$. The coefficients C are related to the new variables X via:

$$\mathrm{C} = \mathrm{C}_0 \cos(\mathrm{U}) + \mathrm{XU}^{-1} \sin(\mathrm{U}),\ \mathrm{U} = \left(\mathrm{X}^{\mathrm{T}}\mathrm{SX}\right)^{\frac{1}{2}}. \tag{2.59}$$

Based on this linear constraint, any standard minimization method such as conjugate gradients[159] or direct inversion in the iterative subspace (DIIS)[160] can be employed. CP2K offers the orbital transformation (OT) method as direct minimization scheme, which has

shown to be fast and successful in terms of the SCF convergence for an appropriate setting.[154]

## 2.3 Investigating structural properties

When performing a simulation, classical MD or AIMD, only a few system properties are directly accessible, like the total energy, the potential and kinetic energy, the systems overall volume and density, depending on the ensemble chosen the systems temperature and pressure. All other properties, like for example structural, dynamic and spectroscopic properties, have to be determined after the simulation via post-processing the resulting trajectory. For this purpose the trajectory analyzer and visualizer tool TRAVIS has been developed in the Kirchner work group,[86,87] which is freely accessible and offers a multitude of different advanced analysis functions. Since for the scope of this work the emphasis is put on the investigation of structural properties of complex liquids, i.e. ionic liquids and IL-mixtures, in the following it is only focused on the according relevant functions.

### 2.3.1 Radial distribution functions

The static functions within TRAVIS comprise a number of different distribution functions (DFs), of which radial, angular, as well as the combination of both, combined distribution functions (RDFs, ADFs and CDFs, respectively) play a superior role for this work. Seen from statistical mechanics[161] these functions are based on the probability of finding certain structural motives amongst the molecules within the simulation box for each time step of the trajectory. At the easy example of the radial distribution function, the probability of finding two particles 1 and 2 in space at the positions $R_1$ and $R_2$ is given by:

$$P_N^{(2)}(\mathrm{R}_1, \mathrm{R}_2) = \int d\mathrm{R}_3 \int d\mathrm{R}_4 \; ... \; d\mathrm{R}_N P_N(\mathrm{R}^N), \tag{2.60}$$

with the probability distribution $P_N(\mathrm{R}^N)$ of configuration $\mathrm{R}^N$. This function is specific for particles 1 and 2. For the consideration of any particle pairs the generic two-particle

probability distribution is determined:

$$\rho_N^{(2)}(\mathrm{R}_1, \mathrm{R}_2) = N(N-1)\ P_N^{(2)}(\mathrm{R}_1, \mathrm{R}_2). \tag{2.61}$$

This expression equals the probability of finding any particle pair of configuration $\mathrm{R}_1, \mathrm{R}_2$. Integration of $\rho_N^{(2)}(\mathrm{R}_1, \mathrm{R}_2)$ over one spatial coordinate and division by the total number of particles $N$ leads to the generic one-particle probability distribution, which equals the density of the system:

$$\frac{1}{N-1} \int d\mathrm{R}_2\ \rho_N^{(2)}(\mathrm{R}_1, \mathrm{R}_2) = \rho_N^{(1)}(\mathrm{R}_1) = \rho = N/V. \tag{2.62}$$

Under normal equilibrium conditions the correlations in liquids only stretch out over a finite distance $\xi$. Above this distance, correlations can be neglected and the pair correlation functions can be fractionated into the product of two one-particle distributions:

$$|\mathrm{R}_1 - \mathrm{R}_2| \gg \xi \Rightarrow \rho_N^{(2)}(\mathrm{R}_1, \mathrm{R}_2) \approx \left(\frac{N-1}{N}\right) \rho_N^{(1)}(\mathrm{R}_1)\ \rho_N^{(1)}(\mathrm{R}_2) \approx \rho^2. \tag{2.63}$$

Thus, normalization of $\rho_N^{(2)}(\mathrm{R}_1, \mathrm{R}_2)$ to the square of the density $\rho^2$ yields the pair correlation function $g_N^{(2)}(\mathrm{R}_1, \mathrm{R}_2)$:

$$g_N^{(2)}(\mathrm{R}_1, \mathrm{R}_2) \equiv \frac{\rho_N^{(2)}(\mathrm{R}_1, \mathrm{R}_2)}{\rho^2}, \tag{2.64}$$

which reaches unity for long distances between the particles. The pair correlation can be expressed as a function $g(r)$ of distance $r = |\mathrm{R}_1 - \mathrm{R}_2|$ as well, which then equals the desired radial distribution function. In this way, RDFs serve to investigate typical distances between atoms or other relevant entities, like the center of mass (CoM) of molecules or center of ring (CoR) in case of present ring structures, which can be directly interpreted in terms of occurring (or missing) interactions between the atoms or entities.

In addition to this, RDFs can reveal further characteristics, such as the solvation structure around a reference particle, which can be easily rationalized when considering a Lennard-Jones fluid as a model system: for $r < \sigma$ the RDF vanishes due to the strong core-core-repulsion. When $r$ is slightly greater than $\sigma$, a first maximum appears, which

corresponds to the first solvation shell of nearest neighbors around the reference particle. For most liquids also a second maximum appears, which is usually broader and less pronounced compared to the first maximum due to the increasing disorder in fluid media with increasing distance. For $r = N \cdot \sigma$ the fluctuations become too strong and $g(r)$ reaches its asymptotic limit at unity. The integral of the first maximum is connected to the average number of particles within the first coordination shell:

$$N_c = 4\pi\rho \int_0^{r_{\min}} dr r^2 \; g(r). \tag{2.65}$$

Here, $r_{\min}$ represents the distance to the first minimum of $g(r)$.

Analogously to the derivation above, angular distribution functions can be employed in order to analyze typical angular constellations present in the system. This, however, does not only comprise intramolecular angles, but in particular the intermolecular angles formed by three atoms or other relevant units and angles between two vectors that can, for example, be defined along an alkyl side chain or perpendicular to a ring plane. In this way it is possible to investigate molecular orientations which is of great importance to fully understand the structural situation in a complex liquid on the molecular level.

An additional implementation in TRAVIS is the possibility to calculate combined distribution functions, e.g., a combination of RDF and ADF, or two RDFs, which allow for the correlation of two criteria to characterize the occurrence of specific molecular constellations or single interactions. A good example in that regard is the investigation of hydrogen bonds, as shown in Figure 2.3 for the 1-ethyl-3-methylimidazolium acetate ([$C_2C_1$Im][OAc]) ionic liquid. Hydrogen bonds are not solely characterized by a distance $r$ between the donor and acceptor atom, but also by the angle $\alpha$ between the donor and acceptor site, bridged by the hydrogen atom (cf. Figure 2.3). This is of high relevance for defining criteria to analyze the hydrogen bond dynamics, e.g., their lifetime.[77,87,162] In this way, by using a color scale, CDFs can reveal the occurrence of certain events dependent of two independent criteria. This is as well interesting in the context of chemical reactions, e.g. a $S_N2$-like reaction, where an atom's distance to the leaving unit can be correlated with its distance to the substituting unit, in order to gain deeper insight into the mechanism of the process.[84,163]

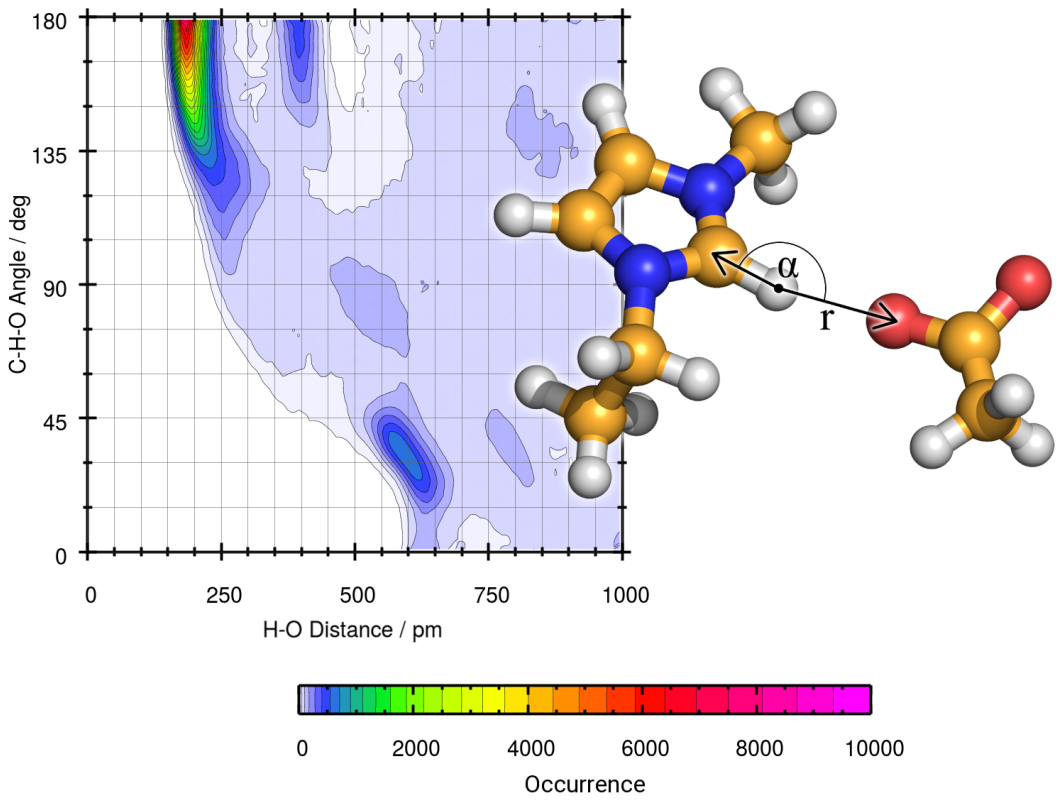


**Figure 2.3** Combined distribution function (CDF) depicting the O-H distance $r$ on the x-axis and the O-H–C angle $\alpha$ on the y-axis for the ionic liquid $[C_2C_1Im][OAc]$, to investigate the hydrogen bonding between the cation and the anion.

## 2.3.2 Spatial distribution functions

A special type of static function accessible in TRAVIS is the spatial distribution function (SDF). SDFs are employed to analyze the local environment of a selected reference molecule in the system, by visualizing the spatial, three-dimensional density distribution of other relevant moieties around this reference molecule under application of a color code. Thus, it is necessary to previously sort and group all chemically analogous moieties present in the system. The different groups that are defined are denoted as subsets hereafter.

As an example we consider an ionic liquid-alcohol mixture composed of 250 ion pairs of 1-octyl-3-methylimidazolium bis(trifluoromethylsulfonyl)imide ($[C_8C_1Im][NTf_2]$) and 50 $n$-dodecanol molecules, and focus on the local environment of one $[C_8C_1Im]^+$ cation and one $n$-dodecanol molecule as references (cf. Figure 2.4).[164] Since the microheterogeneity

in ionic liquids arises from the mismatch of polar and non-polar interactions, resulting in a nanosegregation of the polar and non-polar molecular units (cf. section 1.2), the complex structure forming in the mixture can be analyzed when distinguishing between these polar and non-polar groups. Thus, the subsets are defined as follows: the polar subsets comprise the head group of the cations (P-IL (Cat), colored in red), the anions (P-IL (An), colored in orange), and the polar head group of the *n*-dodecanol molecules (P-A, colored in yellow), while the non-polar subsets include the alkyl-tail of the cations (N-IL, colored in green) and the alkyl-tail of the alcohol molecules (N-A, colored in blue), respectively (cf. Figure 2.4 a)).

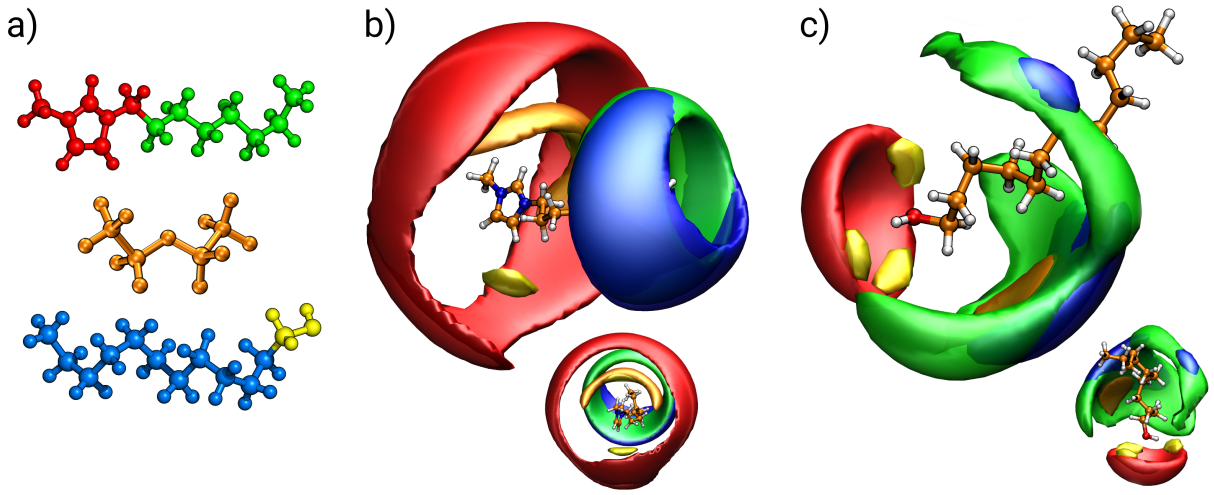


**Figure 2.4** Spatial distribution functions (SDFs) for components around the b) $[C_8C_1Im]^+$ cation and the c) *n*-dodecanol for a 250 IL ion pairs of $[C_8C_1Im][NTf_2]$ to 50 alcohol molecules mixture. The isosurface colors are chosen as follows (cf. ball-and-stick representations a)): polar head group of cation (P-IL (Cat)), red; polar anion (P-IL (An)), orange; non-polar alkyl-tail of cation (N-IL), green; polar head group of *n*-dodecanol (P-A), yellow; non-polar alkyl-tail of *n*-dodecanol (N-A), blue.[164]

The visualization of the subsets density distribution around a reference molecule is then achieved by generating so-called isosurfaces with the aid of the visual molecular dynamics program VMD.[165] Firstly, the position of the reference molecule within the Cartesian coordinate system has to be defined. In the case of the $[C_8C_1Im]^+$ cation, the reference plane is built considering the nitrogen atom carrying the octyl side chain as origin, locating the terminal carbon atom of the octyl chain on the x-axis and the carbon atom between the two nitrogen atoms of the imidazolium ring on the x-y-plane, while for the *n*-dodecanol molecule, the oxygen atom represents the origin, the carbon atom bound

to the oxygen atom is located on the x-axis and one of the hydrogen atoms bound to the aforementioned carbon atom is placed on the x-y-plane.

**Table 2.1** Isovalue ranges ($I_{min}$ - $I_{max}$) and chosen isovalues $I$ for SDFs isosurfaces. In case of the $[C_8C_1Im]^+$ cation, 90.58 % from the upper limit of the ranges for each subset are taken as final isovalue, while for the *n*-dodecanol 90.86 % are chosen.[164]

| | $[C_8C_1Im]^+$ | | | *n*-dodecanol | | |
|---|---|---|---|---|---|---|
| Color | $I_{min}$ | $I_{max}$ | $I$ | $I_{min}$ | $I_{max}$ | $I$ |
| red | $2.13 \cdot 10^{-6}$ | 1.98 | 1.79 | $1.18 \cdot 10^{-6}$ | 2.66 | 2.42 |
| orange | $5.51 \cdot 10^{-6}$ | 3.15 | 2.86 | 0 | 2.01 | 1.83 |
| green | $1.24 \cdot 10^{-5}$ | 1.94 | 1.76 | $1.17 \cdot 10^{-7}$ | 1.60 | 1.45 |
| blue | $2.74 \cdot 10^{-6}$ | 0.42 | 0.38 | $5.04 \cdot 10^{-8}$ | 0.44 | 0.40 |
| yellow | $3.53 \cdot 10^{-6}$ | 0.41 | 0.37 | $2.72 \cdot 10^{-6}$ | 1.11 | 1.00 |

Next, the extend of the isosurface can be controlled by the isovalue, which has to lie within a certain range, as can be seen in Table 2.1. Here, an isovalue approaching zero considers the density within the whole simulation box, while a higher value leads to an isosurface considering only the density distribution of a subset very close to the observed molecule. The range is dependent on the number of entities contributing to the density distribution, which is why for IL subsets (red, orange and green) the ranges are significantly wider than for the the alcohol subsets (blue and yellow). Nevertheless, to reach a comparable isosurface representation for each subset, the same percentage from the upper value limit of each range has to be considered. For a detailed description and interpretation of the SDFs see section 4.3.

### 2.3.3 Domain analysis

The domain analysis function in TRAVIS[15] enables the quantification of structural motives that can form in liquids, based on simple geometric criteria. Basis for this type of analysis is the Voronoi tessellation, originally developed as a mathematical construct for the partition of a plane into regions close to each of a given set of objects.[166] In the simplest case, these objects are just finitely many points in the plane (also called Voronoi

sites). For each site there is a corresponding region consisting of all points of the plane closer to that site than to any other. These regions are called Voronoi cells. Of course this procedure can be applied for three-dimensional systems, as well and it is therefore suitable for an atomistic simulation. In this case, the nuclear coordinates of all atoms in the system $N$ are taken as Voronoi sites $s_i$ in order to dissect the whole simulation box into individual Voronoi cells $C_i$:

$$C_i = \left\{ \mathbf{x} \in \mathbb{R}^3 \;\middle|\; (\mathbf{x} - \mathbf{s}_i)^2 \leq (\mathbf{x} - \mathbf{s}_j)^2 \, \forall \, j \neq i \right\} \tag{2.66}$$

According to equation 2.66, the Voronoi cell $C_i$ consists of all points $x$ that are closer to site $s_i$ than to any other site. With this approach, however, the Voronoi tessellation equally divides the space between two atoms irrespectively of their kind. This strongly contradicts the true chemical situation, because in O-H bonds, for example, the oxygen atom demands a relatively larger space than the hydrogen atom. To overcome this problem, an extended version of the Voronoi tessellation is introduced, the radical Voronoi tessellation.[167,168] In this scheme, a radius $r_i$ is assigned to each site $s_i$ and the distance between a given point and a site from the original Voronoi tessellation is replaced by the power distance to spheres around the sites with the corresponding radii:

$$C_i^{\mathrm{r}} = \left\{ \mathbf{x} \in \mathbb{R}^3 \;\middle|\; (\mathbf{x} - \mathbf{s}_i)^2 - {r_i}^2 \leq (\mathbf{x} - \mathbf{s}_j)^2 - {r_j}^2 \, \forall \, j \neq i \right\} \tag{2.67}$$

Consequently, the position of the face between two atoms is determined by the difference of the squared radii. It has been shown that taking the van der Waals radii for each atom reflects the typical intra- and intermolecular distances in liquids with high accuracy.[169–171] Applying the radical Voronoi tessellation based on the van der Waals radii already lead to successful results for determining partial atomic charges in systems with significant charge transfer,[63] or even for calculating bulk-phase vibrational spectra with good agreement to experimental results.[83,84,172–174]

Before performing a domain analysis, the molecules of the observed system are divided into subsets, analogously to the procedure for the SDF calculation described in subsection 2.3.2. In this way, based on the radical Voronoi tessellation and the afore specified

subsets, a domain is defined as follows: first the atomar Voronoi cells $C_i^{\mathrm{r}}$ are summed up for each subset to create subset-specific cells. Those kind of subsets belong to the same domain if their cells share a common face. Hence, the average number of domains present in the liquid is obtained, which is denoted as domain count $N_{\mathrm{Dom}}$. Any $N_{\mathrm{Dom}}$ value smaller than the total number of the particular subsets that constitute it, represents a certain aggregation in the system. If $N_{\mathrm{Dom}} = 1$, it means that the according subsets form a single, large, continuous microphase that stretches through the system. Next to the domain count, also a domains volume $V_{\mathrm{Dom}}$ and surface area $A_{\mathrm{Dom}}$, as well as the isoperimetric quotient $Q_{\mathrm{iper}}$ are calculated for each time step and averaged over the whole trajectory. $Q_{\mathrm{iper}}$ is a measure for how spherical a domain is and can be calculated via:

$$Q_{\mathrm{iper}} = \left(\frac{r_{\mathrm{Sphere}}(V)}{r_{\mathrm{Sphere}}(A)}\right)^6 = \left(\frac{\sqrt[3]{\frac{3}{4\pi}V}}{\sqrt{\frac{1}{4\pi}V}}\right)^6 = \left(6^{\frac{1}{3}}\pi^{\frac{1}{6}}\frac{V^{\frac{1}{3}}}{A^{\frac{1}{2}}}\right)^6 = 36\pi\frac{V^2}{A^3}. \tag{2.68}$$

Thus, if a domain is perfectly spherical, $Q_{\mathrm{iper}}$ equals one, otherwise $Q_{\mathrm{iper}}$ is smaller than one. The greater the deviation from one is, the less spherical is the domain.

Since the Voronoi tessellation defines surfaces for the subsets, it is also possible to calculate how much of the surface of each subset is covered by any of the subsets in the system, for an even deeper understanding of the interacting units.

# 3 Inorganic material synthesis in ionic liquids

As mentioned in chapter 1, the energy turnaround strongly affects the chemical synthesis of materials. On the one hand side completely new materials with outstanding properties are required, on the other hand the production of well-known and already used materials needs to become more resource-efficient in terms of raw materials and energy. Therefore, chemical processes have to be conceived and developed, which do not only allow for higher purity and yield but also produce less waste and work at lower temperatures.

One highly important strategy in this context is the development and establishment of alternative solvents for chemical synthesis.[33,175] So far, the most common solvents for conducting material synthesis are aqueous or organic media.[175,176] Water is readily available, environmentally benign, non-flammable and non-toxic, but its liquid range is only narrow (0 to 100 °C) and most organic molecules possess a low water solubility. Organic solvents in general possess diverse physicochemical properties with respect to density, polarity, solubility and liquidus range, but most of them have a low boiling point and high vapor pressure, and the solubility of inorganic compounds in these solvents is rather low.[176] Moreover, some organic solvents are highly toxic, flammable and even explosive, which in combination with their high volatility can cause serious environmental problems. Traditional molten salts have also been considered as alternative reaction media,[177,178] however, their high boiling points make their handling highly impractical and thus significantly constrain their scope of applications.

Ionic liquids can be considered as a family of molten salts, but they are clearly different from their traditional analogs. The most striking properties in the context of material synthesis are their low melting points (below 100 °C) and high thermal stabilities (up to 300 °C), providing a wide liquidus range, their negligible vapor pressure, which minimizes

the pollution of the environment with toxic substances, as well as their tunability and capability to dissolve versatile types of materials (cf. section 1.1). Additionally, due to their unique structural properties discussed in section 1.2, ILs can even function as templates and precursors to inorganic materials. This makes ionic liquids particularly promising candidates as alternative solvents and has already lead to immense academic interest in studying at or near room-temperature material synthesis in these solvents.[33,175,179–190] Even though ILs were already successfully used for the synthesis of many different materials, the working principles and interactions between the solvent and the material to be synthesized as well as the first mechanistic steps of the reaction up to the material growth on the molecular level are in many cases far from being understood.

Since such complex, small-scale processes are difficult to elucidate experimentally, theoretical methods clearly provide the most appropriate way to gain insight. In this case, ab initio molecular dynamics simulations represent the method of choice, because here the electronic structure of the system is treated explicitly, allowing for investigating the diverse interatomic interactions as well as observing qualitative changes of the bonding pattern in the course of the simulation.

The following study builds up on the tellurium bromide ($Te_2Br$) material synthesis, which in contrast to a former strategy could be performed at lower temperature and less time using a mixture of 1-butyl-3-methylimidazolium chloride mixed with aluminum chloride ($[C_4C_1Im][Cl]\cdot 1.3AlCl_3$). By performing AIMD simulations on model systems composed of a chain-like $Te_4Br_2$ molecule solved in either pure 1-ethyl-3-methylimidazolium chloride ($[C_2C_1Im][Cl]$) or the 1-ethyl-3-methylimidazolium chloride/aluminum chloride mixture ($[C_2C_1Im][Cl]\cdot 1.3AlCl_3$), it is aimed to reveal the role of $AlCl_3$ and the degree of microheterogeneity within the IL and its effects on the solvent structure and the solvation of the $Te_4Br_2$ molecule, as well as to investigate the first steps of the reaction of the $Te_4Br_2$ molecule to eventually form the $Te_2Br$ material. Since the cost of an AIMD simulation is directly related to the size of the system to be simulated, only 64 ion pairs of the IL and accordingly 83 $AlCl_3$ molecules, with reducing the length of the alkyl side chain attached to the imidazolium cation from a butyl group to an ethyl group, were taken into consideration. This was considered to represent a good compromise between

computational effort and a realistic description of the chemical situation as it is in the experimental setup.

Overall, this study serves as a good example of how theoretical simulations and the subsequent application and combination of appropriate analysis functions provide insight into the molecular level processes occurring during the inorganic material synthesis in ionic liquids.

# Theoretical investigation of the $Te_4Br_2$ molecule in ionic liquids

Roman Elfgen[*†], Oldamur Hollóczki[*], Promit Ray[*], Matthias F. Groh[‡], Michael Ruck[§¶] and Barbara Kirchner[*]

*First published: 19 December 2016*
*DOI: 10.1002/zaac.201600342*

Reprinted with permission from:
R. Elfgen, O. Hollóczki, P. Ray, M. F. Groh, M. Ruck and B. Kirchner, *Theoretical Investigation of the $Te_4Br_2$ Molecule in Ionic Liquids*, Z. Anorg. Allg. Chem. (2017) 643, 41–52.



[*]Mulliken Center for Theoretical Chemistry, Institut für Physikalische und Theoretische Chemie, Rheinische Friedrich-Wilhelms-Universität Bonn, Beringstraße 4+6, 53115 Bonn, Germany
[†]Max Planck Institute for Chemical Energy Conversion, Stiftstr. 34-36, D-45413 Mülheim an der Ruhr, Germany
[‡]Department of Chemistry and Food Chemistry, Dresden University of Technology, D-01062 Dresden, Germany
[§]Department of Chemistry and Food Chemistry, Dresden University of Technology, D-01062 Dresden, Germany
[¶]Max Planck Institute for Chemical Physics of Solids, Nöthnitzer Str. 40, 01187 Dresden, Germany

**Contributions to the manuscript**

- Running the ab initio molecular dynamics simulations
- Analysis of the trajectories
- Discussion of the results
- Writing the manuscript

**Abstract.** Material synthesis in ionic liquids, at or near room temperature, is currently a subject of immense academic interest. In order to illuminate molecular-level details and the underlying chemistry, we carried out molecular simulations of a single $Te_4Br_2$ molecule dissolved in ionic liquid, 1-ethyl-3-methylimidazolium chloride, as well as in ionic liquid mixed with aluminum chloride. Although the ethyl side chain is much too short to show detailed microheterogeneity, significant structuring with the small chloride anions is seen in case of the pure ionic liquid. In the case of the mixture, formation of larger anionic clusters is distinctly observed and analyzed. Due to the tendency of ionic liquids to dissociate, there is a pronounced shift to elongated Te-Br distances in both investigated solvents. However, only in the $AlCl_3$-containing liquid, we observe the reaction of the open chain-like $Te_4Br_2$ molecule to a closed square-like $Te_4Br^+$ and $AlCl_3Br^-$ ion. The molecular geometry of the $[Te_4]^{2+}$ unit shows negligible deviation from that in the experimental crystal structure.

**Keywords:** Ionic liquids, molecular dynamics simulations, electronic structure, $Te_2Br$ molecule, low temperature reaction

## 3.1 Introduction

Ionic liquids (ILs)[13,191–194] are salts in the liquid state, usually composed of organic cations, weakly basic organic or inorganic anions with attached side chains which can, in turn, be functionalized[195]. The nature of the ions greatly influences the physicochemical behavior of an IL[196,197] allowing for the tunability of several fundamental properties. A diverse selection of cations and anions[13] allows one to obtain the desired property in principle, thus facilitating their use as 'designer solvents'.

Design and development of completely new chemical processes at room temperature, with relatively low negative impact on the environment, are extensively in demand in view of the current energy scenario. ILs are attractive alternatives to many conventional organic solvents, because of both their low toxicity and the aforementioned tunability of properties.[198] ILs are particularly promising when it comes to their application as reaction media for chemical synthesis of materials. Preliminary results, such as the synthesis of

semiconductors, have already shown that various inorganic materials[179] can be produced, within ILs, at near ambient conditions. Refs[33,180–189] provide an excellent introduction to the synthesis and development of inorganic materials in ILs.

A prominent example, in this regard, is the synthesis of highly stoichiometric tellurium bromide ($Te_2Br$). Former synthesis from the elements was carried out at 220–260 °C (493–533 K) with subsequent annealing at 350 °C (623 K), quenching followed by annealing for several weeks at 165 °C (438 K). The product could then be obtained by iteratively extracting it from the solid solution via organic solvents.[199] In contrast, it was possible to synthesize phase pure $Te_2Br$ at room temperature within five days, using the IL, 1-butyl-3-methylimidazolium chloride, with aluminum chloride $[C_4C_1Im][Cl]\cdot 1.3AlCl_3$.[200] The crystal structure of $Te_2Br$ shows condensed, infinite double zig-zag chains of tellurium, forming a ribbon of boat-shaped rings with the ribbons saturated by bridging bromine atoms.[200]

Thus, it has been demonstrated that near-room-temperature synthesis in ILs can be applied successfully in order to derive inorganic compounds. However, the precise mechanism of this reaction and the role of the IL, on the formation and the growth of the molecules, are not yet understood in detail. It is reasonable to assume that the formation of infinite double chains of tellurium does not occur instantly, but is instead based on the previous formation of smaller clusters.

Tellurium is well-known for its large variety of polycations, several of which can be synthesized in ILs.[185,188,200–205] Furthermore, utilization of ILs can lead to extraordinary physical properties: $Te_4[Bi_{0.67}Cl_4]$ obtained from a classic gas-phase transport reaction is a semiconductor. However, transition to an IL-based synthesis yielded the closely related compound $Te_4[Bi_{0.74}Cl_4]$, which proved to be a one-dimensional metal and type-I superconductor.[201,202] In particular, three different ternary compounds (and polycations) can be synthesized in the Lewis-acidic IL $[C_4C_1Im]Cl \cdot nAlCl_3$ (n = 1.3-1.5): the already mentioned $Te_4[Bi_{0.74}Cl_4]$[201,202] as well as the closely related semiconductors $Te_4[Bi_6Cl_{20}]$ and $Te_8[Bi_4Cl_{14}]$.[200] Without bismuth in the system, $Te_4[AlCl_4]_2$ is yielded under the same conditions.[203] Introduction of bromine leads to crystallization of $Te_2Br$,[200] while $Te_4[Al_2Cl_7]_2$ has been synthesized under altered conditions in the presence of iodine and

phosphorus.[200] Introducing other anions leads to $Te_6[WOCl_4]_2$[203] and $[Te_8]_2[Ta_4O_4Cl_{16}]$, the latter being synthesized in an aluminum halide free system.[206] An approach other than chemical oxidation of elemental tellurium was established by Beck and coworkers:[204,205] Exploiting the known suitability of ILs as electrolytes resulted in the synthesis of tellurium polycations via anodic oxidation of elemental tellurium. $Te_4[CTf_3]_2$, $Te_6[OTf]_4$ and $Te_8[NTf_2]_2$ were obtained, depending on the chosen IL and voltage.[204,205] In the case of $[Te_4][CTf_3]_2$, containing the relevant $[Te_4]^{2+}$ cluster, Te-Te bonds of 267.0 and 266.7 pm and angles of 87.91° and 92.02° were found, indicating a small deviation from a square shape. It is discussed that this distortion to a rhombus arises from donor-acceptor interactions between the highly electrophilic cationic cluster and the oxygen atoms of the surrounding $[CTf_3]^-$-anions.

Corbett and coworkers investigated the crystal structures of $[Te_4][AlCl_4]_2$ and $[Te_4][Al_2Cl_7]_2$, both containing $[Te_4]^{2+}$ clusters.[207] Both compounds were prepared from a mixture of Te, $TeCl_4$, and $AlCl_3$ with differing compositions. Three-dimensional X-ray diffraction was used to show that planar $[Te_4]^{2+}$ clusters occur within both crystals. In the case of $[Te_4][AlCl_4]_2$, Te-Te bond lengths of 267.38 and 266.33 pm and angles of 89.90 and 90.10° were respectively observed, while for $[Te_4][Al_2Cl_7]_2$, Te-Te distances of 265.99 and 266.10 pm and angles of 89.81 and 90.19° were found. Newer measurements of the structure, carried out via X-ray structure elucidation on single crystals obtained from IL-based syntheses, revealed virtually the same atomic coordinates compared to the classic synthesis.[200,203] It is interesting to consider the possible presence of these tellurium clusters in the mechanism of $Te_2Br$ synthesis.

In order to reveal the mechanisms underlying the synthesis of inorganic substances in ILs, an understanding of the molecular-level interactions, within such polycationic clusters as well as between the clusters and the solvent, is required. Since such complex small-scale effects are nearly impossible to elucidate experimentally, theoretical methods provide the most appropriate way to gain insight on the molecular level. Ab initio molecular dynamics (AIMD) simulations represent the method of choice in this case because, in these simulations, the basic idea is to compute the forces that are acting on the nuclei from electronic structure calculations on the fly as the trajectory is generated. In this way,

the electronic variables are considered as active degrees of freedom. In contrast to classical MD, this enables the investigation of a myriad of different interatomic interactions, arising from many different atom types and the observation of qualitative changes of the electronic structure, and thus the bonding pattern in the course of the simulation. This simultaneously implies that the approximation is shifted from selecting a model potential (i.e., classical MD) to selecting a particular theoretical approximation.

Within this work, we focused on the $Te_2Br$ synthesis in ILs, according to the experimental approach followed by Ruck and coworkers.[200] It is aimed to characterize the influence of the Lewis-acidic $AlCl_3$ on the formation and the growth of the $Te_2Br$ particles and to reveal the mechanism of this chemical reaction by applying state-of-the-art theoretical approaches in order to gain detailed insight into the synthesis on a molecular level.

## 3.2 Computational methodologies

### 3.2.1 AIMD simulations

To investigate the influence of the Lewis-acidic $AlCl_3$ on the structure and the solvation of the $Te_4Br_2$ molecule, two systems (Figure 3.1) were taken up for study.

In the first system, denoted **A**, a $Te_4Br_2$ molecule was simulated within the ionic liquid $[C_2C_1Im][Cl]$, with 64 ion pairs taken into consideration. For the second system, denoted **B**, 83 $AlCl_3$ molecules were added to 64 ion pairs of $[C_2C_1Im][Cl]$ to form the solvent for a $Te_4Br_2$ molecule. The number of $AlCl_3$ molecules corresponds to the 1.3:1 ($AlCl_3$:IL) concentration chosen by Ruck and coworkers for the experimental near-room-temperature synthesis of $Te_2Br$.[200] We choose to simulate the ethyl chain instead of the butyl chain for the IL compounds, so as to lower the demand on the computational resources. With the aid of the program PACKMOL[208,209], the solvent components of the investigated systems were first placed into cubic simulation boxes, choosing an edge length of 2430.10 pm for the first system and 3006.22 pm for the second one in order to reproduce their experimental densities. PACKMOL creates a starting geometry for MD simulations by packing molecules in defined regions of space. The packing guarantees that short range repulsive interactions do not disrupt the simulations. The software allows the definition of the

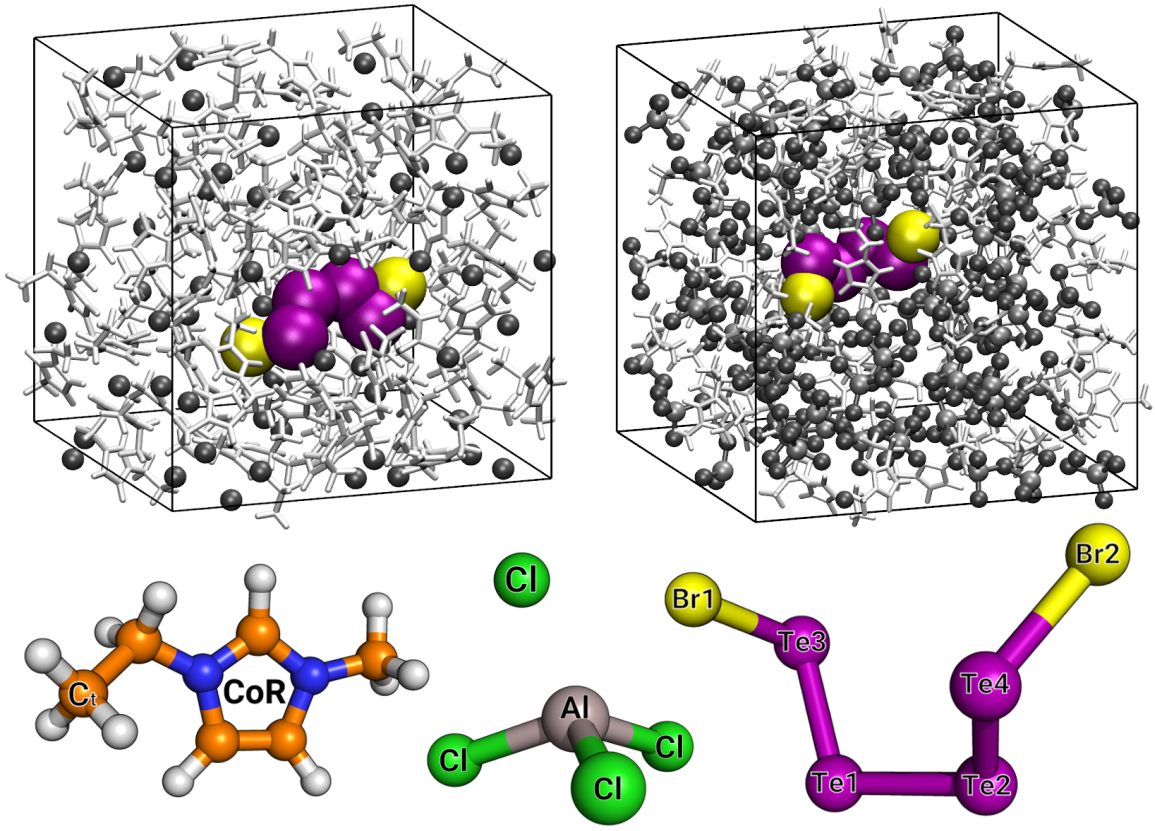


**Figure 3.1** Snapshots of simulation boxes showing the composition and size of both observed systems. Left: System **A**, $Te_4Br_2$ in $[C_2C_1Im][Cl]$, edge length of simulation box $a = 2430.10$ pm; Right: System **B**, $Te_4Br_2$ in $[C_2C_1Im][Cl]{\cdot}1.3AlCl_3$, edge length of simulation box $a = 3006.22$ pm. Underneath, the labeling of relevant atoms and positions of the solvent components and their geometry is shown. In the case of the $Te_4Br_2$ molecule, initially an open or chain-like form is assumed.

molecular system by packing different types of molecules into regions defined by geometric constraints. Function and gradient evaluations are optimized to the point that a number of atoms can be packed in a reasonable time, and initial configurations for state-of-the-art simulations can be built in few minutes or even seconds. The only requirements are the structures of one molecule of each type and the geometrical constraints that must be fulfilled in order to generate a reasonable structure. It is possible to generate starting structures of mixtures of several components, solvated proteins, and build ordered arrangements as double layers or micelles. In addition to the solvents, an optimized $Te_4Br_2$ particle, in the open or chain-like form (see Figure 3.1), was inserted into the previously created simulation boxes of the pure ILs, followed by a few steps of energy minimization.

The chain-like structure was chosen because it turned out to be the more stable structure provided by gas phase calculations on the isolated molecules.

In order to compare the complex behavior of the $Te_4Br_2$ molecule within the two different solvents, the same simulation method with the same setup was chosen; AIMD simulations were carried out with density functional theory (DFT) within the CP2K [152] program package using the QUICKSTEP module [154]. Here, the hybrid Gaussian and plane waves (GPW) approach is used to calculate the energies and forces on the atoms. The molecularly optimized double-$\zeta$ basis set (MOLOPT-DZVP-SR-GTH) [210] was applied to all atoms together with the revPBE functional and the corresponding PBE Goedecker–Teter–Hutter pseudopotentials for core electrons [155–157]. A 280 Ry density CUTOFF criterion with the finest grid level was employed, together with multigrids number 5 (NGRID 5 and REL_CUTOFF 30) using the smoothing for the electron density (NN10_SMOOTH) and its derivative (NN10). [154]

Dispersion interactions were accounted for by using the DFT-D3 type of a pair potential van der Waals density functional. [115,116] For the SCF calculation, the default value (1.0E-5) was used as target accuracy for the SCF convergence. The DIIS minimizer [152] was used to reach a faster orbital transformation via direct inversion in the iterative subspace. The maximum number of SCF iterations to be performed for one iteration was set to 100 while a maximum of 10 iterations was performed for outer SCF loops.

In order to observe and analyze the temporal development of the systems over time, MD simulations were carried out applying periodic boundary conditions in order to avoid boundary effects. The canonical (NVT) ensemble was used with the aid of the Nosé–Hoover-chain thermostats [211,212] with a time constant of the thermostat chain of 50. Both systems were equilibrated over 5 ps defining the keyword REGION MASSIVE to achieve faster equilibration. The temperature was set to 450 K in order to increase the sampling. For the following production runs, the temperature was kept at 450 K with one MD iteration comprising 100000 steps with a time step of 0.5 fs.

For our simulations the following considerations should be kept in mind. The simulation boxes were created by inserting the $Te_4Br_2$ molecule into the two liquids, which increases the density by maximum 3 %. Considering the higher density of $Te_2Br$ crystal

(5.8 g·cm$^{-1}$), one could expect a slight increase in the density compared to the pure liquid upon mixing, compensating for this density deviation. In order to estimate a possible effect, one can refer to the compressibilities of ILs, which are in general in the same range as that for water (see extensive work of Brennecke[213]). Therefore, a comparison to water seems reasonable. Given the compressibility of liquid water is $\approx 5\times10^{-10}$ Pa$^{-1}$, a 3 % volume decrease may lead to a pressure increase up to 60 MPa.

Since we are discussing in this article with the determination of the solvation modes of the molecule in the ionic liquid, we should consider the effect of such a high pressure or of the density on the structure of the liquid. For the effect of the density on the structure we refer for example to the work of Yoshida et al.,[214] who investigated the temperature and density dependence of molecular and thermodynamic properties of water in the entire fluid region including the autoionization processes. They demonstrated within their study the effect of the density change on the RDFs between water molecules. It is visible from Ref.[214] that in the case of the RDFs for the O-O distances, decreasing the density for 50 % (from 1.000 to 0.500 g·cm$^{-3}$) results in a shift of the first peak no more than 10 pm towards higher distances. In the case of the O-H, H-O and H-H distances, the shifts are even significantly smaller or not observable at all. Further, a study of the pressure effects on the structure of water by Urquidia[215] showed that increasing the pressure at room temperature to 100 MPa leads to a negligible change in the water structure. Not even increasing the pressure to 770 MPa affects the location of the first peak, only the depth of the first minimum shows notable effects. Furthermore, keeping in mind that in AIMD all particles perceive all interactions, thus many-body effects are included, it can be further assumed that less errors will be introduced in an AIMD as compared to traditional classical simulation based on pair potentials. Thus, it has been shown by Huber and coworkers that under high pressure many body effects are more important to be included in the simulations[216,217] than at standard conditions.

### 3.2.2 Static calculations

For all quantum chemical calculations, we used the TURBOMOLE[218] version 7.0.2 and the ORCA[219] version 3.0 programs. We calculated three structures, i.e., a chain-like and

a square-like conformation of $Te_4Br_2$ and the $[Te_4]^{2+}$ square, see Figure 3.9. Firstly, we optimized all structures with the SV(P) basis set and standard effective core potential on Te,[220] and the PBE functional employing the resolution of identity approach[218] and the Grimme D3 dispersion correction[115,116] with standard criteria within the TURBOMOLE package.[218] Upon this, we applied the PBE-3c composite functional of Grimme et al.[220–222] with a tightSCF criteria in ORCA.[219] In the next step, optimization was performed using the PBE0 functional, again with tightSCF criteria. All optimizations in ORCA were checked for convergence to true minima. We carried out the calculations in restricted and unrestricted (with multiplicity 1 and 3) Kohn-Sham density functional theory. Upon the lowest energy structure, which was always either the singlet unrestricted or the restricted calculation, we carried out single point calculations. To allow for an orbital analysis, we fixed the dihedral angle of the $[Te_4]^{2+}$ and optimized the structure with PBE0-D3 and the SV(P) basis set under $C_2$ symmetry. Subsequently, we added a simple Hartree–Fock calculation with a SV(P) basis set.

### 3.2.3 Analysis

Our open source program TRAVIS (Trajectory Analyzer and Visualizer) was used to examine the temporal development of the simulated systems.[86] This powerful tool enables the time-dependent investigation of structural features of the solvent and the solute, intra- and intermolecular interactions within or between the components and the elucidation of chemical reaction mechanisms by calculating different distribution functions (DFs) between relevant atoms and positions of the observed systems. The most used features are radial distribution functions (RDFs) and distance distribution functions (DDFs), which are visualized with the aid of the program gnuplot (version 5.0)[223] for the generation of two- and three-dimensional plots of functions, data, and data fits or with the xmgrace software[224].

Cluster analysis, to identify the presence of $Al_2Cl_7^-$, $Al_3Cl_{10}^-$ and larger clusters, was performed with the aid of self-developed FORTRAN programs. Clusters were defined purely based on geometric criteria, determined primarily from Al-Al and Al-Cl RDFs. The analysis is based on the fact that the presence of an Al-Cl-Al bridge uniquely defines

a cluster and is, therefore, enough to distinguish between accidental closeness of atoms and long-term bonds. To characterize the presence of Al-Cl-Al bridges, Al-Cl distances were considered up to a cut off of 240 pm along with an Al-Al distance of up to 445 pm in combination with an Al-Cl-Al angle between 90 and 140°. The criteria were carefully chosen so as to eliminate occurrences of an isolated $AlCl_3$ molecule approaching a cluster being counted as a dimer. For the characterization of $Al_3Cl_{10}^-$ clusters, an Al-Al distance of up to 445 pm, in combination with Al-Al-Al angles greater than 90°, was found to be adequate. This combination of criteria allows one to uniquely identify $Al_3Cl_{10}^-$ clusters as verified by looking at the number of $Al_3$ clusters and atomic indices of the Al atoms from the respective Al-Cl-Al bridges. Subsequently, we proceed to identify the number of $Al_2Cl_7^-$ clusters. In this case, a distance cut-off of 445 pm results in several Al-Al combinations which are not connected through a bridging Cl atom. These correspond to $AlCl_3$ or $AlCl_4^-$ species approaching each other to form larger clusters. For the sake of completeness, the number of such occurrences was evaluated but is not detailed in the manuscript. Further, the number of unique such Al-Al combinations is also discussed by accounting for those combinations which are actually part of $Al_3$ clusters. The number of such bridges belonging uniquely to $Al_2$ clusters, were evaluated by keeping a count of Al-Cl-Al bridges corresponding to $Al_3$ clusters. These numbers showed negligible deviations from the number of $Al_3$ clusters isolated purely from Al-Al distances and Al-Al-Al angles. The number of free $Cl^-$ and $AlCl_3$ species are also evaluated by considering an Al-Cl cut-off distance of 300 pm.

## 3.3 Results and discussion

### 3.3.1 Solvent structure

Before investigating the structure and solvation of the $Te_4Br_2$ molecule within both solvents, we first examine the structure of the solvent in order to gain detailed insight into its governing principles and the fundamental interactions on the molecular level. To achieve this, RDFs were calculated between different relevant atoms and positions of the solvents' components (Figure 3.1) and compared with regard to the particular system.

It is well known that ILs containing ions with attached large alkyl side chains, tend to form microheterogeneities.[8,9,11–13,225] This effect is based on the microscopic segregation of the ions' components into polar and non-polar phases.[15] Even though microheterogeneity is almost not observable for ethyl chains, as in the case of the $[C_2C_1Im]^+$-cation, we nevertheless distinguish between the center of the imidazole ring CoR and the terminal carbon atom $C_t$ of the ethyl side chain attached to the square, see Figure 3.1. In order to compare both solvents, in the case of the $AlCl_3$ containing system, the chloride and aluminum atoms are treated separately because it is not known a priori how many free $Cl^-$-anions, $AlCl_3$, $AlCl_4^-$, $Al_2Cl_7^-$ or even larger clusters are being formed and broken over time. Figure 3.2 shows the RDFs between different atoms and positions of the particular solvents.

In the case of system **A** (only chloride anions), the RDFs reveal a structuring which is typical for ILs composed of such ions. Due to the electrostatic attraction between oppositely charged ions, the curve depending on the CoR-Cl distances shows a significant first peak at approximately 450 pm and a broad second peak at approximately 950 pm. The RDFs for the CoR-CoR and Cl-Cl distances show quite similar shapes, with only their first broad maxima deviating from each other due to the size of the charge carrying unit, occurring at approximately the same distance as the minimum of the CoR-Cl curve ($\approx$ 700 pm). For very helpful discussions in a larger system studied by classical simulations and experiment, we refer the readers to the work of Castner, Margulis and coworkers[226]. The $C_t$-$C_t$ curve exhibits the first maximum below 400 pm, see blue curve in the upper panel of Figure 3.2. These findings indicate a structure where the polar components of the IL, namely the head group of the cation and the chloride anion, form a continuous, three-dimensional network. Within this network, a definitely charged unit is surrounded by units of the opposite charge in which the non-polar components, namely the terminal carbon atoms of the ethyl side chains attached to the cations, agglomerate due to van der Waals interactions and form small and finely dispersed micro-phases that coexist with the polar network, i.e., the first signals of microheterogeneity.[9,12,13]

In contrast, the RDFs for system **B** show a different course. In comparison to **A**, the Cl-Cl curve (black) shows a more intense first peak which is shifted towards lower distances

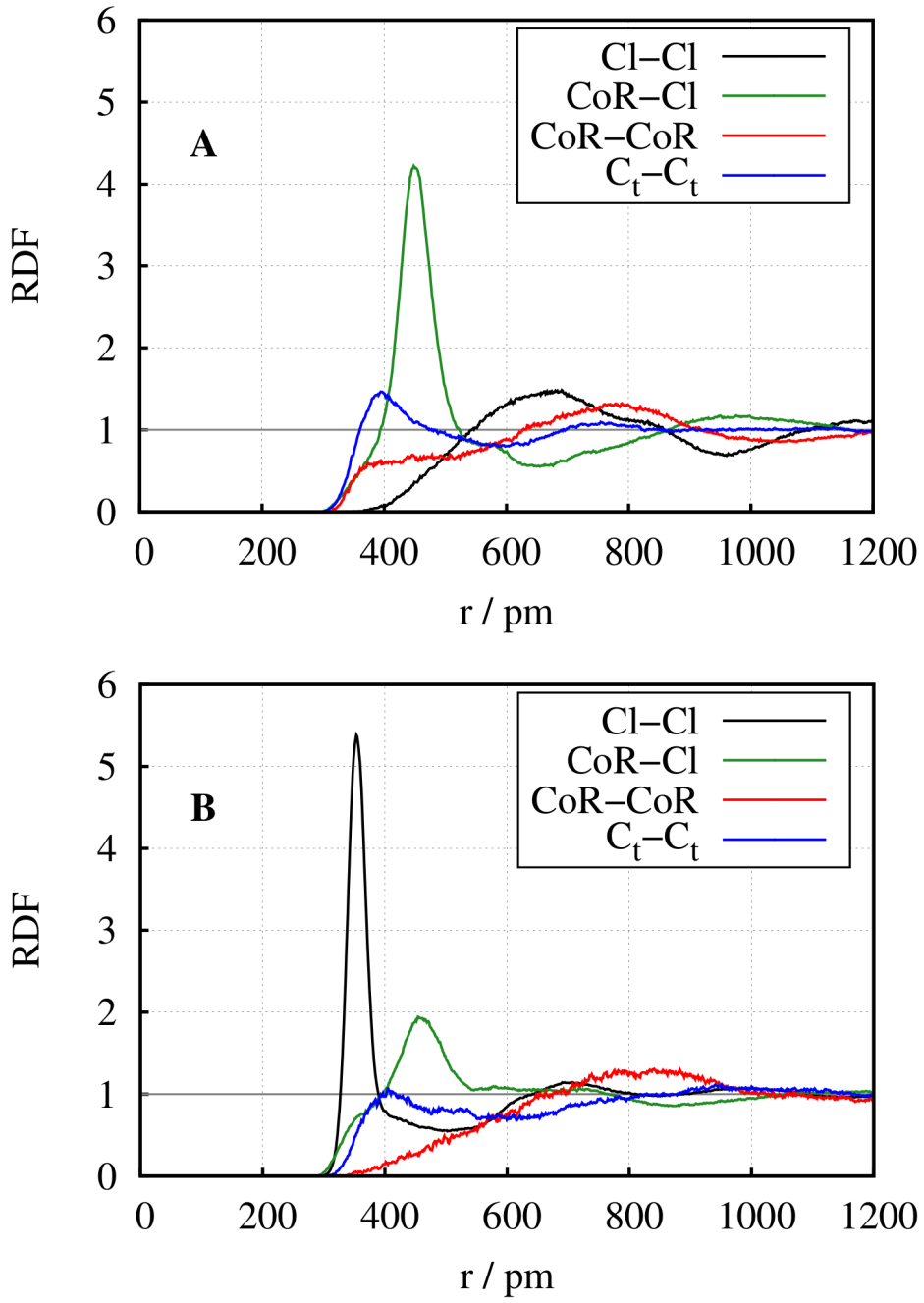


**Figure 3.2** RDFs depending on the Cl-Cl distances (black), the CoR-Cl distances (green), the CoR-CoR distances (red) and the $C_t$-$C_t$ distances (blue) for the $Te_4Br_2$ molecule within **A**: $[C_2C_1Im][Cl]$ and within **B**: $[C_2C_1Im][Cl]\cdot 1.3AlCl_3$.

($\approx$ 360 pm) between the atoms while the intensity of the CoR-Cl peak decreases significantly. The peak of the $C_t$-$C_t$ RDF exhibits only a slight decrease, while the CoR-CoR RDF shows a similar course compared to the other system. Obviously, these deviations can be traced back to the presence of $AlCl_3$ within the second solvent. Less obvious is

the decrease of the microheterogeneity, i.e., the decrease in the $C_t$-$C_t$ RDF. This has been observed and discussed previously by us[12] — that with increasing anion size, which is the case changing from system **A** to system **B**, the microheterogeneity decreases in ILs. Therefore, for system **B**, the RDFs between the Al and the different relevant atoms and positions of the available components are shown in Figure 3.3.

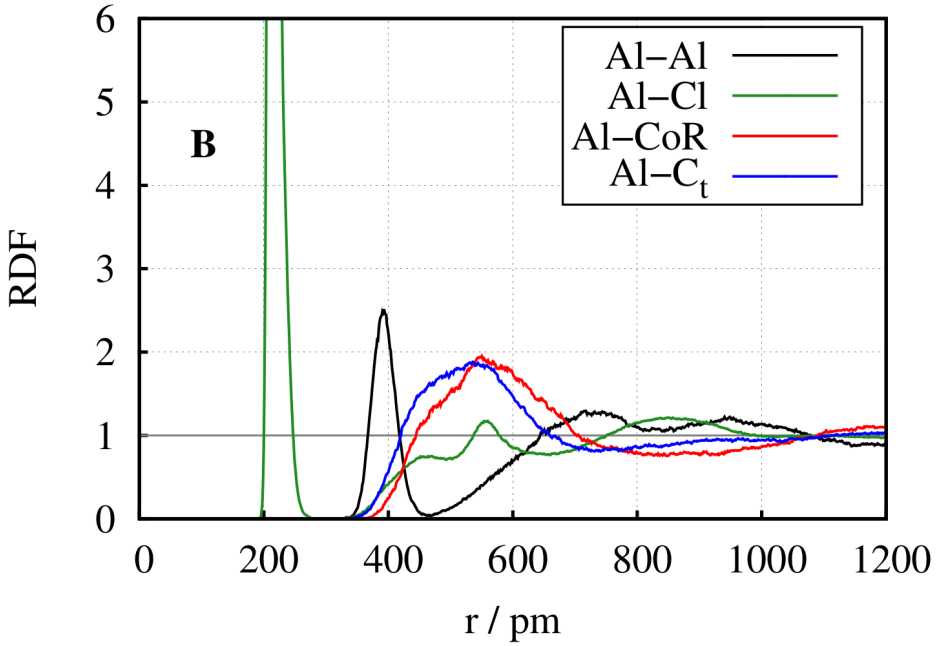


**Figure 3.3** RDFs depending on the Al-Al distances (black), the Al-Cl distances (green), the Al-CoR distances (red) and the Al-$C_t$ distances (blue) for the $Te_4Br_2$ molecule within **B**: $[C_2C_1Im][Cl]\cdot 1.3AlCl_3$.

Here, the curve for the Al-Cl distances shows a significant peak up to g(r) = 33 at 215 pm. This clearly indicates that most of the chloride atoms participate in the formation of anionic complexes, together with Al which is well-known for $AlCl_3$-based ILs with halide anions.[227] We verify later via our cluster analysis that this is indeed the case.

The peak corresponding to Al-Al distances of approximately 400 pm arises from Al atoms participating in one cluster. This distance corresponds to a structure in which two Al atoms are connected by a bridging Cl atom with a certain Al-Cl-Al angle.[227] In order to investigate the size of the forming clusters, we carried out an extended cluster analysis (Figure 3.4).

As already mentioned, in the case of trimers, it was observed that setting each of

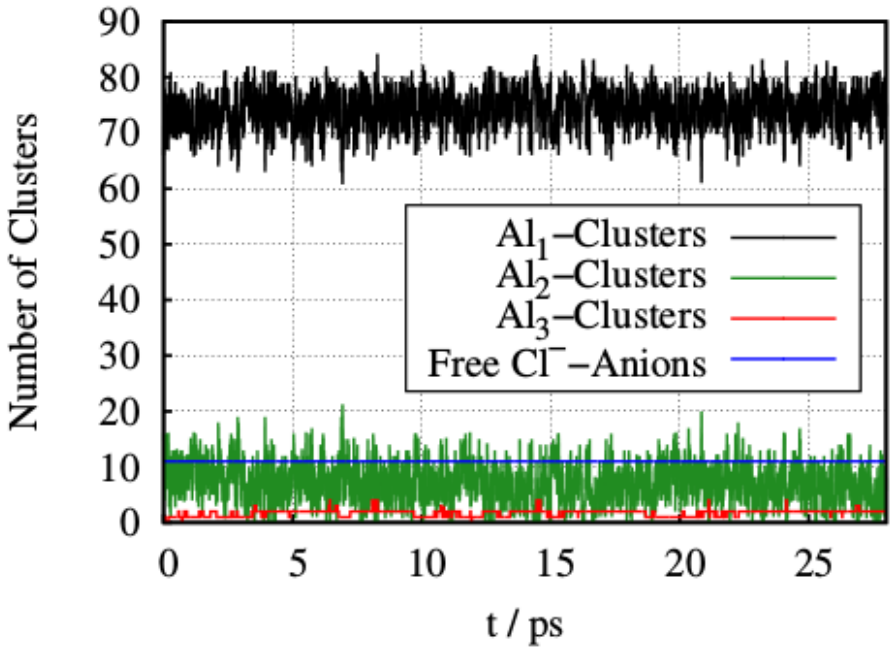


**Figure 3.4** Temporal development of Al-clusters and free $Cl^-$-anions based on the 83 available $AlCl_3$ molecules and 64 $Cl^-$-anions occurring in the system. Species containing only one Al atom are depicted in black, clusters of two Al atoms in green and clusters containing three Al atoms in red. On average 89.4 % of the Al atoms are part of an $Al_1$-cluster, i.e., $AlCl_3$ and $AlCl_4^-$, 8.5 % are part of an $Al_2$-cluster, i.e., $Al_2Cl_7^-$ and only 2.1 % are part of an $Al_3$-cluster, i.e., $Al_3Cl_{10}^-$.

the Al-Al distances to a limit of 445 pm and setting the Al-Al-Al angle to be obtuse could capture the clusters uniquely. In case of dimers, this condition was not sufficient and we reverted back to the Al-Cl-Al bridges and corrected for the presences of dimers within trimers. The number of $Al_1$ ($AlCl_3$ and $AlCl_4^-$), $Al_2$ ($Al_2Cl_7^-$) and $Al_3$ ($Al_3Cl_{10}^-$) clusters are plotted against simulation time in Figure 3.4. The average number of $Al_3$, $Al_2$ and $Al_1$ clusters are 2, 7 and 63, respectively, which can be compared to Øye et al.[228] The vast majority of Al atoms, over 75 % of the total Al atoms, exist as $Al_1$ species, which could correspond to either $AlCl_3$ or $AlCl_4^-$ species. However, almost all the $Al_1$ species exist in the anionic form. The total number of $Al_3$ clusters does not show major fluctuations with time, ranging between 1 and 4. There does not seem to be major bond rearrangements in the few $Al_3$ clusters; they are stable and reasonably long-lived as observed by following atomic indices of the relevant Al atoms. However, the total number of $Al_2$ clusters fluctuates significantly about the mean indicating Al-Cl-Al bond

rearrangements, characteristic of Grotthus-like diffusion as observed by us in a previous simulation of a different composition.[227] The Grotthus diffusion, initially only proposed to explain the diffusion of an excess proton in water, is now generally used to describe proton hopping mechanisms. Similar hopping mechanisms of atomic species are observed with $I^-$, $Cl^-$, in the context of larger complex anions. Interestingly, the number of Al-Al combinations identified from the preliminary distance criterion alone, as explained in the computational details, shows values between 23 and 27. These smaller fluctuations in the number of Al-Al combinations, within a distance of 445 pm, compared to the number of dimers, suggests that new clusters are formed from Al atoms approaching the existing clusters. This is verified by tracking atomic indices. Therefore, the average number of such combinations is 25, significantly higher than the average number of dimers present in the systems. The presence of $Al_2$ clusters is quite prominent, accounting for over 20 % of the total Al atoms on average, with regular changes in the Al atoms participating in their formation. The number of $Al_2$ clusters, on the other hand, exhibits a large range of values between 0 and 18. This is explained by the gradual approach of $AlCl_3$ molecules towards $Al_2$ clusters and subsequent bond rearrangements within the clusters.

Less than 6 % of the total Al atoms in the system exist as $Al_3$ clusters while larger anionic clusters with 4 Al atom units are only visible as transient species due to our distance and angle criteria. Furthermore, the number of free $Cl^-$ ions is small (11 on average) and remains constant with time.

### 3.3.2 $Te_4Br_2$ molecule in the ionic liquids

For investigating the behavior of the $Te_4Br_2$ molecule within both solvents, different aspects have to be considered. As a first approach, the temporal development of all relevant intramolecular distances between the atoms within the $Te_4Br_2$ molecule is compared for the two solvents. In order to distinguish between the four Te and two Br atoms respectively, the single atoms were labeled as shown in Figure 3.1 which shows the cluster in the open or chain-like structure, as inserted into the simulation box in the beginning of the simulations.

The upper two panels of Figure 3.5 show the relevant intramolecular distances between

the atoms of the $Te_4Br_2$ molecule that are initially directly bound to each other, while the lower two panels contain the Te3-Te4 distances (Figure 3.1).

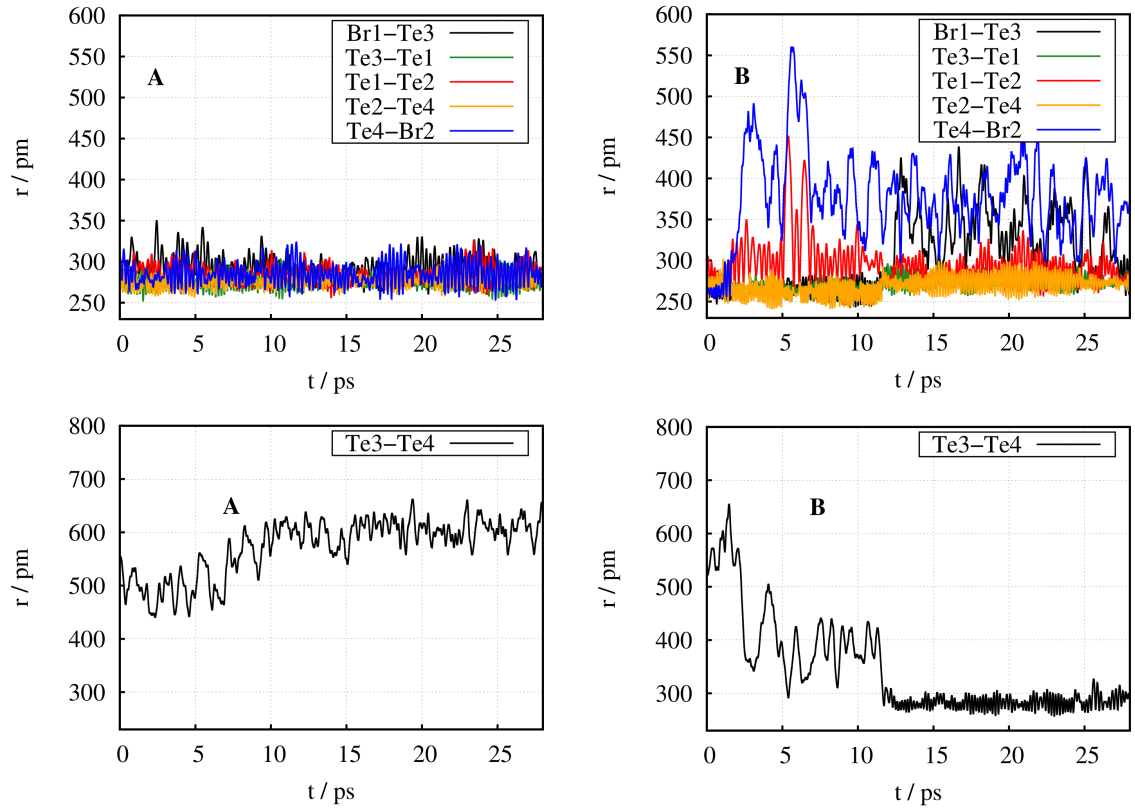


**Figure 3.5** Temporal development of intramolecular distances between the $Te_4Br_2$ molecules atoms within both solvents **A** (left panels) and **B** (right panels). The upper two panels show the distance development for initially directly bound atoms, i.e., Br1-Te3 (black), Te3-Te1 (green), Te1-Te2 (red), Te2-Te4 (orange) and Te4-Br2 (blue) and the lower two panels show the distance development for the initially unbound atoms Te3 and Te4.

Comparing the distances in both solvents, it is immediately apparent that the $Te_4Br_2$ molecule behaves differently in $[C_2C_1Im][Cl]$ (**A**) as compared to $[C_2C_1Im][Cl]{\cdot}1.3AlCl_3$ (**B**). For system **A**, the average distances between the atoms that are directly bound to each other, remain the same during the course of the simulation. This indicates that the $Te_4Br_2$ chain does not transform into a square. Small fluctuations in the distances are observed, with minimum values of 250 pm and maximum values of 350 pm, which can be assigned to the temperature dependent stretching vibrations within the molecule. The distance between Te3 and Te4 increases during the first 20 ps until it reaches an approximately constant value between 610 and 620 pm. Therefore, a slight stretching,

but no structural change of the molecule can be assumed.

In contrast, the distances for the $Te_4Br_2$ cluster in $[C_2C_1Im][Cl]\cdot 1.3AlCl_3$ show a different pattern. After a few time steps, the bond length between Te4 and Br2 increases on average, before it breaks at around 2.1 ps. From this point on, the distance between Te1 and Te2 starts to fluctuate strongly. At 5.4 ps, it amounts to more than 450 pm. However, the atoms always come back together up to the covalent bond distance. Moreover, after the Te4-Br2 bond grows, the distance between Te3 and Te4 drops significantly from around 560 pm to approximately 400 pm. The fluctuation in the Te1-Te2 distance and the approach of Te3 and Te4 are related to a structural change within the molecule. In the course of this structural change, after about 6.3 ps, on average the bond length between Te3 and Br1 also starts to increase slightly until it breaks at around 12.2 ps. Simultaneously, the distance between Te3 and Te4 drops again and a covalent bond is formed between these two atoms. From this point, the fluctuation of the Te1-Te2 bond length decreases, indicating that a four-unit ring or square-like structure of Te atoms has formed. This square is stable for the rest of the simulation time up to 28.0 ps. These results agree nicely with experimental findings. Upon mixing of tellurium, $TeCl_4$, and a Lewis-acidic IL, the solution turns immediately from colorless to dark violet indicating the fast formation of tellurium polycations.[203]

In order to reveal the particular reaction mechanism for the $Te_4Br_2$ molecule within $[C_2C_1Im][Cl]\cdot 1.3AlCl_3$, the following question needs to be answered: Do the Te-Br bonds break spontaneously or are the bromide ions abstracted by the surrounding solvent? To answer this question, distances are considered between the two bromide atoms and the four Te atoms, (Figure 3.6 upper panels) and between the bromide atoms and all Al atoms present in the system (Figure 3.6 lower panels).

The mechanism of the Br elimination will be revealed chronologically, starting with the Br2 atom (Figure 3.5). Considering the blue curve depending on the Br2-Te4 distances in the upper panel of Figure 3.6 and the orange curve for the distance between Br2 and one of the Al atoms of the system (Al no. 55), it can be observed that first an $AlCl_3$ molecule (formerly being an $AlCl_4^-$ anion) from the surrounding bulk phase approaches the molecules Br2 atom. As it reaches a certain distance, which lies in the area of a covalent

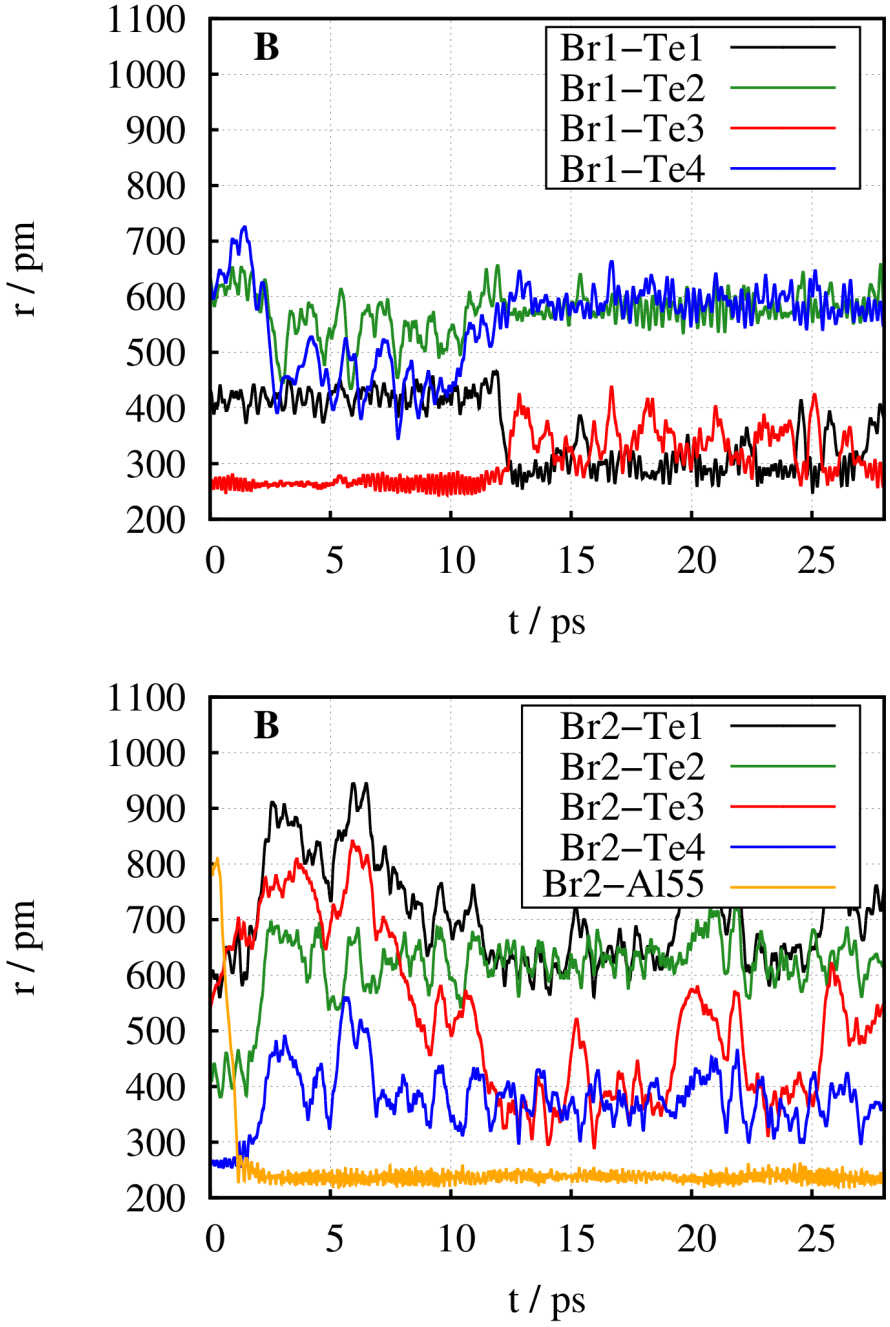


**Figure 3.6** Temporal development for intra- and intermolecular distances based on Br1 (upper panel) and Br2 (lower panel) as reference atoms for the $Te_4Br_2$ molecule within system **B**. The distances with Te1 as observed atom are depicted in black, with Te2 in green, with Te3 in red and with Te4 in blue. The graph for the Br2-Al55 distance is shown in orange.

bond distance, the Br2-Te4 bond is weakened and an intermediate state is formed, where the Br2 atom interacts with both the Al and the Te4. The duration of this intermediate

state is rather short, approximately 0.3 ps, before the Br2-Te4 bond breaks and $AlBrCl_3^-$ and $Te_4Br^+$ are formed. This behavior seems to be logical since there are not enough free chloride anions for all 83 Lewis-acidic $AlCl_3$, which tend to fill up their "lack" of electrons.[227] Thus, the Br2 atom is attacked in an electrophilic manner by one of the $AlCl_3$ molecules. However, the second bromide atom (Br1) still remains connected to the Te cluster. As seen before, after the Br2 elimination, the $Te_4Br^+$ undergoes a structural change. The formation of a four-unit ring or square of Te allows for the charge to delocalize over all ring atoms. We will come back to this point when we discuss the electronic structure of the molecule. The upper panel of Figure 3.6 shows that as soon as the ring is formed, the Br1 atom leaves the Te3, but only to bind to the Te1 atom. For the rest of the simulation the Br1 atom switches between the Te1 and the Te3 atoms and is not attacked by another $AlCl_3$ molecule which might be due to the short simulation time. Whether the Lewis-acidic abstraction by $AlCl_3$ is the only cause for the reaction or if there is also another driving force underlying will be discussed in the next sections.

### Particle structure analysis

For analyzing the driving force for the Br elimination, the structure of $Te_4Br_2$ molecule is investigated by calculating the average bond length $\bar{l}$ between its atoms and their respective standard deviations (SD). Table 3.1 shows the values for the observed molecule within system **B** ($[C_2C_1Im][Cl]\cdot 1.3AlCl_3$) and system **A** ($[C_2C_1Im][Cl]$) compared to dynamic gas phase simulations and static gas phase calculations of the molecule without any surrounding solvent.

For the analysis of the bond distances, a part of the simulation was picked in which the fluctuation of the distances is small and the molecule is stable and does not undergo a chemical reaction. In the case of $Te_4Br_2$ within $[C_2C_1Im][Cl]$ this was true for a time range between 10.0 and 28.0 ps, while for the solvent **B** a range between 12.2 and 28.0 ps was chosen (Figure 3.5). In the case of the static calculation of the square, a structure was considered in which the bromide atoms were attached to two oppositely arranged Te atoms. This is due to the fact that the geometry, in which the bromides are bound to two neighboring Te atoms, turned out to be unstable in the gas phase calculations due to its

**Table 3.1** Structure analysis of the $Te_4Br_2$ molecule from bulk phase simulations, dynamical gas phase simulations (using RKS and UKS-M1) and static gas phase calculations (using RKS for both a chain- and a square structure of the molecule). The particular pair distances $\bar{l}$ and their standard deviations (SD) are shown in pm. For system **A** the time range between 10.0 and 28.0 ps was chosen, while for the system **B** the range between 12.2 and 28.0 ps was chosen (Figure 3.5).

| | Solvent | Solvent | Gas dyn | Gas dyn | Gas static | Gas static |
|---|---|---|---|---|---|---|
| | **B** | **A** | RKS | UKS-M1 | RKS chain | RKS square |
| Pair | $\bar{l}$ (SD) | $\bar{l}$ (SD) | $\bar{l}$ (SD) | $\bar{l}$ (SD) | $\bar{l}$ (SD) | $\bar{l}$ (SD) |
| Br1-Te3 | - | 290.4 (13.2) | 261.1 (7.9) | 261.3 (7.0) | 258.6 | 270.1 |
| Br2-Te4 | - | 286.2 (13.2) | 261.1 (7.9) | 261.2 (6.7) | 258.5 | 400.0 |
| Te1-Te3 | 274.7 (7.5) | 276.2 (7.4) | 268.8 (6.3) | 267.6 (5.9) | 268.3 | 270.2 |
| Te1-Te2 | 289.3 (13.6) | 285.1 (9.9) | 290.5 (12.2) | 292.6 (11.0) | 284.4 | 299.2 |
| Te2-Te4 | 274.5 (10.0) | 278.2 (7.5) | 268.8 (6.5) | 267.7 (6.7) | 268.3 | 270.2 |
| Te2-Te3 | 396.8 (13.9) | 455.5 (20.0) | 439.0 (23.2) | 439.6 (18.0) | 439.9 | 411.1 |
| Te1-Te4 | 394.5 (13.7) | 441.7 (18.9) | 439.3 (22.8) | 439.6 (17.4) | 439.8 | 395.0 |
| Te3-Te4 | 282.3 (11.2) | 605.6 (19.6) | 555.4 (82.1) | 490.3 (82.6) | 511.6 | 299.2 |

unfavorable charge distribution.

While the intramolecular (Br1-Te3, Br2-Te4, Te1-Te3, Te1-Te2, and Te2-Te4) distances represent the strength of the particular bond, the Te2-Te3, Te1-Te4 and Te3-Te4 distances are a measure of the molecule's geometry. Due to the molecule's symmetry, there are three pairs of inter-atomic distances, which lie in the same distance range and also yield a similar SD value, i.e., the pairs Br1-Te3 and Te4-Br2, Te3-Te1 and Te2-Te4 as well as Te1-Te4 and Te2-Te3. These are grouped in different blocks in Table 3.1. In the case of the molecule within $[C_2C_1Im][Cl]\cdot 1.3AlCl_3$, this is also true for the pairs Te1-Te2 and Te3-Te4. Please note that for the static calculation of the square, the Br-Te distances differ due to the arrangement of the bromide atoms. In the case of system **B**, since the Br2 atom is eliminated from the molecule and the Br1 atom switches between Te1 and Te3 in order to stabilize the charge of the Te square, the Br-Te distances are not considered here.

From a first examination, it can be pointed out that the two Br-Te distances and the Te1-Te2 distance are shorter in the case of the static calculation of the chain in the vacuum

as compared to dynamical gas-phase simulations. This can be traced back to temperature effects, which occur in the dynamic gas-phase simulations. Due to the higher temperature, the atoms receive a higher amount of energy resulting in stronger vibrations. Therefore, the average bond length increases and the bond gets weakened. In addition to this, all covalent bond distances, except for the Te1-Te2 bond, are longer within the solvents as compared to the gas phase simulations and calculations. On the one hand, the Te1-Te2 bond length is increased in the vacuum due to the charge distribution within $Te_4Br_2$ and on the other hand, the elongation of the other bonds, especially the Br-Te bonds, in the solvents is caused by the IL-effect. This effect was already investigated extensively and can be traced back to the properties of ILs to be an "extremely dissociating" solvent.[229,230] In particular, this means that due to the solvent, there is a natural tendency of the molecule to dissociate and rather assume a charged species form, which is why the bonds are stretched and therefore weakened. Thus, the IL-effect supports the electrophilic attack of the Br2 atom by the Lewis-acidic $AlCl_3$.

Furthermore, we observe that the unrestricted gas phase calculations show similar results to the restricted one. We will come back to this point in the electronic structure section.

In addition to the average bond lengths between the molecule's atoms, we provide the intramolecular RDFs considering all Te-Te distances for the molecule in both solvents **A** and **B** (cf. Figure 3.7).

The progression of the RDFs confirms the previous observations and agrees with the findings for the particular bond length. For the chain-like molecule within **A**, three maxima are visible: The first one at around 280 pm corresponds to the Te atoms that are directly bound to each other, the second one to the pairs, Te2-Te3 and Te1-Te4, and the third one to the pair Te3-Te4. Due to the flexibility of the chain, the maxima are broadened with increasing distances. In contrast to this, the square-like molecule within **B** only produces two maxima: The first one for the neighboring Te atoms and the second one for Te atoms arranged oppositely within the square. Since the ring is distorted marginally (Table 3.1), The second maximum of the green curve is broadened as well.

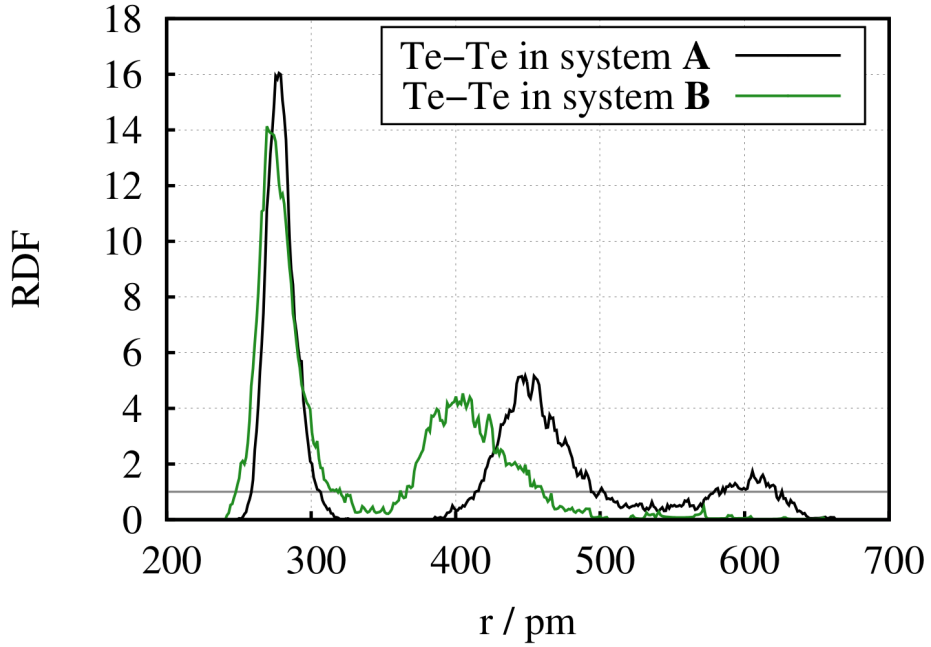


**Figure 3.7** Intramolecular RDFs for all possible Te-Te distances within the observed molecule in both system **A** (black) and system **B** (green).

### Particle solvation and stabilization

Since the characteristic interactions within the solvents and the molecules' reaction mechanism and structure have been examined extensively, we now turn to the solvation and stabilization of the particular structures in both system **A** and system **B**. Therefore, we present the RDFs for different intermolecular distances between Br and Te respectively, and the components of their surrounding solvents (cf. Figure 3.8).

In the case of the Br solvation, it is not surprising that within $[C_2C_1Im][Cl]{\cdot}1.3AlCl_3$, the RDF for the Br-Al distances shows a high signal at around 240 pm, which is due to the covalent bond that is formed between Br2 and Al55, after 2.1 ps of the simulation (Figure 3.5 and Figure 3.6). However, the presence of the $AlCl_3$ in system **B** also influences the molecules' solvation significantly. In comparison to system **A**, the Cl atoms are closer to the bromide due to the Br-Al bond and the peak for the terminal carbon atoms of the cations decreases and shifts to larger distances. Putting this result in the context of the higher microheterogeneity in system **A** compared to **B**, it indicates that although the molecule perceives an IL-effect in both systems, the larger microheterogeneity might

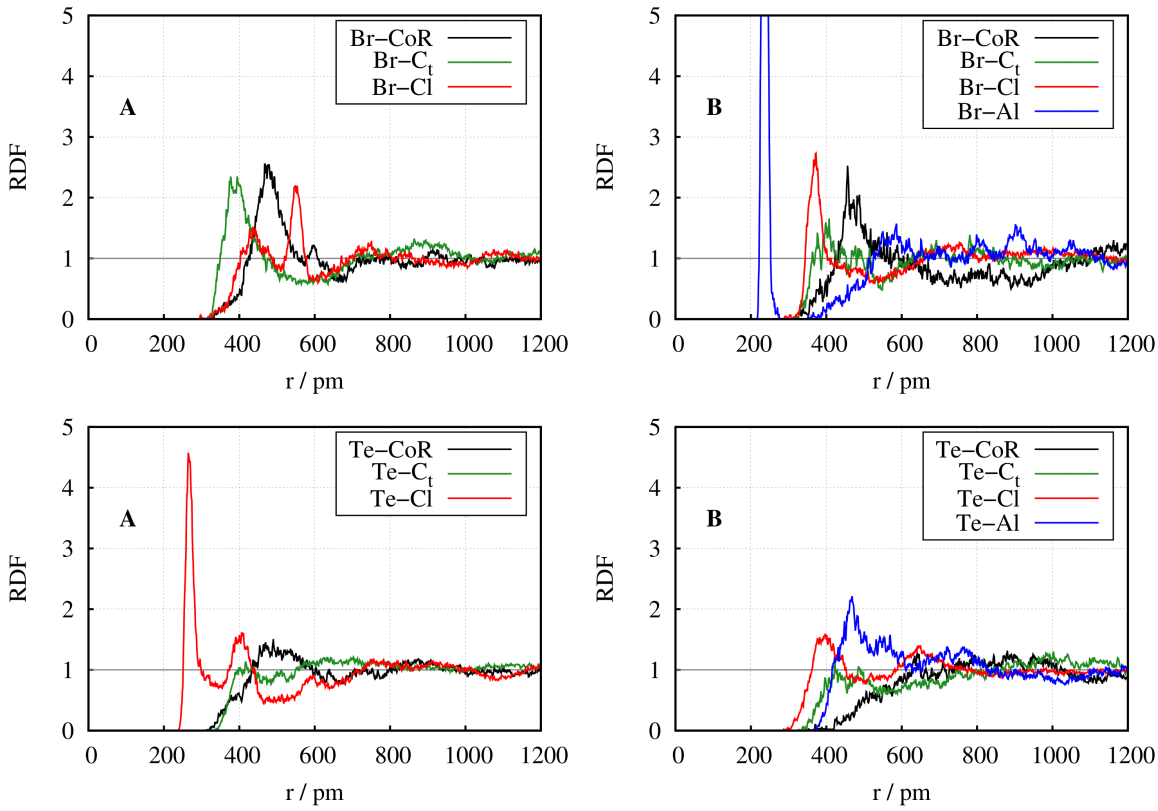


**Figure 3.8** Intermolecular RDFs depending on the distances between Br (upper panels) or Te (lower panels), respectively, and all relevant solvent compounds. The curves for the CoR are depicted in black, for $C_t$ in green, for Cl in red and for Al (for system **B**), shown in the right panels, in blue.

support the more covalent character of the molecule in system **A** by including the bromide atoms in the non-polar structure. The Br-CoR maxima occur at approximately the same distance and show a similar height, which is due to the electrostatic attraction between oppositely charged species.

The effect of $AlCl_3$ can be observed as well by regarding the Te-based RDFs. Within $[C_2C_1Im][Cl]$, the first two maxima arise from the free $Cl^-$ anions, which strongly solvate the Te atoms of the molecule. The first peak at approximately 260 pm indicates the formation of a covalent bond within at least one Te-Cl-pair. However, this event seems to be quite rare because the g(r) value would otherwise be much higher. The majority of the solvating chloride ions are located within a radius of approximately 400 pm around the Te atoms. Moreover, it can be seen that within solvent **B**, the solvation by CoR is reduced compared to the system without $AlCl_3$. This might be due to the fact that in

contrast to system **A**, within system **B**, the Te atoms are solvated by much larger anions and secondly, due to the more ionic character of the Te-molecule, the cations are much less attracted to it. The occurrence of $C_t$ atoms in the close neighborhood of Te atoms is in both cases comparably low while in system **A**, the Br atoms are highly solvated by $C_t$ atoms. This indicates that in system **A**, only the bromide atoms are solvated by and thus penetrate the non-polar parts.

### 3.3.3 Electronic structure

#### Electronic structure in the isolated molecule picture

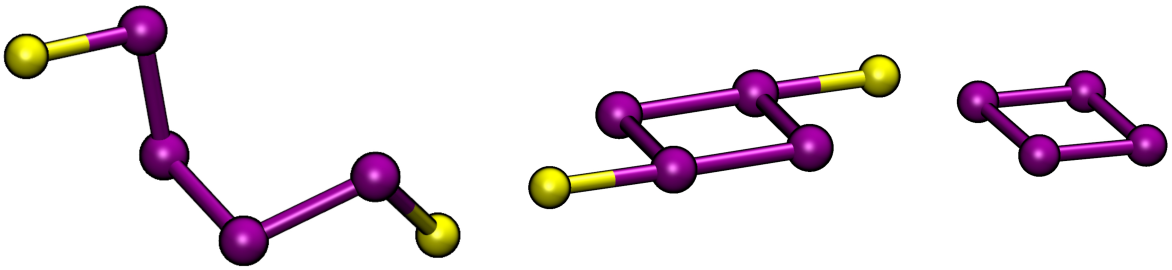

**Figure 3.9** Ball-and-stick representation of the chain-like structure, the square-like structure and the $[Te_4]^{2+}$ cyclic structure. The chain (left) is more stable by 70.2 kJ/mol in the gas phase than the square (middle).

In order to gain insight into the electronic structure of the $Te_4Br_2$ clusters, we optimized a chain-like and a square-like conformation in the gas phase with a pure Gaussian basis set. In addition, we optimized a square $[Te_4]^{2+}$ cluster. The chain shows the lowest energy for the restricted calculation although the unrestricted singlet is off by only $0.7\times10^{-5}$ kJ/mol. However, the unrestricted triplet is much higher in energy; about 189.6 kJ/mol. For the square, the lowest energy structure was obtained for the unrestricted singlet calculations from which the restricted calculation deviated by $0.2\times10^{-3}$ kJ/mol only. However, the triplet state of the square lies 51.4 kJ/mol above the singlet state. The chain (left structure in Figure 3.9) is more stable, in the gas phase, than the square (middle structure in Figure 3.9), by 70.2 kJ/mol.

In Table 3.2, the same distances are given as in Table 3.1. These static quantum chemical values agree well with each other given the difference in the basis set; see computational details. As was observed before, the bromide-tellurium distances are longer in

**Table 3.2** Geometry of different $Te_4Br_2$ clusters calculated at PBE0/SV(P) level of theory. Note, that Br2 is bond to Te2 in the square cluster. Distances between two atoms in pm, angles (3 atoms) and dihedral angles (4 atoms) in degrees.

| Bond | chain | square | square$^\star$ |
|---|---|---|---|
| Br1-Te3 | 253.6 | 266.0 | – |
| Br2-Te4 | 253.6 | 381.6 | – |
| Te1-Te3 | 268.8 | 267.0 | 272.6 |
| Te1-Te2 | 278.6 | 298.1 | 272.6 |
| Te2-Te4 | 268.9 | 267.0 | 272.6 |
| Te2-Te3 | 428.6 | 413.3 | 385.3 |
| Te1-Te4 | 428.1 | 386.7 | 385.6 |
| Te3-Te4 | 506.6 | 298.1 | 272.6 |
| Br1-Te3-Te1 | 103.5 | 91.4 | – |
| Br2-Te4-Te2 | 103.4 | 44.2 | – |
| Br1-Te1-Te2-Br2 | −147.6 | −3.2 | – |
| Te3-Te1-Te2 | 103.0 | 93.8 | 90.0 |
| Te1-Te2-Te4 | 102.9 | 86.2 | 90.0 |
| Te3-Te1-Te2-Te4 | −73.0 | −0.1 | 0.0 |

the square than in the chain. Comparing the values of the $[Te_4]^{2+}$ cluster with the crystal structure[204,205,207] we observe deviations of less than 2 %, see introduction.

## Orbital analysis

Obviously, the different structures possess different symmetry. While the $Te_4Br_2$ chain possesses $C_2$ symmetry, the square shows $C_{2h}$, and the $[Te_4]^{2+}$ cation has $D_{4h}$ symmetry, also see Figure 3.9.

Analyzing the electronic structure of the $[Te_4]^{2+}$ square (with 22 electrons), it is clearly visible that the six electrons in the $\pi$ system give the molecule a certain aromatic character, which corresponds to the assumed more delocalized charge in the square compared to the open form, as discussed in the previous section. The corresponding molecular orbitals are shown on the left in Figure 3.10. Since the molecular geometry on the left forms a perfect square (other than in the bulk simulation), we find two sets of degenerate molecular orbitals in the $\pi$ system which are identical in energy and the orbital *3b* which allow a

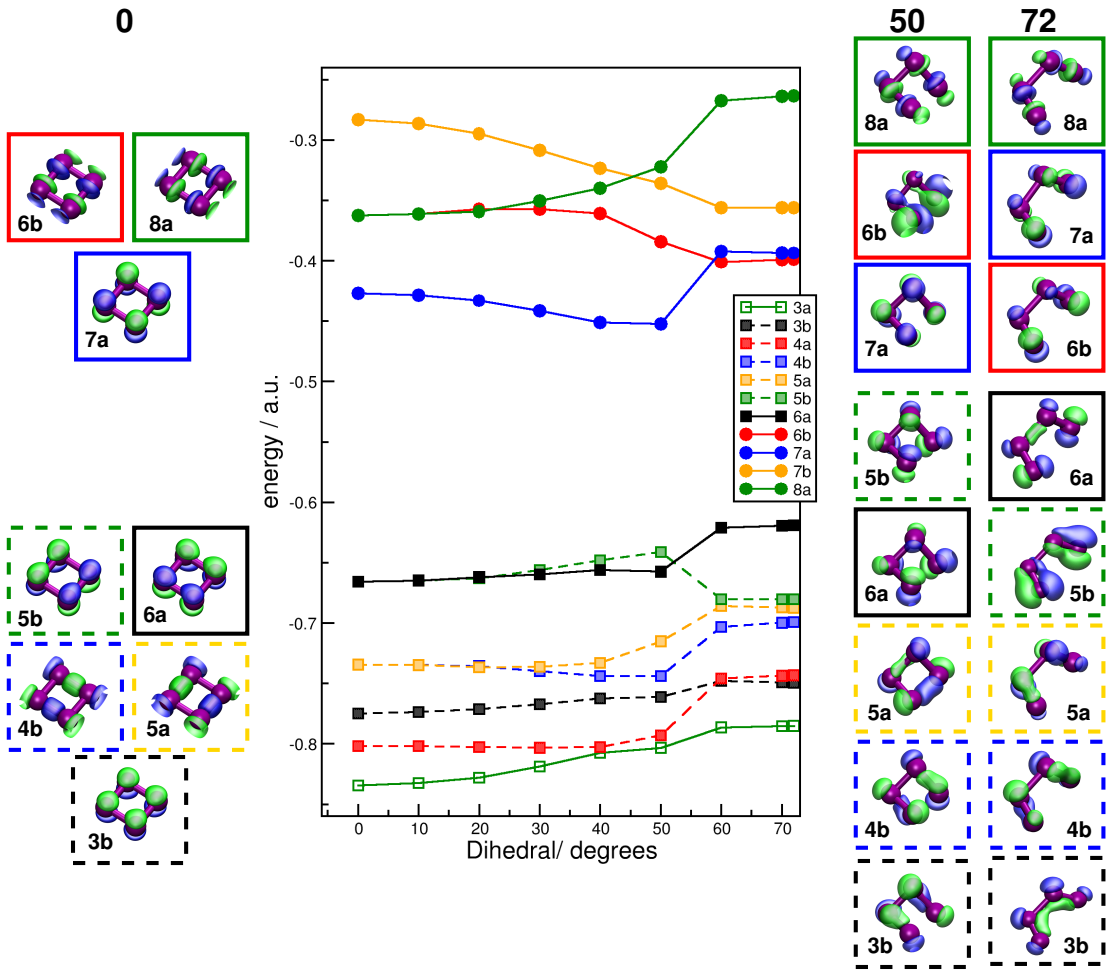


**Figure 3.10** Walsh diagram for the dihedral angle, governing the conversion of the square structure (0 degrees) to a chain-like conformation (72 degrees), plotted on the x-axis and the orbital energy on the y-axis for the different $C_2$-orbitals given in the legend. Representative orbitals are plotted adjacent to the graph. On the left, the $C_2$ orbitals from the 0 degree structure is shown and on the right, the orbitals of the 50 and 72 degree structures are shown. Blue: positive; Green: negative. The isosurface value is chosen to 0.055 except for 50-6*b* and 72-5*b* where an isosurface value of 0.03 was chosen in order to show the transformation to the lower degree structures.

perfect delocalization of the electrons.

In Figure 3.10, we also show the Walsh diagram along with the orbitals.[231] The dihedral angle is plotted on the x-axis and the orbital energy on the y-axis for the different $C_2$-orbitals given in the legend. Please note that the square structure possesses a dihedral angle of 0° and the chain-like conformation, of 72°. At 0°, the LUMO is orbital *7a* and the HOMO and HOMO-1 are degenerate with the orbitals *6a* and *5b*. For the 72°-structure, it

changes to the HOMO being the *6a* and the LUMO being the *6b* orbital. The degeneracy is now lifted, but the increase in orbital energy of *6a* is compensated by a decrease in orbital *5b*.

It is obvious, that *5b* crosses the *6a*, which is a symmetrically allowed crossing. Thus, the energy barrier is expected to be low which nicely corresponds to the reaction occurring in the simulations. For the 0° structure, also the HOMO-2 (*5a*) and HOMO-3 (*4b*) are degenerate, while for the chain-like structure, the HOMO-1, the HOMO-2, and HOMO-3 are very close in energy as are the LUMO and LUMO+1. All these orbitals become more negative in energy indicating a driving force for the reaction.

## 3.4 Conclusion

We carried out a theoretical study of a $Te_4Br_2$ molecule dissolved in two different ionic liquids, namely 1-ethyl-3-methylimidazolium chloride (system **A**) and 1-ethyl-3-methylimidazolium chloride mixed with aluminum chloride $[C_2C_1Im][Cl]\cdot 1.3AlCl_3$ (system **B**).

For the solvent structures, we expect almost no microheterogeneity, i.e., the separation of polar and non-polar groups, because the ethyl chain merely allows for dispersed islands of the non-polar groups within a connected network of polar subunits.[9] Nevertheless, we see an increased microheterogeneity for system **A** because this system contains the smaller anions as compared to system **B**. This influence of the anion size on the nanostructure of the liquid was observed by us previously.[12] Connected to this is the fact that the $AlCl_3$ forms different anionic species[227] in system **B** which exceed the size of simple chloride anions by far. We find apart from a few "free" chloride atoms, 89.4% $Al_1$ ($AlCl_3$ and $AlCl_4^-$) clusters, 8.5% $Al_2$ ($Al_2Cl_7^-$) and only 2.1% $Al_3$ ($Al_3Cl_{10}^-$) clusters.

Turning to the $Te_4Br_2$ molecule dissolved in the different liquids, we observe Te-Br-bond elongations compared to gas-phase simulations and can thus infer that an ionic liquid effect is at play and a tendency to form more ionic species is obvious[63]. However, an even more striking observation is that for system **B**, a rearrangement of the $Te_4Br_2$ molecule occurs due to a bromide abstraction by a former anionic Al-species which changes

into a $AlCl_3$ species before the abstraction. After this abstraction, the $Te_4Br_2$ molecule assumes a square-like form and is thus converted from an open form to a closed, more charged species. The second Br remains at the $[Te_4]^{2+}$ but jumps between two Te atoms. These findings support the proposed reaction mechanism for the formation of tellurium polycations in Lewis-acidic media by halide abstraction with subsequent redox reaction or rearrangement.[201,202,204,205,232]

This rearrangement reaction also has consequences on the solvation between the remaining $Te_4Br^+$ ion and the liquid. The separated $Br^-$ species being strongly bound within an $AlCl_3Br^-$ anion, the Br atom now perceives the presence of the neighboring Cl atoms. Due to the increased microheterogeneity in system **A**, the Br atoms are much more solvated by the terminal carbon atoms in this liquid than in system **B**. This leads to the possibility of a structure-directing effect, caused by the non-polar groups, which has to be investigated in more detail with various different side chains.

Considering the electronic structure in the isolated Te-molecule, we find good agreement between the experimental crystal structure values[204,205,207] and the calculations. The unrestricted singlet and the restricted calculations show almost identical energy while the unrestricted triplet lies much higher in energy. The Walsh diagram indicates that the reaction is symmetry-allowed and thus shows a small barrier which is why we observe this reaction in the time-scale of our simulation.

To summarize, our theoretical study allowed to characterize the influence of the Lewis-acidic $AlCl_3$ on the formation of the $Te_2Br$ species in an ionic liquid and to reveal the mechanism of this chemical reaction on the molecular level.

In order to extend this study, it is planned to execute further simulations using the $[C_4C_1Im][Cl]$ IL as solvent for tellurium bromide particles or clusters of different sizes with the aim of approaching the real crystallization behavior of the particles. The findings of this study will contribute to a better comparability to and deeper understanding of the experimental synthesis of $Te_2Br$ provided by Groh et al.[200]

## Acknowledgements

The authors would like to thank Prof. em. Dr. Dr. h.c. Sigrid D. Peyerimhoff and Dr. Werner Reckien for the helpful discussions and their scientific input. Moreover, we would like to thank the support from the Deutsche Forschungsgemeinschaft under the SPP 1708. RE is a member of the International Max Planck Research School for Reactive Structure Analysis for Chemical Reactions. Therefore, the authors thank the International Max Planck Research School for supporting RE. MFG thanks the graduate academy of the TU Dresden for support, financed by the excellence initiative of the German federal and state governments.

# 4 Template effects in ionic liquids

The application of ionic liquids as reaction media has led to very successful outcomes in the material synthesis of many different products, with the advantage that in most cases only mild reaction conditions and short synthesis times are required. Thereby, the solvation effects of the IL, arising from the various interactions emanating from the ion's building blocks, are rather complex, as can be seen from the study above. One interesting aspect in that regard is the role of the cation, possessing an ethyl side chain attached to the charge-carrying imidazolium ring. Even if this ethyl side chain is rather short, the system containing the smaller chloride anions already shows a tendency towards microheterogeneity, i.e., the segregation of the polar and non-polar groups.

The microheterogeneity in ionic liquids has been investigated intensively, especially by theoretical methods (cf. subsection 1.2).[7–15] Resulting from this, it is common sense that increasing the length of the side chain to at least a butyl group or longer alkyl units leads to the formation of continuous non-polar microphases, embedded in the otherwise polar IL network. The coexistence of these two microphases, and the respective individual interactions within them, results in a high degree of structural self-organization in such ILs.[18,19] This consequently opens the perspective for considering ionic liquid as structure-directing agents or templates,[26] which significantly enhances the potential of these solvents for material synthesis, but also for other applications. Simultaneously, it opens a completely new research area with challenging tasks, because a potential template effect adds to the already complex working principles of ILs and requires an even better understanding of the molecular level interactions in them. Thus, appropriate methods have to be employed that are capable of capturing such structural effects.

In this context molecular dynamics simulations represent the method of choice. The advantage here is that, with this technique, systems containing tens of thousands of atoms and more can be simulated over time scales in the nanosecond range with feasible com-

putational effort. Thus, MD simulations are an ideal tool to give insight into microscopic many-body structural effects and to observe their evolution over time. Such effects can be for example the formation of solvation structures with several shells or the formation of larger microphases. Next to the simulation technique, the choice of analysis functions to elucidate the occurrence and temporal development of such complex structural motives, both qualitatively and quantitatively, plays a key role as well. For this purpose, the trajectory analyzer and visualizer tool TRAVIS is employed,[86,87] which contains a multitude of different functions, like distribution functions and the domain analysis tool (cf. subsection 2.3), which in combination provide a comprehensive molecular level picture of the simulated system.

When aiming at investigating and understanding non-trivial structural processes in liquids, it is necessary to conduct systematic investigations of appropriate model systems in order to break down the complexity, allowing for focusing on the influence of only one parameter at a time. With respect to the degree of microheterogeneity in ILs and its potential to function as template, this parameter is the length of alkyl side chains present in the system. For this purpose the following study focuses on imidazolium based ILs 1-alkyl-3-methylimidazolium bis(trifluoromethylsulfonyl)imide considering ethyl, butyl, hexyl and octyl side chains attached to the cation ($[C_xC_1Im][NTf_2]$, x = 2, 4, 6, 8). As solute molecules either *n*-dodecanol or *n*-butanol, in a ratio of 5:1 ion pairs of the IL to alcohol molecules, are mixed into the four different ILs. IL-alcohol mixtures have already been studied extensively, both theoretically and experimentally.[233–236] While the investigation of IL-methanol mixtures has shown that the methanol molecules mainly interact with the polar units of the IL via hydrogen bonding, and tend to form larger clusters at higher methanol concentrations,[233,234] hydrocarbons like *n*-hexane mainly interact with the alkyl groups of the IL.[233] Accordingly, depending on the length of the IL cation's and alcohol molecule's side chains, aliphatic alcohols can be expected to interact stronger with either the polar, the non-polar, or both microphases in a microheterogeneous IL, making them promising candidates for the investigation of the capability of ILs to act as structure-directing agents.

# A molecular level understanding of template effects in ionic liquids

Roman Elfgen*†, Oldamur Hollóczki* and Barbara Kirchner*

*First published: 13 November 2017*

*DOI: 10.1021/acs.accounts.7b00436*

Reprinted with permission from:

R. Elfgen, O. Hollóczki and B. Kirchner, *A Molecular Level Understanding of Template Effects in Ionic Liquids*, Acc. Chem. Res. (2017), 50, 2949–2957.



*Mulliken Center for Theoretical Chemistry, Institut für Physikalische und Theoretische Chemie, Rheinische Friedrich-Wilhelms-Universität Bonn, Beringstraße 4+6, 53115 Bonn, Germany

†Max Planck Institute for Chemical Energy Conversion, Stiftstr. 34-36, D-45413 Mülheim an der Ruhr, Germany

**Contributions to the manuscript**

- Running the molecular dynamics simulations
- Analysis of the trajectories
- Discussion of the results
- Writing the manuscript

**Conspectus.** The structure-directing or template effect, has been invoked several times for ionic liquids to explain the different outcome in material synthesis, namely, different scaffolds or geometrical arrangements with varying ionic liquids. It is obvious to assume that such an effect can originate from the most likely complex microstructure, being present within the ionic liquid itself. In that regard, ionic liquids have already been shown to undergo a nanosegregation into polar and non-polar phases, which is commonly known and denoted as microheterogeneity. In order to provide detailed insight on the molecular level and to understand the effects rising from this structuring, we performed molecular dynamics simulations on selected very simple model systems composed of 1-alkyl-3-methylimidazolium bis(trifluoromethylsulfonyl)imide, considering ethyl, butyl, hexyl and octyl side chains attached to the cations, mixed with either $n$-dodecanol or $n$-butanol. By analyzing snapshots of the simulation boxes and calculating spatial distribution functions we can visualize that with increasing side chains, the systems show considerable nanosegregation into polar and non-polar domains. Combined angular and distance distribution functions show that in case of the nanosegregating systems the side chains of the cations are preferentially arranged in a parallel fashion, which indicates a micelle-like structure for the ionic liquids. The alcohol molecules participate in, and are, therefore, influenced by this microheterogeneity. It can be shown that in the case of the short IL alkyl side chains, the self-aggregation of the non-polar units of the alcohols is much stronger, while for the long chain cations the non-polar entities of the alcohols are most often connected to the non-polar units of the ionic liquids. Using our domain analysis tool, we can quantify these observations by tracking the number, size, and shape of the polar and non-polar entities present in the different investigated systems. The aforementioned combined angular-distance distribution functions reveal a structure-directing effect of the ionic liquids on the alcohol molecules within our simple model systems. The ionic liquids act as template and order the alcohol molecules according to their own structure, resulting in a parallel alignment of the alkyl side chains of the alcohols and ionic liquid cations, with both polar groups being at the same side. These observations show that the microheterogeneous structure of ionic liquids can indeed be applied to order substrates with respect to each other or, for example, to catalysts in a predetermined fashion, opening new possibilities

for explaining or enhancing selectivites of chemical reactions in ionic liquids.

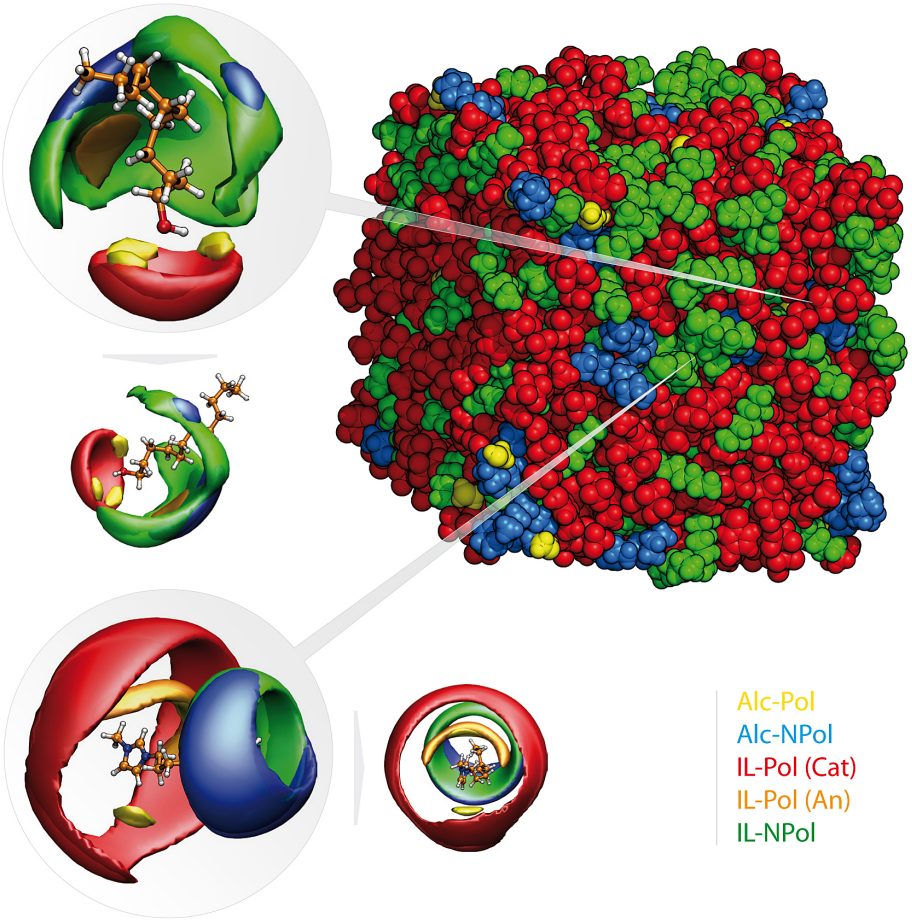


**Figure 4.1** Table of contents picture for template effect in ionic liquids study.

## 4.1 Introduction

As opposed to traditional molten salts,[13,26,237,238] ionic liquids (ILs)[13,191,237,239–241] possess polar and non-polar moieties, which in many cases results in a distinct structural ordering. Resulting from this polar–non-polar nature (one has to be careful here not to associate electrostatic forces with the polar part and dispersive forces with the non-polar part; both parts have electrostatic and dispersive portions just differently weighted[238]), and the underlying balance between weak and Coulombic interactions, many ILs form nano-segregated structures, i.e., microheterogeneity (MH).[7,8,11–15,242] Hence, the term

"supramolecular fluids" has been coined by Dupont to describe supraionic aggregates observed in ILs.[26] These features of ILs point to a different view than simply considering them as solvents; namely, it highlights their ability to act as structure-directing agents or templates.[27] Such effects have been discussed extensively for standard supramolecular systems.[28]

Traditionally, the template effect is described as the template organizing other components of a system and allowing for product formation that would not form as easily or at all in the absence of the template.[30] This is accompanied by chemical reactions, in which significant spatial, topological or geometric control is achieved, where the structural information stored in the template is transferred to the product. It has been pointed out repeatedly that a template works as an "entropic sink", due to the introduction of the aforementioned increased ordering within the given system.[243] One prominent example is the template-assisted synthesis of rotaxanes.[29] Vögtle and coworkers[29] have discussed the mechanism of threading a macrocycle-wheel onto an axle to proceed via a pseudo- or semirotaxane complex, in which the guest is fixed by hydrogen bonds inside the host cavity. The preorganization of the axle enables a further reaction of the reactive groups at the end of the axle to form stoppers and thus a full rotaxane molecule.

Template or structure-directing effects in ILs[27] have been suggested especially in the field of inorganic material synthesis.[27,31–33] It was reported that the IL ions incorporate into the forming solid state product during the synthesis, and therefore through directing the structure new materials can be obtained.[33] Evidence for this phenomenon was found during the synthesis of three-dimensional iodometallate networks like $GeI_4$-$I^-$ and $[Bu_3MeN]_3[cis\text{-}Bi_3I_{12}]$, using ILs with asymmetrically substituted and sterically demanding cations.[34,35] ILs recently have found increasing use as reaction media in the synthesis of zeolite-analogous framework compounds and metal-organic frameworks. In contrast to their conventional synthesis, which was performed under hydro- and solvothermal conditions via suitable templates, Morris et al. proposed a so called "ionothermal synthesis" in ILs.[31,32] For this method, IL solvents with large organic cations are used, which can directly act as template to guide the synthesis pathway. Liquid clathrate formation, occurring upon mixing ILs with aromatic hydrocarbons, presents another example where

template effects might play a role.[36–38] Liquid clathrates are generally considered to be liquid yet localized host-guest complexes formed by associative interactions between salt ions and aromatic molecules.

The first step towards understanding such complicated effects lies in understanding the nature of the IL itself. As mentioned already, microheterogeneity can be considered as a self-organization of the IL and thus could be highly relevant for the IL playing a role as a template. Several studies have contributed to the understanding of MH,[7,8,11–15,242] MH shows a distinct dependence on the length of the side chains at the IL ions, typically attached to the cation. Although the side chains tend to aggregate already at the shortest applied ethyl groups,[15,242] these aggregates are generally very small. It was observed by theory[7,8,242] and later by experiments[11] that increasing the length of the side chain on the cation to longer than a butyl group results in the formation of a continuous non-polar microphase that stretches through the whole system. Interestingly, an influence of the anion has also been observed on the aggregation of the cationic side chains.[12,15] Naturally, functionalizing the side chains influences the MH. For instance, side chain perfluorination increases the segregation behavior compared to their parent alkyl side analogues.[12,14,15] Considering the tendency of fluorous groups to segregate into a separate domain from both polar groups and hydrocarbons, fluorination opens the possibility to build even three microphases. By attaching long perfluorinated side chains to the anions, while having cations with large alkyl groups, Triolo and coworkers,[16] and later Rebelo and coworkers created such "triphylic" ionic liquids.[17] In a combined theoretical and experimental study, we have shown that the triphilicity can even be tuned by mixing ILs with alkyl and perfluoroalkyl side chains at the cations with different molar fractions.[14]

All the information above points to the existence of supramolecular structures in ionic liquids, which may be tuned through changing the components of the liquid. Since such features generally infer the possibility of template effects, and as described above there are indeed some scattered information on such phenomena in ILs, we will aim here to investigate this issue in detail theoretically. For such purposes, theoretical methods are ideal tools, since they allow direct insight into the microscopic level picture,[13] providing, therefore, an in depth understanding of the governing structural features. We investigate

the possibility of template effects of ILs on solute alcohol molecules, thus at very simple model systems.

Alcohol-IL mixtures have been studied in detail already.[233–236] In various methanol-IL mixtures both theoretical[233,234] and experimental[234,235] results show that this small alcohol molecule interacts mainly with the polar part of the IL, in particular through hydrogen bonds with the anions. At higher methanol concentrations and in case of the weak hydrogen bond acceptor bis(trifluoromethylsulfonyl)imide ILs, the alcohol molecules tend to form larger clusters in the liquid through the strong methanol-methanol hydrogen bonds.[234] On the other hand, hydrocarbons, such as *n*-hexane, tend to interact mainly with the alkyl groups of the IL.[233] Accordingly, aliphatic alcohols can be expected to interact mainly with the polar, the non-polar, or both microphases in a microheterogeneous IL, depending on the length of the side chains of the alcohol and the IL. Recent calorimetric experiments indirectly support this idea.[236]

Therefore, in this work, we apply molecular dynamics simulations on model systems composed of the imidazolium based ILs 1-alkyl-3-methylimidazolium bis(trifluoromethylsulfonyl)imide considering ethyl, butyl, hexyl and octyl side chains attached to the cation ($[C_xC_1Im][NTf_2]$, x = 2, 4, 6, 8) mixed with either *n*-dodecanol or *n*-butanol in a ratio of 5:1 ion pairs of the IL to alcohol molecules (cf. Table 7.1 in the appendix for more details).

## 4.2 Analyzing molecular dynamics simulations

Molecular dynamics simulations generate a large data file, that is, the trajectory, which contains for each of the discretized time steps the configuration with atomic positions and velocities of the simulated system.[244] This amount of data needs to be processed during the analysis, and turned into chemically meaningful data, where the orientation of the molecules, as well as their movements can be shown. Our open source software TRAVIS[86] makes it possible to extract data beyond the regular analysis, and the supramolecular structure of the liquid can also be quantified. Below a few details are given regarding this function; more information on the analyses can be found in ref. [86]. The full simulation

details of the present work are given in the supporting information (subsection 7.2.2).

The dissection of the liquid into domains is initiated by defining their building blocks, that is, subsets.[15] These subsets can be functional groups or parts of the molecules or complete molecular entities. Then a radical Voronoi tessellation is performed, where all atoms are considered as Voronoi sites (i.e., points around which the Voronoi polyhedra are constructed). In this approach, the van der Waals radii are used to define borders, and thus volumes and surfaces for each atom, creating the atomic Voronoi cells, which will sum up to the cells of each subset. Those kind of subsets, which we initially defined to be building blocks of the same chemical nature (e.g., alkyl groups), belong to the same domain (e.g., non-polar domain) if their cells share a common face. This allows us to obtain the average number of each kind of domain present in the liquid, which we call in this paper domain count $N_{Dom}$. Any value for $N_{Dom}$ that is smaller than the total number of the particular subsets that constitute it represent a certain aggregation in the system. If this domain count is one, it means that the subsets are forming a large, continuous microphase that stretches through the liquid. Since the Voronoi tessellation defines surfaces for the subsets, one can also calculate how much of the surface of each subset is covered by any of the subsets in the system. It is worth mentioning here that we applied successfully the radical Voronoi tessellation beside the domain analysis, also in calculating partial atomic charges in systems with significant charge transfer[63] and with respect to the calculation of vibrational spectra,[83,172,173] that is, for the discussion of the microscopic structure in systems with a strong dynamic network of intermolecular interactions, such as ILs.

## 4.3 Observing the template effect in ionic liquids

The visual inspection of the simulated systems already shows some highly important information regarding the microheterogeneity (MH) and the template effect. Figure 4.2 shows a snapshot of each simulated system. First we focused on the MH in total, regardless of whether the alkyl side chains or the polar groups are from the alcohol or from the IL (see top right of Figure 4.2). It is clearly visible that in case of the long side chains the

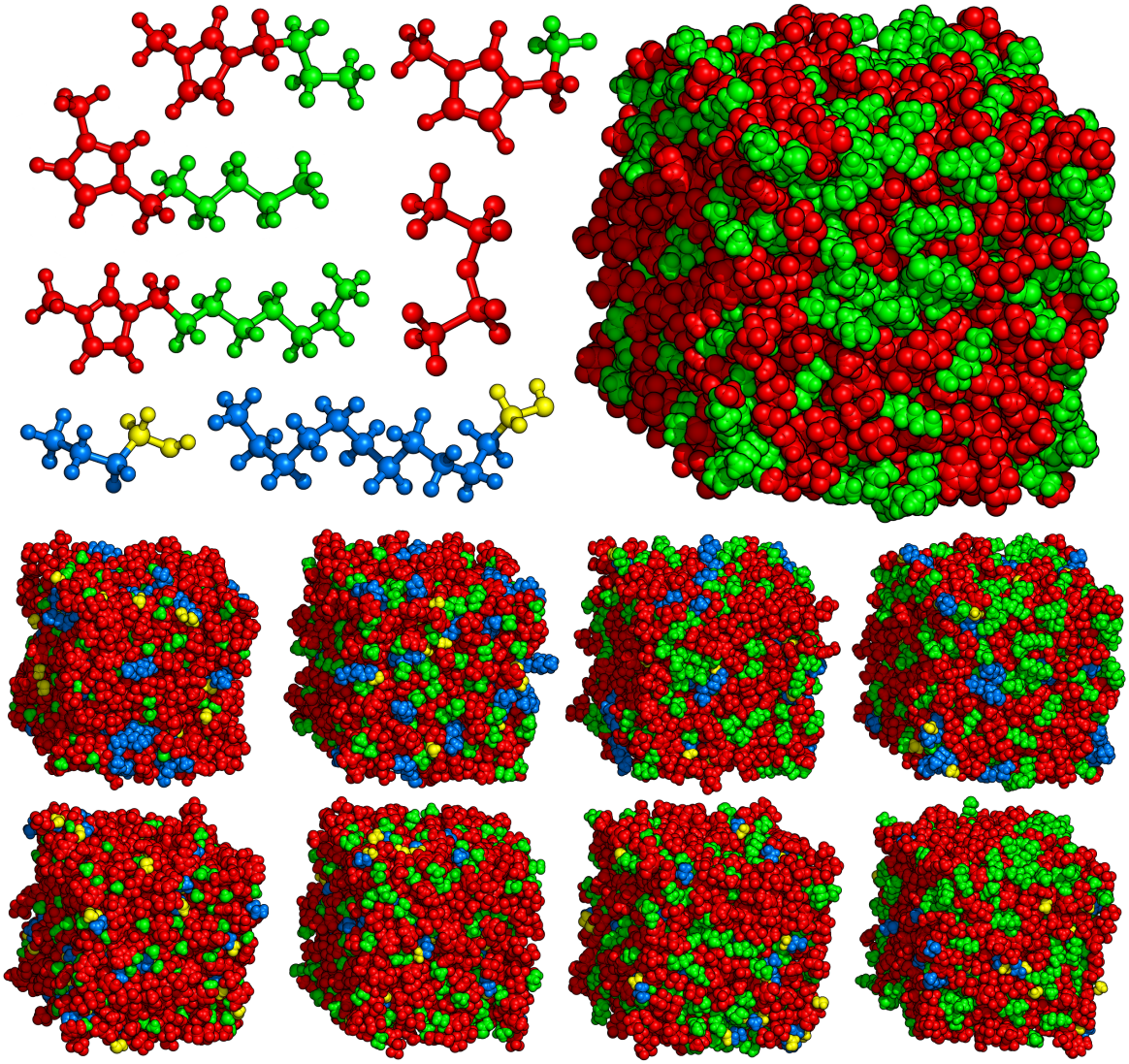

**Figure 4.2** Snapshots of the simulated systems illustrating possible microheterogeneities. In the upper right snapshot we distinguish only between polar (red) and non-polar (green) subsets at the *n*-dodecanol in $[C_8C_1Im][NTf_2]$ system. For the eight snapshots below red indicates polar units of the ILs (P-IL), green indicates non-polar units of the ILs (N-IL), yellow indicates polar units of the alcohols (P-A), and blue indicates non-polar units of the alcohols (N-A). The upper four snapshots represent the systems composed of *n*-dodecanol in $[C_xC_1Im][NTf_2]$ with x = 2 (left) to x = 8 (right) and the lower ones represent the *n*-butanol containing analogues.

polar (red) and non-polar groups (green) are segregated in the liquid, forming a highly microheterogeneous structure. The template effect of the IL should lie in the arrangement of the alcohol molecules within this mesoscopic structure. Distinguishing the side chains of the alcohol molecules and the IL cations, as well as the polar moieties of the alcohol

and the IL, shows interesting trends.

It is apparent that the polar units of the alcohol (yellow) are always connected to the polar components of the ILs (at least half a solvent shell is formed), showing in agreement with the previous studies[233–236] the strong interactions between the polar components through hydrogen bonding; see also the spatial distribution functions (SDFs) in Figure 4.3 and the discussion below. For the side chains of the alcohols (blue), it is clearly visible that the self-aggregation is much stronger for *n*-dodecanol than for *n*-butanol, due to the difference in the length of the alkyl groups. Moreover, while the self-aggregation of the alcohols' non-polar units is clearly observable in case of the ILs with shorter side chains (Figure 4.2 left), in case of longer cationic side chains (Figure 4.2 right), these blue units are dispersed, and they interact with the non-polar moieties of the IL rather than with each other. The clustering of alcohols has been observed before for ILs with short side chains,[234] but this was originated from hydrogen bonding in methanol, and here, we observe the aggregation due to the long side chains of the alcohols in short side chain-ILs and the disruption of the alcohol's self-aggregation in long side chain-ILs. This indicates a possible template effect in long alkyl side chain-ILs, in which the alkyl moieties of the alcohols are aligned according to the order within the IL side chains, instead of self-aggregation.

Although the snapshots showed a clear indication that a template effect might be present in the hereby investigated systems, the structure has to be characterized in a systematic and quantitative manner and averaged over the course of the full simulations to prove this phenomenon. We first performed a detailed Voronoi and domain analysis, as described in the previous section.

Table 4.1 lists the number of domains, $N_{\mathrm{Dom}}$, formed by the different subsets. It can be seen for $[C_2C_1Im][NTf_2]$ that, in agreement with the conclusions from the snapshots, the polar subsets (P) form a single domain, which shows that the alcohol molecules are interacting through their hydroxyl group with the polar part of the ionic liquid. The non-polar components (N), on the other hand, show a high number of domains, indicating that the ethyl side chains of the IL cations are not long enough to form larger structural units than small clusters in the liquid. By the increase of the IL's side chain length the

**Table 4.1** Domain analysis for different ILs $[C_xC_1Im][NTf_2]$ mixed together with alcohols $H_{2y+1}C_yOH$. The number of domains $N_{Dom}$ emanating from the different subsets P, N, P-IL, N-IL, P-A and N-A are shown. The maximal $N_{Dom}$ values for each subset are shown in parenthesis underneath the subset names.

| | | $N_{Dom}$ | | | | | |
|---|---|---|---|---|---|---|---|
| IL | ALC | P | N | P-IL | N-IL | P-A | N-A |
| x = | y = | (500) | (300) | (500) | (250) | (50) | (50) |
| 2 | 12 | 1.0 | 50.5 | 1.0 | 136.4 | 40.5 | 7.7 |
| 4 | 12 | 1.0 | 5.5 | 1.0 | 29.0 | 40.9 | 10.0 |
| 6 | 12 | 1.0 | 1.5 | 1.0 | 4.8 | 41.7 | 12.3 |
| 8 | 12 | 1.1 | 1.1 | 1.0 | 1.6 | 41.6 | 13.6 |
| 2 | 4 | 1.0 | 81.4 | 1.0 | 126.4 | 40.2 | 31.9 |
| 4 | 4 | 1.0 | 7.7 | 1.0 | 19.6 | 41.7 | 34.9 |
| 6 | 4 | 1.0 | 1.9 | 1.0 | 2.9 | 41.3 | 34.3 |
| 8 | 4 | 1.0 | 1.2 | 1.0 | 1.3 | 42.4 | 36.3 |

number of non-polar mesoscopic units drops rapidly, showing a progressive growth of the alkyl islands in the liquid. This is in good accordance with the typical behavior of such ILs.[7,8,11–15,242] Interestingly, although the number of polar domains is 1.0 in almost all systems, in case of the *n*-dodecanol in $[C_8C_1Im][NTf_2]$ simulation, it rises to a value of 1.1. This finding can be explained by the — compared to other systems — extensive interaction between the N-A and N-IL subsets, which overcome the attraction of the hydroxyl moiety to the polar units of the IL, occasionally albeit rarely pulling the alcohol molecule out of the vicinity of the polar domain completely, splitting thereby the single polar domain into two entities.

Considering the functional groups of the alcohol molecules separately from those of the IL, an interesting trend can be observed. The domain counts of the P-A subsets, are barely influenced by the increase in the alcohol or IL side chains. The $N_{Dom}$ values are in all cases between 40 and 43. This indicates that the 50 alcohol molecules are embedded in the liquid almost always separately from each other, and hydrogen bonds between them are relatively rare. Interestingly, the N-A subsets show a completely different behavior.

Upon the increase of the side chain length, the *n*-dodecanol aggregates decrease in size significantly, as the domain counts almost double, showing the exact opposite change compared to the IL's N-IL subsets. For *n*-butanol, the changes are not that dramatic, but their dissociation is nevertheless notable. These findings confirm the picture obtained from the snapshots above: The non-polar alcohol subsets (N-A) stick together when the N-IL part is small and they are more dispersed when the ILs get more microheterogenous, that is, more connected in the N-IL part.

**Table 4.2** Surface coverage from Voronoi analysis for different ILs $[C_xC_1Im][NTf_2]$ mixed together with alcohols $H_{2y+1}C_yOH$. It is distinguished between the subsets P-IL, N-IL, P-A and N-A.

| IL | ALC | P-IL coverage | | | | N-IL coverage | | | |
|---|---|---|---|---|---|---|---|---|---|
| x = | y = | P-IL | N-IL | P-A | N-A | P-IL | N-IL | P-A | N-A |
| 2 | 12 | 74.6 | 14.0 | 2.1 | 9.3 | 85.2 | 5.2 | 1.5 | 8.0 |
| 4 | 12 | 67.1 | 22.8 | 1.9 | 8.1 | 75.2 | 14.1 | 1.6 | 9.1 |
| 6 | 12 | 62.8 | 28.1 | 1.8 | 7.3 | 66.8 | 22.3 | 1.5 | 9.5 |
| 8 | 12 | 60.1 | 31.7 | 1.7 | 6.4 | 58.9 | 30.2 | 1.4 | 9.5 |
| 2 | 4 | 78.9 | 14.6 | 2.4 | 4.2 | 89.1 | 5.7 | 1.7 | 3.4 |
| 4 | 4 | 70.1 | 24.0 | 2.2 | 3.7 | 79.3 | 15.2 | 1.8 | 3.7 |
| 6 | 4 | 65.1 | 29.6 | 2.0 | 3.3 | 70.4 | 24.2 | 1.7 | 3.7 |
| 8 | 4 | 61.7 | 33.5 | 1.9 | 3.0 | 62.2 | 32.6 | 1.6 | 3.6 |
| IL | ALC | P-A coverage | | | | N-A coverage | | | |
| X = | y = | P-IL | N-IL | P-A | N-A | P-IL | N-IL | P-A | N-A |
| 2 | 12 | 54.6 | 6.4 | 2.8 | 36.1 | 63.8 | 9.0 | 9.6 | 17.6 |
| 4 | 12 | 49.3 | 12.1 | 2.8 | 35.7 | 55.0 | 18.8 | 9.5 | 16.7 |
| 6 | 12 | 46.6 | 15.9 | 2.6 | 34.9 | 49.3 | 27.0 | 9.3 | 14.4 |
| 8 | 12 | 44.1 | 19.0 | 2.7 | 34.2 | 43.4 | 34.5 | 9.1 | 13.0 |
| 2 | 12 | 60.6 | 7.3 | 2.9 | 29.2 | 67.8 | 9.1 | 18.5 | 4.6 |
| 4 | 12 | 55.4 | 13.5 | 2.4 | 28.6 | 59.7 | 18.3 | 18.1 | 4.3 |
| 6 | 12 | 50.7 | 17.8 | 2.6 | 28.9 | 52.6 | 25.1 | 18.3 | 4.0 |
| 8 | 12 | 47.7 | 21.5 | 2.3 | 28.5 | 47.7 | 30.9 | 18.1 | 3.6 |

Creating the Voronoi cells in the system at each step of the simulation allows not only

the domain analysis but also provides valuable information on the neighborhood of each subset and the interaction surfaces between the corresponding moieties. The average percentages that the different groups cover from the surface of each subset are shown in Table 4.2 (note that each pair of subsets that are covalently bound to each other show, of course, some interaction surface; for example, N-IL possesses a high coverage by P-IL, which partly stems from the covalent bond between them). Apparently, for every subset, the coverage by N-IL increases by the increasing length of the cationic side chain, while the coverage by P-IL decreases. This indicates an increasing microheterogeneity and therefore confirms the conclusions from Table 4.1. Furthermore, in accordance with the results from the domain analysis, the surface coverages corresponding to the alcohol-alcohol interactions, especially between the alcohols' alkyl chains, the coverages show a monotonous decreasing trend upon increasing the length of the cationic side chain; instead, the N-A subsets are covered more by the N-IL units. This further emphasizes that the alcohol molecules are pulled to the N-IL microphases, and the solvation of the alcohol molecules will be switched from the other alcohol molecules to the solvent when changing the structure of the IL.

After having seen how the embedding of the alcohol in the IL changes as the microheterogeneous structure of the solvent is altered, we focused on understanding how the local environment of the solute molecules differs in the present set of ILs. To observe the spatial, three-dimensional distribution of the previously defined subsets around the ions and molecules in the system, we created the spatial distribution functions (SDFs). In Figure 4.3, we illustrate the solvation of the $[C_8C_1Im]^+$ cation (left) and *n*-dodecanol in $[C_8C_1Im][NTf_2]$ (middle), and the *n*-dodecanol in $[C_2C_1Im][NTf_2]$ (right). For more detailed information on the SDFs generation, including isovalue ranges ($I_{min}$ - $I_{max}$) and chosen isovalues $I$ for SDFs isosurfaces, see Table 7.2 and the corresponding description in the appendix.

In accordance with the microsegregation observed above, the SDFs around the cations clearly show the local distinction between the polar (yellow, orange and red) and non-polar (green and blue) subsets: The cationic imidazolium headgroup apparently attracts the polar moieties, while the non-polar subsets are located around the side chain. The

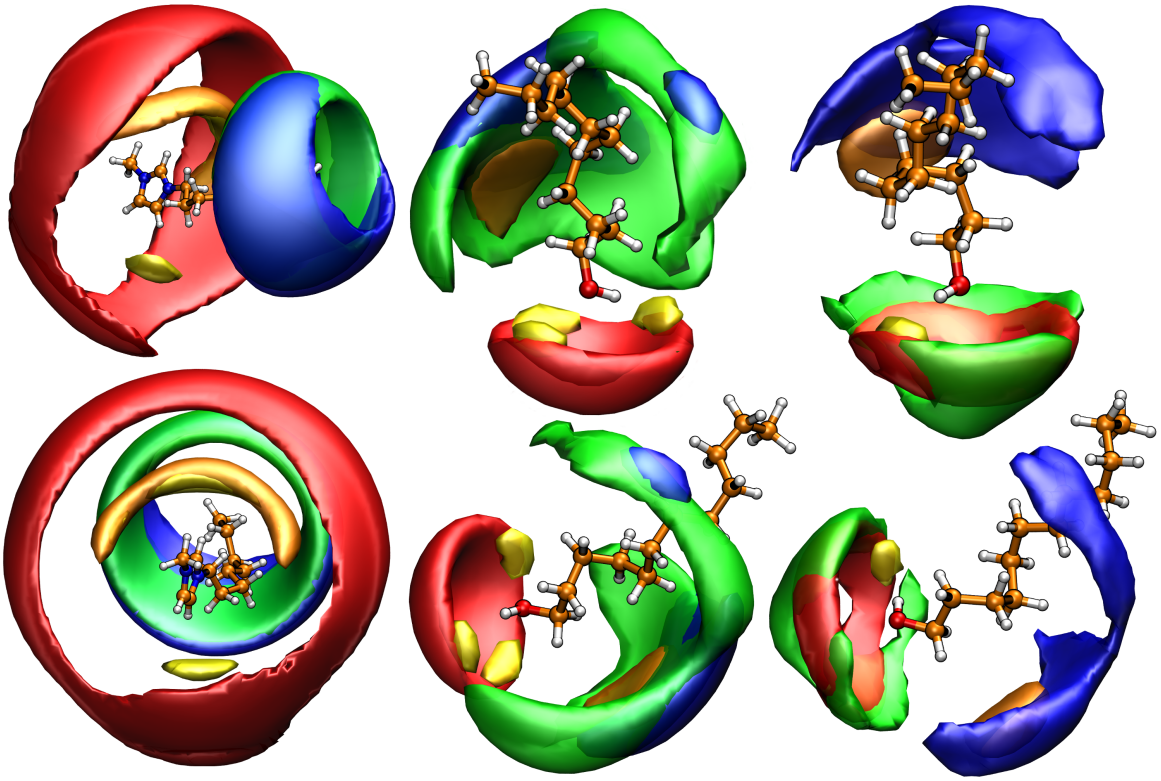

**Figure 4.3** SDFs for components around the $[C_8C_1Im]^+$ cation (left panels) and the *n*-dodecanol alcohol in $[C_8C_1Im][NTf_2]$ (middle panels) and the *n*-dodecanol alcohol in $[C_2C_1Im][NTf_2]$ (right panels). Colors were chosen similar to the colors for the snapshots, but here we distinguished between the anion and cation of the P-IL domain (cf. Figure 4.2: P-IL cation, red; P-IL anion, orange; N-IL, green; P-A, yellow; N-A, blue).

SDFs of the polar groups show the expected orientation around the cation. The anion (orange) and the alcohol's polar groups (yellow) are mostly located in the close proximity of the ring hydrogen atoms. The further cations are arranged in the second solvent shell, completing the network of ions of the IL solvent. It is interesting to observe that the isosurfaces that represent the spatial distribution of side chains from the alcohols and the IL cations around the cations do almost completely overlap, suggesting the lack of significant selection between these moieties by the IL cation.

The SDFs around the alcohol molecules also show some intriguing details regarding their solvation in the IL. The polar-polar interaction between the alcohol molecules is clearly visible in the three yellow spots at the hydroxyl group in the $[C_8C_1Im][NTf_2]$ solvent (Figure 4.3, middle). Such an interaction is also present in the IL $[C_2C_1Im][NTf_2]$, but not as pronounced (Figure 4.3, right). It is interesting to see that these weak hydrogen

bond acceptor anions do not often form a hydrogen bond with the alcohol, as the orange spots are missing at these locations. Instead, the anions occupy the positions around the carbon atoms that are adjacent to the hydroxyl group. It seems possible that the interaction between the anion and the alcohol molecule is weak, and the polar IL-alcohol interplay is dominated by the hydrogen bond between the cation as donor and the alcohol as acceptor. In this case, the occurrence of the anions in these positions is mostly due to the interaction with the IL cation, being in a hydrogen bond with the solute. The most important finding here concerns, however, the non-polar–non-polar interactions in the solvation. In agreement with the observations above, in $[C_2C_1Im][NTf_2]$, the alkyl group of the alcohol is predominantly interacting with other alcohol side chains, indicating a certain self-aggregation. However, in $[C_8C_1Im][NTf_2]$, the cationic side chains form an overwhelming shell around the alcohol. This underlines the increasing importance of the cation-alcohol interactions with the introduction of longer side chains in the cation, which opens the possibility of enforcing the distinct structure of the liquid on the alcohol itself. Having seen the changes in the mesoscale structure and in the solvation of alcohols in ILs, we will now focus on exploring how much the structure of the solvent is actually transferred into the solute in these particular cases, to see if the change in the solvent might indeed have a structure directing effect.

Angles were calculated for vectors defined along the alkyl side chains of the cations and distances were taken between the nitrogen atoms of the imidazolium rings, carrying the side chains. Lower panels consider angles defined by vectors along the alkyl side chains of the cations and the alkyl chains of the alcohols. Distances are measured between the nitrogen atoms of the imidazolium rings and the oxygen atoms of the alcohols.

To observe if the microscopic order of the liquid, that is, the orientation of the cations with respect to each other in the microheterogeneous structure of the IL, is transferred or enforced on the alcohol molecules, we employed combined distribution functions (CDFs), shown in Figure 4.4 and Figure 4.5. Here, we plot the mutual occurrence (shown by the color gradient and scaled individually for one row of plots) of two measures, in this case the distance between two entities ($d_1$, pm, for upper plots: distances taken between nitrogen atoms of the imidazolium rings; $d_2$, pm, for lower plots: distances taken between nitrogen

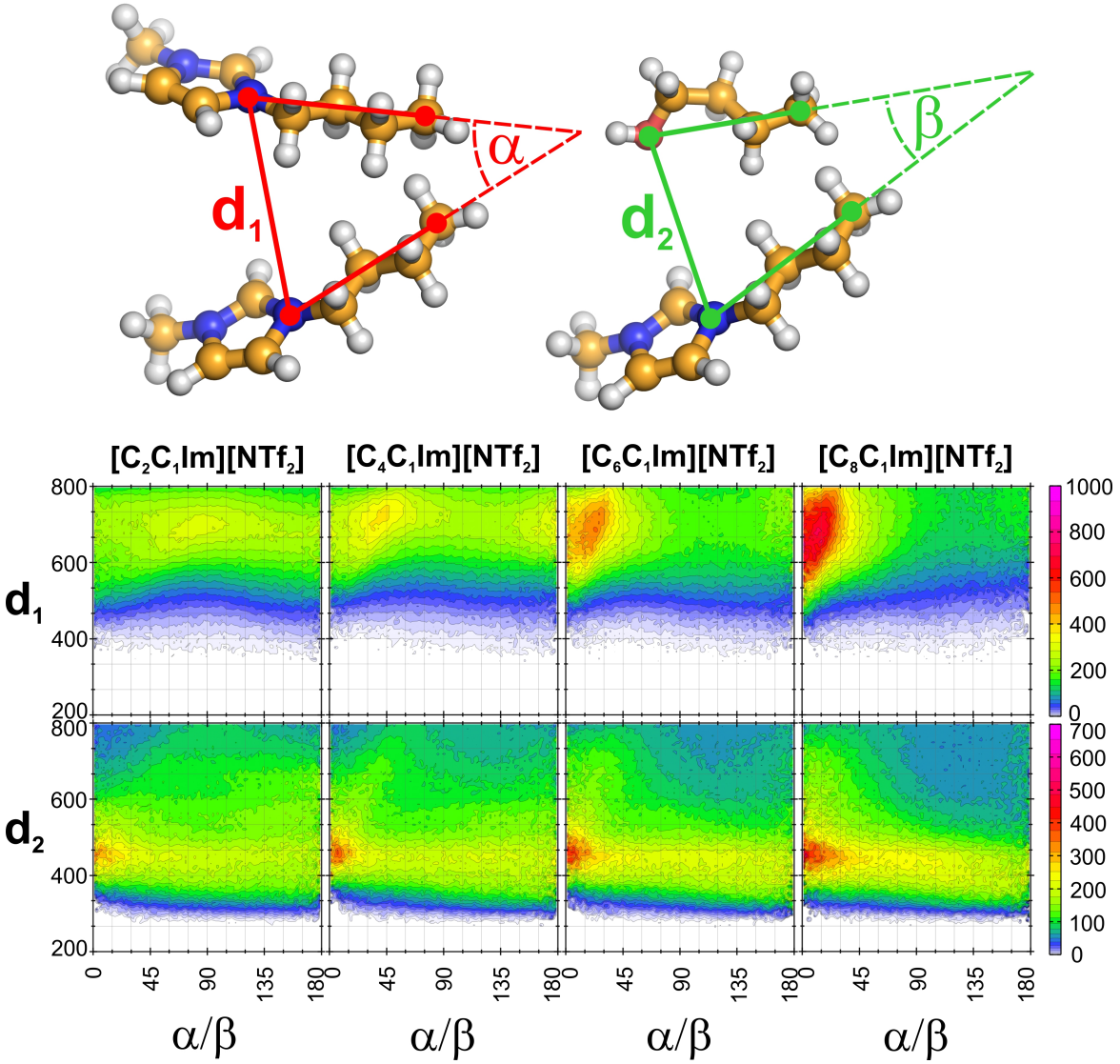


**Figure 4.4** Combined angular (y-axis, degrees) and distance (x-axis, pm) distribution functions that show the alignment of the cations with respect to each other (above) or the alcohols with respect to the cations (below) as a function of the distance for the mixtures of *n*-butanol and $[C_xC_1Im][NTf_2]$ ILs.

atoms of the imidazolium rings and oxygen atoms of the alcohols) and their relative orientation ($\alpha$, degrees, for upper plots: angles calculated for vectors defined along alkyl side chains of the cations; $\beta$, degrees, for lower plots: angles constructed by vectors along alkyl side chains of the cations and alkyl chains of the alcohols). From the plots that correspond to the cation-cation distances and orientations, that is, the upper row of plots in Figure 4.4 and Figure 4.5, it is apparent that the nearby cations (thus, where the distance is low) change their alignment when the side chain increases in length. In case

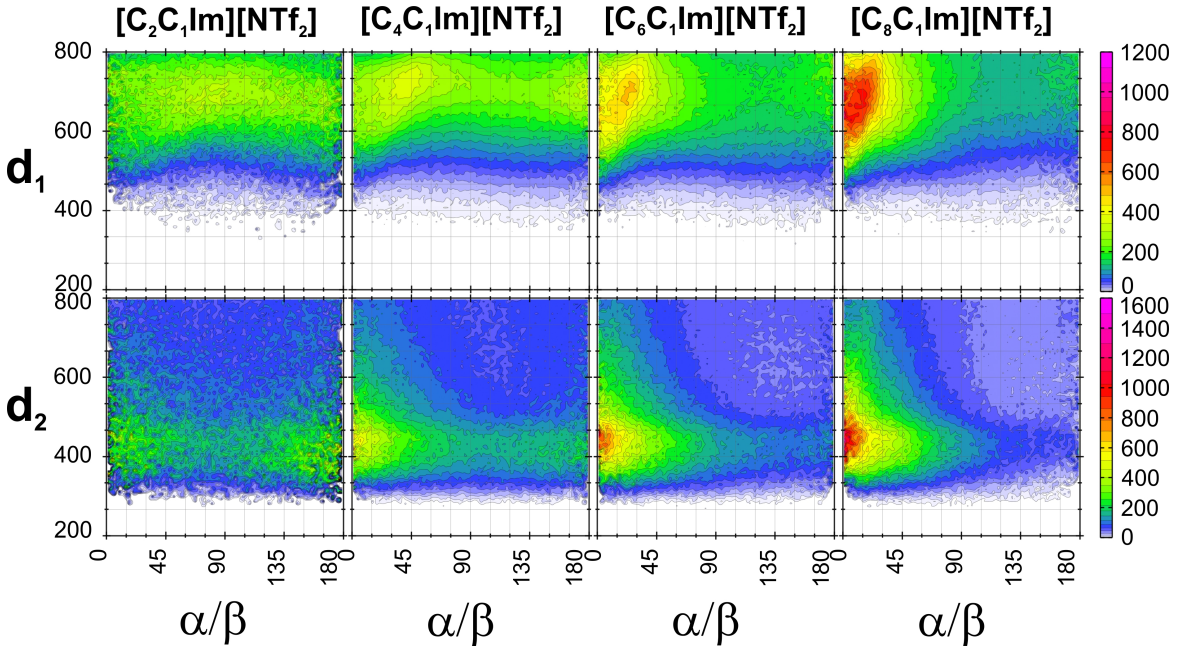


**Figure 4.5** Combined angular (y-axis, degrees) and distance (x-axis, pm) distribution functions that show the alignment of the cations with respect to each other (above) or the alcohols with respect to the cations (below) as a function of the distance for the mixtures of *n*-dodecanol and $[C_xC_1Im][NTf_2]$ ILs. The description of $d_1$ and $d_2$ can be seen in Figure 4.4 for the analogous *n*-butanol-IL mixtures.

of the shorter cationic side chains (ethyl and butyl) the cations arrange mostly randomly next to each other. In the case of the longer chains (hexyl and octyl), however, where the microheterogeneity is more and more expressed, the neighboring cations order more in a parallel fashion, as a distinct maximum arises at low distances and parallel orientations. This is the first direct proof for the qualitative description of microheterogeneous ILs being similar to surfactants in forming a non-spherical micelle-like structure. The similarity in the cation-cation orientations regardless of the alcohol chain length is also clearly visible, suggesting that the IL and not the alcohol determines the structure.

Apparently, the aforementioned order is transferred also to the cation-alcohol orientations: While in case of the shorter side chains, the alcohols orient mostly randomly next to the cations, in the microheterogeneous ILs, the alcohol-cation pairs clearly align in a parallel fashion next to each other. Considering the observations from the domain analysis, the present results show that while the polar hydroxyl group of the alcohol often anchors in the polar microphase, the side chains are pointing into the non-polar domain in a highly ordered way. Clearly, this parallel alignment produces a higher maximum

for *n*-dodecanol, showing that its longer side chain makes it easier to control its ordering in the liquid. It is interesting to point out, however, that although butyl groups on the cations are too short to form a well-defined continuous domain that stretches through the liquid, the butyl side chain of the *n*-butanol can be incorporated in the microheterogeneity of the ILs, and therefore this chain is apparently already long enough for the alcohol to incorporate in the structural order of the IL. Thus, according to the CDFs, the distinct structural order of microheterogeneous IL, described by the domain analysis and the cation-cation orientation CDFs, is strongly transferred into the orientation of the alcohol solutes in them, showing the presence of unambiguous template effects in ILs. This is, to our knowledge, the first time when such effects are proven in these highly applied solvents, which will expectedly lead the focus of experimental studies more to structure-directed synthesis in ILs.

## 4.4 Conclusion

In the present contribution, we applied selected analyses to classical molecular dynamics trajectories in order to observe template effects in ionic liquids (ILs). In our very simple model system we dissolved two alcohols, *n*-butanol and *n*-dodecanol, in 1-alkyl-3-methylimidazolium bis(trifluoromethylsulfonyl)imide ILs, where the alkyl side chains were varied from ethyl to butyl, hexyl and octyl groups. The analyses all show the increasing segregation of the non-polar from polar moieties as the side chain becomes longer, and indicate that the IL cations are oriented in a specific, parallel way. While the alcohol molecules tend to aggregate in the ILs with shorter side chains, they are more and more dispersed in the liquid upon moving towards the ILs having longer alkyl tails. Thus, they can be considered to dissolve in the non-polar IL microphase. Most importantly, not only their association but also their orientation changes with the different degree of microheterogeneity of the liquid, and the increasing order of the longer side chain ILs is imprinted in their alignment in the liquid. In particular, the polar part of the alcohol molecules mostly anchors to the polar microphase of the IL through strong polar-polar interactions, while the side chain of the alcohol stretches out parallel to the alkyl group

of the IL cation. Interestingly, this behavior changes in degree but does not dissipate when exchanging the *n*-dodecanol to *n*-butanol, despite the shortness of the side chain. Instead, the behavior seems to be determined primarily by the structure of the IL itself, which serves as a highly structured template for the orientation of the solutes.

The observed transfer of order from the solvent to the solutes has tremendous practical consequences for the application of ILs, as apparently we can, by the simple change of the solvent, manipulate the orientation of reactants, or otherwise valuable molecules. We can, thus, make molecules assume a certain conformation, or collide in the solution in a certain manner, which can definitely enhance some chemical processes in the liquid, while suppressing others, as it has been seen from the many examples in literature with other kind of template effects in chemistry. Being aware of these template effects will not only aid us to interpret regioselectivities of reactions in ILs that have already been experimentally explored but will also enable to consciously design solvent systems for reactions with the purpose of being more selective. It will be particularly interesting to see in the close future if the mesoscopic structure of the liquid can be imprinted directly into the morphology of (organic) polymers. Stereoselectivity and chirality are also highly interesting topics in that manner, since by introducing chiral microheterogeneous ILs template effects might increase the efficiency of the synthesis of the desired products.

## Acknowledgements

The authors thank the International Max Planck Research School for the support of R.E. B.K. would like to thank for the support from the Deutsche Forschungsgemeinschaft under the SPP 1708 project KI 768/15-1.

# 5 Ionic liquids as extraction medium

The sheer amount of already existing and theoretically thinkable ionic liquids and the possibility to further functionalize the ions leads to a broad portfolio of interactions and resulting structural and physicochemical properties, and makes them even capable of acting as structure-directing agents or templates. This great potential of ILs points towards the expansion of the use of these solvents for a broader range of applications.

While some mainly polar ILs are fully miscible with water, the functionalization with non-polar groups, that also leads to the formation of a microheterogeneous structure, can simultaneously make them sufficiently hydrophobic for extracting substances from an aqueous medium.[39–41] This property can also be beneficial for the efficient dissolution and capture of non-polar compounds that are to be extracted. Besides the many examples of successfully applied and established separation and extraction processes of a great variety of different materials,[42–51] ILs might as well be suitable to tackle one of the most severe and concerning problems of our time: the man-made pollution of the environment with plastics.[245–260]

The high amount of plastic waste that is emitted to the environment represents a serious threat, because it leads to smaller pieces of plastic, microplastics (MP, $< 5$ mm and $> 100$ nm) and nanoplastics (plastic nanoparticle, PNP, $< 100$ nm). These smaller units emanate from the physical degradation or chemical decomposition,[245,254,261–263] or from the digestive organs of different aquatic species.[264] Micro- and nanoplastics can be easily taken up by animals and are thus spread further via the food chain.[247–252,256,257,265–269] The number of studies about nanoplastics is now steadily increasing and the results are rather alarming.[260,270–278] For example, it was found that nanoplastic particles can enter individual cells,[260] and even alter the properties of lipid bilayers,[279,280] as well as those of proteins.[271–274] Thus, it is indispensable to search for — and eventually establish — strategies for the removal of these particles from the environment.[281] However, due to

the small size of PNPs and the existence of many different kinds of plastics with different physicochemical properties, there are huge challenges related to their separation and up to now there is no general strategy to remove plastic nanoparticles. Thus, it is of high importance to test alternative materials, like ILs, and to develop and establish novel procedures.

For gaining a general understanding of the interactions of PNPs with different potential extraction media and to model a phase transfer process, classical molecular dynamics simulations are predestined. Similar to the study above, the advantage here lies in the possibility to simulate large systems over long timescales with feasible computational effort.

As model systems pristine and oxidized polyethylene (PE) nanoparticles (consisting of 16 $C_{72}H_{144}$ chains) in a set of different ionic liquids, 1-alkyl-3-methylimidazolium bis(trifluoromethylsulfonyl)imide considering ethyl, butyl, hexyl and octyl side chains attached to the cation ($[C_xC_1Im][NTf_2]$, x = 2, 4, 6, 8) and 1-alkyl-3-methylimidazolium tetrafluoroborate with either ethyl or octyl groups attached to the cation ($[C_xC_1Im][BF_4]$, x = 2, 8), are chosen, and a comparison to molecular solvents with different polarity is conducted, in order to identify the advantages of ILs over other possible extractants. Additionally, an extraction process is modeled by simulating the phase transfer of a PE nanoparticle from an aqueous phase to an IL phase (either $[C_2C_1Im][NTf_2]$ or $[C_8C_1Im][NTf_2]$), revealing the thermodynamics and mechanism of this process.

# Ionic liquids as extractants for nanoplastics

Roman Elfgen,* Sascha Gehrke* and Oldamur Hollóczki*

*First published: 11 August 2020*

*DOI: 10.1002/cssc.202001749*

Reprinted with permission from:

R. Elfgen, S. Gehrke and O. Hollóczky, *Ionic Liquids as Extractants for Nanoplastics*, ChemSusChem (2020) 13, 5449–5459.



*Mulliken Center for Theoretical Chemistry, Institut für Physikalische und Theoretische Chemie, Rheinische Friedrich-Wilhelms-Universität Bonn, Beringstraße 4+6, 53115 Bonn, Germany

**Contributions to the manuscript**

- Running the molecular dynamics simulations
- Analysis of the trajectories
- Discussion of the results
- Writing the manuscript

**Abstract.** Plastic waste in the ocean and on land in the form of nanoplastics is endangering food and drinking water supplies, raising the need for new strategies for the removal of plastic nanoparticles from complex media. In the present contribution we suggest considering ionic liquids as extractants, since they show several advantageous properties that may facilitate the design of efficient separation processes. Through varying the anion and the side chain at the cation, the interactions between the extractant and the polymer can be strengthened and tuned, and thereby the disintegration of the particle into separate polymer chains can be controlled. Oxidized moieties can also be efficiently solvated, given the amphiphilic nature of the considered ionic liquids, allowing also realistic particles to be extracted into these solvents. The phase transfer was found to be thermodynamically and kinetically possible, which is supported by the complicated structure of the ionic liquid-water interface through the rearrangement of the interfacial ions, and the formation of a micelle around the plastic already at the edge of the aqueous phase.
**Keywords:** Nanoplastics, ionic liquids, extraction, molecular dynamics

## 5.1 Introduction

The high amount of plastic waste that is emitted to the environment poses a distinct threat to the environment, which is presently one of the most pressing ecological issues.[245–260] Smaller pieces of plastic, microplastics (MP, $< 5$ mm and $> 100$ nm) and nanoplastics (plastic nanoparticle, PNP, $< 100$ nm) are produced directly to use in diverse costumer products, or originate from physical degradation via mechanical processes or chemical decomposition.[245,254,261–263] In addition, evidence was found that Antarctic krill and potentially other species fragment microplastic beads to nanoplastics in their digestive organs.[264] Animals take up the plastic particles,[247–252,256,257] and spread them further via the food chain. As a result, plastics have been found in the bodies of various aquatic and terrestrial animals.[247,249–251,265–269]. We are consuming plastic particles by eating some of these animals, using sea salt,[253,282] drinking water, and using plastic packaging.[283,284]

There is an increasing number of studies showing potentially adverse effects of nanoplas-

tics, and the findings are rather alarming.[260,270–278] It was recently shown that nanoplastics can enter individual cells.[260] They can alter biologically relevant properties of lipid bilayers (and thereby cell membranes),[279,280] while our and other research groups have also shown their effects on proteins as well.[271–274] For this reason, it is paramount to establish strategies for the accurate measurement of PNP concentrations, and eventually for the removal of these particles from the environment and from consumption products.[281] Nguyen et al. recently gave an overview addressing the challenges related to the separation of small plastic particles and their analysis in complex samples.[285] For the isolation of plastic particles from such matrices exploiting the properties of plastics that make them different from their matrix is required. Recently, methods using electrosorption[286] and centrifugation emerged,[287] which can have applications in purification and analysis in the future. However, up to now there is no general procedure to remove MPs and PNPs, which prompts the need for the development of novel techniques.

In the present contribution we suggest the use of ionic liquids (ILs) as extractants for the removal of nanoplastics from aqueous media. The potential of these liquids lies in their almost infinite variety, allowing functionalization and fine-tuning of these solvents for any given task. Furthermore, the plethora of diverse interactions within ILs constitute a completely different environment from that of polar or non-polar molecular solvents. Similarly, whereas some ILs are fully miscible with water, some are sufficiently hydrophobic for applications in extracting from an aqueous phase;[39–41] a property, which might be beneficial also for the efficient dissolution of non-polar compounds that are to be extracted. For these reasons, ILs have been successfully applied for separation and extraction processes of a variety of different materials.[42–51] It has been repeatedly demonstrated that, if properly selected, IL-based solvents and materials can afford higher extraction yields and purification factors as compared to traditional solvents and materials.[45] Hereby we characterize the solvation of pristine and oxidized polyethylene plastic particles in a set of different ionic liquids, and compare it to molecular solvents with different polarity, in order to identify the advantages of these materials over other possible extractants. We explore the extraction process by simulating the phase transfer, revealing the thermodynamics and mechanism of this process.

## 5.2 Models and methods

### Simulated systems

The present study was performed on a polyethylene nanoparticle (PE-PNP), composed of 16 chains of $C_{72}H_{144}$ as a model system. In order to perform molecular dynamics simulations, we needed to produce a reasonable starting geometry for the PNP. The molecular structure of these materials is largely unknown, but they are expected to be mostly spherical aggregates of polymer chains in aqueous solutions.[288] We employed here our previously described[271,272,279] simulated annealing approach to produce the nanoparticle through a temperature program, involving the slow cooling and eventual nucleation of evaporated polymer chains, and their rearrangement into the desired low-energy structures.

The polyethylene nanoparticle was surrounded by the solvent molecules with the aid of the program PACKMOL (version 16.228),[208,209] in order to create the starting geometries for the simulations. Additionally, we performed simulations starting from dissociated polymer chains, which were placed into the simulation box individually and randomly by PACKMOL, to avoid imposing any kind of structure onto the system. The simulation box contained 25000 water molecules, 72 sodium cations and 72 chloride anions in case of saline, which corresponds to the physiological NaCl concentration. The number of solvent molecules in the other systems were: 7500 for ethanol, 5500 for tetrahydrofuran (THF), 5000 for toluene, and 1400 ion pairs for the ionic liquids. The Lewis structures of the ionic liquids are shown in Figure 5.1. For the simulation of the extraction process we set up an orthorhombic box, which contained two phases, separated along the Z axis. The first phase contained a nanoplasic particle and 24000 water molecules, while the other phase was composed of 1400 ion pairs of either $[C_2C_1Im][NTf_2]$ or $[C_8C_1Im][NTf_2]$.

### Classical MD simulations

The prepared systems were simulated using the LAMMPS program (version 12$^{th}$ April 2013).[144] Periodic boundary conditions were applied in order to avoid border effects. For

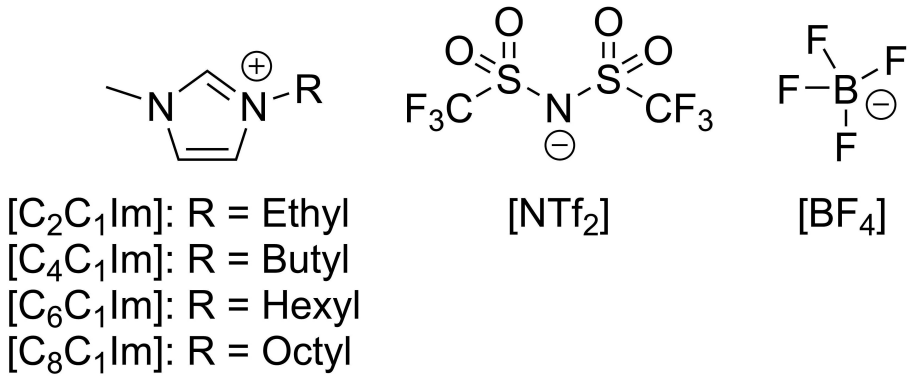


**Figure 5.1** Ionic liquid ions considered in this study.

the description of the IL cations and anions intra- and intermolecular interactions the force field parameters of Canongia Lopes and Pádua were chosen.[59,60] For the polyethylene chains as well as for the organic solvents ethanol, toluene and tetrahydrofuran the OPLS-AA model,[142] whereas for the simulation of water, the SPC/E water model was used.[289] In order to obtain Lennard-Jones cross terms, the Berthelot rule for $\varepsilon$ and the Good–Hope rule for $\sigma$ were applied.[136,290] All non-bonded interactions between the atoms were restricted to a cutoff radius of 10 Å, while for larger distances the particle-particle particle-mesh long-range correction was employed. The timestep was set to 1.0 fs. Initial simulations were performed in an NPT ensemble for 7.7 ns at a temperature of 293 K and under a pressure of 1 bar, which was controlled by Nosé–Hoover thermostat and Nosé–Hoover barostat, respectively.[211,291,292] Over the last 6 ns, the cell volume was averaged, which produced the cell vector that was employed for the subsequent NVT simulations. Table 5.1 summarizes the physical sizes of the periodic simulation boxes, obtained through NPT simulations. After 1.5 ns of further equilibration in the NVT ensemble at 293 K, for molecular liquids 10 ns while for the more viscous ionic liquids 30 ns production runs were performed, again in the NVT ensemble.

In case of simulating the phase transfer processes, the polyethylene nanoparticle was initially located in the aqueous phase. An additional harmonic force, a bias potential was applied in the system to keep the Z component of the distance vector between the centers of mass of the IL phase and the nanoplastic at 85 Å. Over 6 ns of simulation in the NPT ensemble, the volume of the simulation box was averaged to determine the final

**Table 5.1** Cell vectors of the cubic periodic simulation box (in Å) after equilibration in the NPT ensemble for each systems with the globular polyethylene nanoparticle (PE-PNP), and the dissociated polyethylene chains.

| Solvent | PE-PNP | PE-Chains |
|---|---|---|
| Saline | 92.1428 | 92.1478 |
| Ethanol | 90.7434 | - |
| Tetrahydrofuran | 92.5610 | - |
| Toluene | 97.2398 | 97.2573 |
| $[C_2C_1Im][NTf_2]$ | 86.6628 | 86.6478 |
| $[C_4C_1Im][NTf_2]$ | 89.9599 | - |
| $[C_6C_1Im][NTf_2]$ | 93.0614 | - |
| $[C_8C_1Im][NTf_2]$ | 95.9671 | 95.9794 |
| $[C_2C_1Im][BF_4]$ | 73.4861 | 73.4464 |
| $[C_8C_1Im][BF_4]$ | 86.0987 | 85.9369 |

cell vectors for the subsequent NVT runs. The system was then equilibrated for another 0.25 ns, followed by a 1 ns production run, during which the force applied through the bias potential, to keep the nanoparticle in the desired position in the Z direction, was averaged. The bias potential was shifted from 85 Å to 0 Å with 1 Å increments, repeating the 0.25 ns equilibration and 1 ns production run at each distance. The integral of the obtained average forces against the distance gave the free energy profile of the extraction.

## Analysis

For analyzing the trajectories we used the TRAVIS software.[15,86,87] Much of the analysis discussed in the present paper relies on Voronoi analysis. Through Voronoi analysis, all atoms are assigned a cell, and thereby all atoms have volume and surface. The connectivity of these Voronoi cells can be analyzed in a systematic manner, which holds crucial information regarding the spatial distribution (dispersivity) and orientation of the components within the simulation box. The area of contact surfaces between two cells, viz. two atoms, can also be quantified and summarized in a systematic way.

Through grouping Voronoi cells that belong to chemically analogous moieties, subsets

can be defined, e.g. alkyl groups of IL cations, or ionic components. The connectivity of these subsets can be analyzed by the domain analysis tool of TRAVIS,[15] which can identify how many continuous domains a given kind of subsets forms. The average of this number over time we will call henceforth domain count $N$. If $N$ equals the total number of individual subsets in the simulated system (e.g. 1400 alkyl side chains of the cations), all these subsets are dispersed spatially, and separated by other components of the liquid, whilst any value for $N$ smaller than that represents a certain level of aggregation in the system. If the domain count is one, it means that the subsets form a single large, continuous network. The total surface area $A$ of a given kind of domain can also be calculated by summing up the contact surfaces of the constituting cells with subsets that do not belong to the domain in question. Next to $N$, $A$ can provide another quantitative measure for how dispersed certain subsets or components in the liquid are, and how much the shape of the given domain is altered. The plastic was always considered to be a separate subset, while the definitions of the polar and non-polar subsets in the ionic liquids are shown in Figure 5.2.

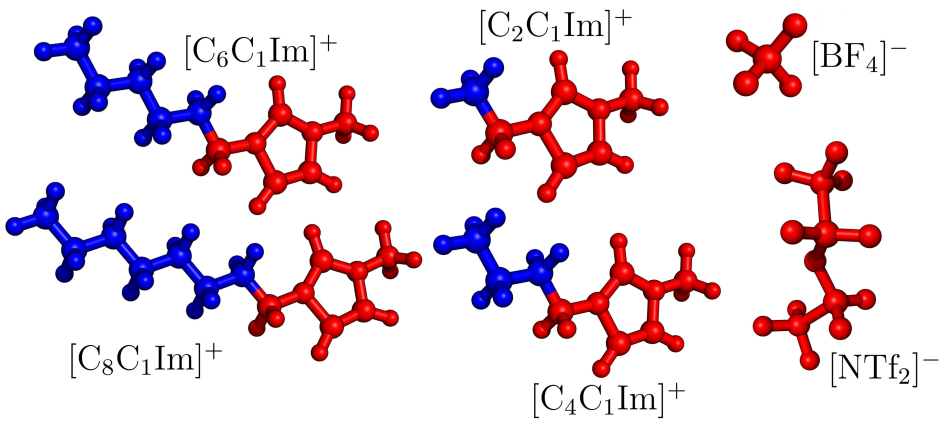


**Figure 5.2** Definitions of the polar (red) and non-polar (blue) subsets of ionic liquids, as used throughout the article.

## 5.3 Results and discussion

Plastics are often based on non-polar materials, hence the solvation of PNPs should be highly affected by the polarity of the solvent. To establish a basic understanding on the

solvation of PNPs, a polyethylene (PE) particle with a diameter of ca. 5 nm, composed of 16 $C_{72}H_{144}$ chains, was simulated in selected molecular solvents that exhibit different polarity: isotonic saline solution, ethanol, tetrahydrofuran, and toluene. When inspecting the geometry of the last snapshot of the trajectories (Figure 5.3), already at first glance it is apparent that the PNP behaves very differently in these solvents. In water and ethanol, which are the two most polar solvents here, the PE particle retains its globular form, whereas it dissolves in the two non-polar solvents tetrahydrofuran and toluene. Under closer scrutiny, the particle appears to be very compact in water, thereby minimizing its surface area exposed to the polar solvent. In contrast, the plastic nanoparticle in ethanol shows a notably rougher surface and thus a higher surface area to enable more interactions between the non-polar PE chains and the non-polar ethyl groups of the ethanol molecules. However, ethanol still possesses a high ratio of polar moieties, which form an extensive hydrogen bonding network in the liquid, not allowing for a further unfolding and disentanglement of the PE chains. The even less polar solvents tetrahydrofuran and toluene allow for a dissociation of the PE chains in order to maximize the attractive non-polar-non-polar solute-solvent interactions.

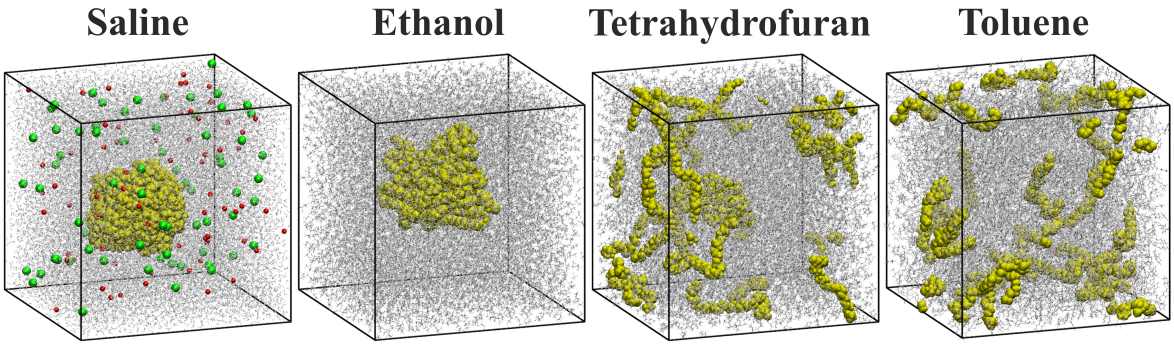


**Figure 5.3** Snapshots of the simulations with molecular solvents (grey) and the polyethylene nanoparticle (yellow) after 10 ns of simulation. The $Na^+$ and $Cl^-$ ions are depicted in red and green, respectively.

In order to quantify the above described effects, we performed a domain analysis, distinguishing between the solvent and PE, defining the two subsets S and PE, respectively. Table 5.2 shows the average number of domains $N$ emanating from each subset as well as the average surface area of PE covered by the solvent $A^{\mathrm{PE}}$. The results confirm that within water and ethanol the PE chains stay aggregated and form one single domain.

**Table 5.2** Domain analysis[15] data, describing the solvation of the plastic nanoparticle in molecular solvents. The number of domains composed of the solvent molecules and the polyethylene ($N^{\mathrm{S}}$, and $N^{\mathrm{PE}}$, respectively) as well as the surface area of the polyethylene $A^{\mathrm{PE}}$ are shown. Of the 10 ns simulation, only the last nanosecond is used for calculating the averages presented here.

| System | $N^{\mathrm{S}}$ | $N^{\mathrm{PE}}$ | $A^{\mathrm{PE}}$ / Å$^2$ |
|---|---|---|---|
| Saline | 1.0 | 1.0 | 7213.4 |
| Ethanol | 1.0 | 1.0 | 10167.2 |
| Tetrahydrofuran | 1.0 | 5.6 | 24938.0 |
| Toluene | 1.0 | 6.8 | 25409.8 |

The outer surface area of the PNP is approximately 41% larger in ethanol than in water, which means that although the chains that constitute the particle stay associated, they loosen their compact structure in order to expose more of the polymers to the solvent.

In tetrahydrofuran and toluene the dissociation of the PNP particle into separate chains can be observed through the increased domain counts for the PE ($N^{\mathrm{PE}}$, Table 5.2). This effect is notably stronger in the case of toluene, in which $N^{\mathrm{PE}}$ yields a value of 6.8, in contrast to the value 5.6 for tetrahydrofuran. This finding is in agreement with the trends in polarity. Due to this more effective dissociation in toluene, the PE surface area is somewhat larger than in tetrahydrofuran ($A^{\mathrm{PE}}$, Table 5.2). Repeating the simulations from the dissociated polyethylene chains gave qualitatively the same result: In saline solution the plastic readily formed a PNP, while in toluene the polymers remained dissociated through the whole simulation.

The trends in the disintegration of the PNP to individual polymer chains as described above unequivocally prove that the non-polar molecular solvents have more favorable interactions with the PNP. Accordingly, it is very likely that non-polar solvents can be used for the extraction of pristine PNPs, and these structures dissociate to individual chains within these media. However, such disintegration of the particle might not be advantageous. If the biological decomposition of the plastic is the aim, the fragmentation of the PNPs might be desired, providing better access for digestive enzymes of bacteria to the polymer chains.[293–295] On the other hand, fragmentation creates smaller particles, which

are generally believed[260] — albeit argued[296] — to be more harmful, if they re-enter the purified solution in the presence of e.g. surfactants. Furthermore, the aim of the extraction may also be to create a solution with a higher concentration of PNPs from complex environmental samples, which can be analyzed in terms of size distribution, and occurrence.[287] Obviously, in case of such an application, the disintegration of the particles to individual chains or their aggregation into larger species is disadvantageous. Furthermore, dissolution of the PNP may release compounds that are adsorbed on or absorbed in it,[297] including drugs, pesticides, plastic additives, which can also pose certain health and environmental risks. For these reasons, it seems vital that the level of PNP disintegration, i.e. the dissociation of the chains that constitute these particles are carefully controlled, adjusted to the problem at hand.

As shown above, the polarity of the solvent has a significant influence on the solvation of the PNP, and probably this feature must be fine-tuned to fulfill the criteria above. In this regard, ionic liquids (ILs) are promising extractants, since the polarity and hydrophobicity of these compounds can be adjusted easily through varying the anionic and cationic moieties, and the non-polar side chains. Furthermore, it has been discussed in literature for more than a decade that some ILs possess a unique microscopic structure, called microheterogeneity.[7,8,11,13–15,164,242,298] This phenomenon arises from the mismatch of polar and non-polar groups of the liquid, which results in the spatial separation of polar and non-polar domains, sometimes referred to as microphases, within the macroscopically homogeneous liquid. The presence of this peculiar structure has been the source of many intriguing properties of ILs, including their excellent structure directing effect in material synthesis.[164] For the extraction, this property might be also useful for two reasons. Firstly, the polar and non-polar domains have a well-defined structure in any given ionic liquid, with characteristic shapes and sizes.[11,14,15,298] These pre-defined dimensions may impose a certain selectivity to the extraction, dissolving only those particles that are small enough to fit into this network of domains. Secondly, PNPs are often not pristine, but they contain — next to the actual polymer – additional compounds. These can be amphiphilic molecules adsorbed onto the PNPs surface[271,299] (e.g. amino acids with non-polar side chains[271]), and thereby solubilizing it in a micelle-like structure, or

polar substituents on the polymer chains, produced by the partial oxidation of the PNP surface by air and sunlight[300,301] or oxidative wastewater treatment.[302] For weathered macroscopic polyethylene species, both processes have been observed through spectroscopic measurements.[300] Whilst the former structures can be removed from the PNP during the phase transfer, solvated thereafter separately from the PNP in either of the two phases, the latter ones are covalently attached to the particle, and therefore they must enter the IL phase together with the rest of the PNP. The presence of separate polar and non-polar microphases within the solution should offer an excellent medium for the simultaneous solvation of both kinds of moieties with different polarity.

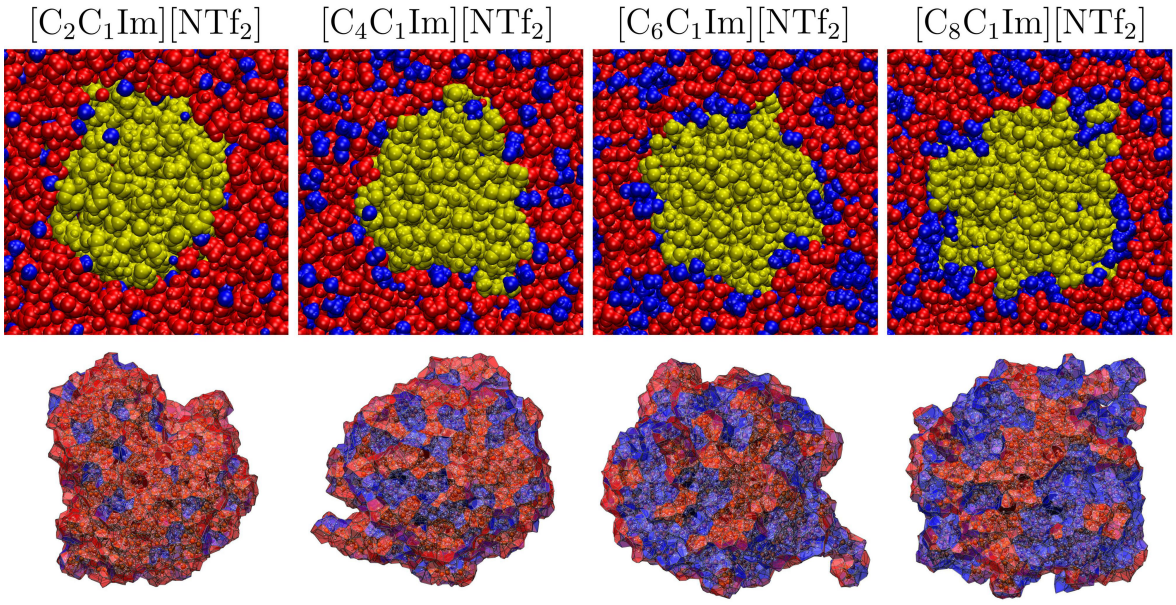


**Figure 5.4** Segments of the simulation boxes containing the polyethylene nanoparticle (yellow) in the different $[C_nC_1Im][NTf_2]$ ionic liquids (polar domain: red; non-polar domain: blue; see Figure 5.2), after 30 ns of simulation. Below each segments the Voronoi cell of the polyethylene particle is shown, with color indicating the polar (red) or non-polar (blue) nature of the neighboring moieties at each face of the cell.

As model IL extractants for the PE-PNP, we chose 1-alkyl-3-methylimidazolium bis(trifluoromethylsulfonyl)imide salts, with ethyl, butyl, hexyl, and octyl alkyl side chains ($[C_2C_1Im]$, $[C_4C_1Im]$, $[C_6C_1Im]$, $[C_8C_1Im]$, respectively, see Figure 5.1), which exhibit an increasing degree of microheterogeneity in this order.[15,164] To vary the anion, we also studied 1-ethyl-3-methylimidazolium tetrafluoroborate and 1-octyl-3-methylimidazolium tetrafluoroborate ILs. The two anions considered here, bis(trifluoromethylsulfonyl)imide

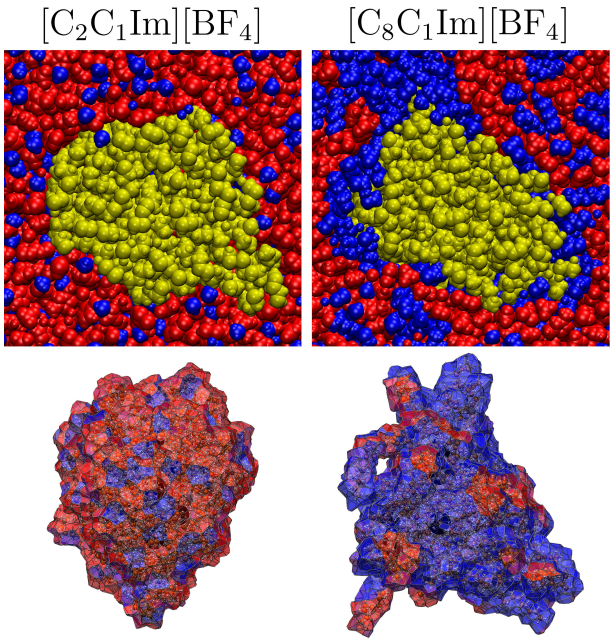


**Figure 5.5** Segments of the simulation boxes containing the polyethylene nanoparticle (yellow) in the different $[C_nC_1Im][BF_4]$ ionic liquids (polar domain: red; non-polar domain: blue; see Figure 5.2), after 30 ns of simulation. Below each segments the Voronoi cell of the polyethylene particle is shown, with color indicating the polar (red) or non-polar (blue) nature of the neighboring moieties at each face of the cell.

and tetrafluoroborate ($[NTf_2]$ and $[BF_4]$, respectively), are both hydrophobic, making the corresponding ILs largely immiscible with water.[39] Visible already at the segments of the snapshots shown in Figure 5.4 and Figure 5.5, by the increase in side chain length the polar (red) and non-polar (blue) domains become more segregated in the liquid, as observed previously.[7,8,11,13–15,164,242,298] This is fully corroborated by the domain analysis (Table 5.3), which shows that while the polar domain includes all polar subsets into a single network of ions in all systems, the number of non-polar domains ($N^N$) decreases from 667.1 in case of $[C_2C_1Im][NTf_2]$ to 2.8 in case of $[C_8C_1Im][NTf_2]$. It is worth mentioning here that the number of non-polar domains have been found to be $N^N = 1.0$ for the neat ionic liquids with a side chain length longer than a hexyl group,[15,164] which shows that the nanoplastic separates some of the solvating ions from the non-polar domain, and creates its own environment within the liquid. Due to the smaller size of the anion, in the $[BF_4]$-based ILs the non-polar moieties can form larger, more uninterrupted domains in the liquid than in the corresponding $[NTf_2]$ derivatives (cf. $r^N$ and $N^N$ in Table 5.3).

**Table 5.3** Domain analysis data[15] for the systems containing the ILs and the polyethylene nanoparticle. The average volume percentage of non-polar domains in the liquid ($r^N$), the average number of polyethylene ($N^{\mathrm{PE}}$), polar ($N^{\mathrm{P}}$) and non-polar domains ($N^{\mathrm{N}}$), as well as the average total outer surface area of the polyethylene particle ($A^{\mathrm{PE}}$), and the average surface area of the plastic particle covered by the non-polar domain of the ionic liquid are ($A^{\mathrm{PE/N}}$) presented, together with literature viscosity ($\eta$). Only the last ns of the 30 ns simulation was used to calculate the averages.

| System | $r^{\mathrm{N}}$ | $N^{\mathrm{PE}}$ | $N^{\mathrm{P}}$ | $N^{\mathrm{N}}$ | $A^{\mathrm{PE}}$ | $A^{\mathrm{PE/N}}$ | $\eta$ |
|---|---|---|---|---|---|---|---|
| | % | | | | Å$^2$ | Å$^2$ | mPa s |
| $[C_2C_1Im][NTf_2]$ | 9.45 | 1.0 | 1.0 | 667.1 | 8211.0 | 1331.6 | 40[a] |
| $[C_4C_1Im][NTf_2]$ | 20.10 | 1.0 | 1.0 | 89.1 | 8766.7 | 3261.6 | 63[a] |
| $[C_6C_1Im][NTf_2]$ | 29.03 | 1.0 | 1.0 | 15.1 | 9503.8 | 5208.7 | 90[a] |
| $[C_8C_1Im][NTf_2]$ | 40.18 | 1.0 | 1.0 | 2.8 | 10376.5 | 6707.2 | 120[a] |
| $[C_2C_1Im][BF_4]$ | 14.60 | 1.0 | 1.0 | 303.9 | 8697.7 | 2440.4 | 67[b] |
| $[C_8C_1Im][BF_4]$ | 51.81 | 1.0 | 1.0 | 1.7 | 11651.2 | 9348.9 | 439[b] |

[a] experimental values taken from Ref[303]

[b] experimental values taken from Ref[304]

The solvation of the PNP varies in the different ILs. The PNP is apparently encompassed by the non-polar domain, and the proportion of the surface covered by the non-polar moieties of the solvent increases significantly towards the ILs with longer cationic side chains (Figure 5.4, Figure 5.5, and Table 5.3). Although the polyethylene chains that build the particle remain associated throughout the simulations (see $N^{\mathrm{PE}}$ in Table 5.3), the particle strongly reacts to the presence of the IL, as shown by the changes in its total surface area $A^{\mathrm{PE}}$ (Table 5.3). $A^{\mathrm{PE}}$ is larger compared to that in water already in the most polar $[C_2C_1Im][NTf_2]$, and increases steadily towards the less polar ILs with longer side chains up to the octyl derivative. In Figure 5.4 and Figure 5.5 it can also be observed that the unfolding of the polymer chains from the particle occurs at those positions, where the non-polar domains are in contact with the PNP. The highest surface area of the particle is similar to that in ethanol. These observations are consistent with stronger solute-solvent interactions of the PNP within the IL than within an aqueous solution, suggesting a higher solubility of the PNP in the IL than in water. In accordance with the trends in the size of the anions, and in the corresponding volume ratio of the (for the plastic apparently more

attractive) non-polar moieties in the liquid ($r^{N}$, Table 5.3), the 1,3-dialkylimidazolium tetrafluoroborate derivatives show higher surface areas than those with the $NTf_2$ anion, indicating a more intensive interplay between the particle and the solvent.

Thus, the trends shown in the $N$ and $A$ data in Table 5.3 seem to be reasonable, as they represent a good correlation between the degree of rearrangement of the PE chains within the PNP and the polarity trends of the IL solvents. However, there are some limitations of MD simulations, which are worth pointing out in the present context. A statistically meaningful description of the transition between two states — e.g. the globular nanoparticle, and the dissolved, dissociated PE chains — can be achieved only if both states are sampled. In practice, this means that the transition from one state to the other — in this case the dissolution/disintegration process — occurs within the time frame of the simulation. ILs are highly viscous solvents (see Table 5.3), which should lead to a relatively slow mass transport within the liquid. In classical MD simulations the diffusion of the ions is known to be underestimated,[305] making a dissolution process in these model systems even slower. It is, therefore, possible that the PNP would dissolve in these ILs, but within the accessible time range of the simulations the rearrangements that are involved in the disintegration of the particle cannot be completed. For most ILs the $N$ and $A$ values fluctuate roughly around a constant value through the simulation (see Figure 7.4 and Figure 7.5 in the appendix), suggesting that they have indeed reached an equilibrium state, and the data presented in Table 5.3 are physically realistic. The only exception was $[C_8C_1Im][NTf_2]$, in which case both quantities drifted slowly towards higher values, indicating an ongoing disintegration process.

To overcome this problem, we performed further simulations with the $[C_2C_1Im][NTf_2]$, $[C_8C_1Im][NTf_2]$, $[C_2C_1Im][BF_4]$, and $[C_8C_1Im][BF_4]$ ILs, having the dissociated PE chains distributed randomly in the solution. In case of accurate sampling, the two sets of calculations — with the globular and disintegrated PNP — should converge into similar structures. The last snapshots of these simulations are presented in Figure 5.6, while the domain analysis data are shown in Table 5.4. The difference to the structures and data from the simulations with the PNP is striking. When plotting $N$ and $A$ against time, it becomes clear that the chains start to aggregate throughout the simulation in case of

all ILs (see Figure 7.6 and Figure 7.7 in the appendix). These two sets of structures are possible to compare through their average potential energy over the last ns of the simulations, revealing which of the two states are closer to the preferential conformation of the system. According to the energies, the PNP is more stable in all ILs, except for $[C_8C_1Im][NTf_2]$. Thus, according to the energetic data and the trends in the variations in $A$ and $N$ values, the PNP is supposed to avoid disintegration in all $[BF_4]$ ILs and in $[NTf_2]$ ILs with a shorter side chain. In contrast, in $[C_8C_1Im][NTf_2]$ the dissociated state is more stable, and therefore in this ionic liquid apparently the dissociation to individual chains should occur.

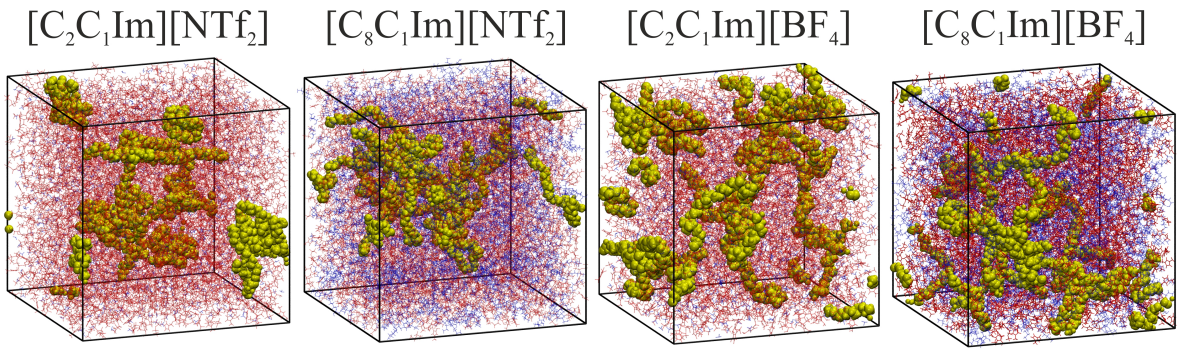


**Figure 5.6** Simulation boxes containing the polyethylene chains (yellow) in the different ionic liquids (polar domain: red; non-polar domain: blue), after 30 ns of simulation.

**Table 5.4** Domain analysis for the systems containing the polyethylene chains. The number of polyethylene ($N^{PE}$), polar ($N^{P}$) and non-polar domains ($N^{N}$), as well as the total outer surface area of polyethylene (viz. polyethylene-solvent contact area, $A^{PE}$) are presented.

| System | $N^{PE}$ | $N^{P}$ | $N^{N}$ | $A^{PE}$ Å$^2$ | $A^{PE/N}$ Å$^2$ |
|---|---|---|---|---|---|
| $[C_2C_1Im][NTf_2]$ | 3.5 | 1.0 | 681.2 | 21741.2 | 2525.0 |
| $[C_8C_1Im][NTf_2]$ | 3.7 | 1.0 | 3.7 | 25603.8 | 12978.1 |
| $[C_2C_1Im][BF_4]$ | 2.0 | 1.0 | 328.1 | 22402.0 | 4321.1 |
| $[C_8C_1Im][BF_4]$ | 4.0 | 1.0 | 1.3 | 22996.9 | 13633.6 |

As mentioned above, we suggest that the amphiphilic nature and the corresponding microstructure in ILs is beneficial for the extraction of partially oxidized PNPs as well,

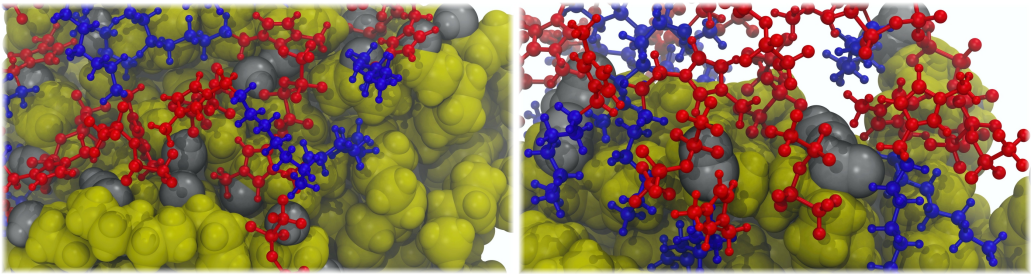

**Figure 5.7** Aggregation of polar moieties of the IL at the hydroxyl (left) and formyl (right) substituents of partially oxidized polyethylene nanoparticles after 30 ns of MD simulation (yellow: polyethylene; silver: polar substituents on polyethylene; red: polar domain of the IL; blue: non-polar domain of the IL).

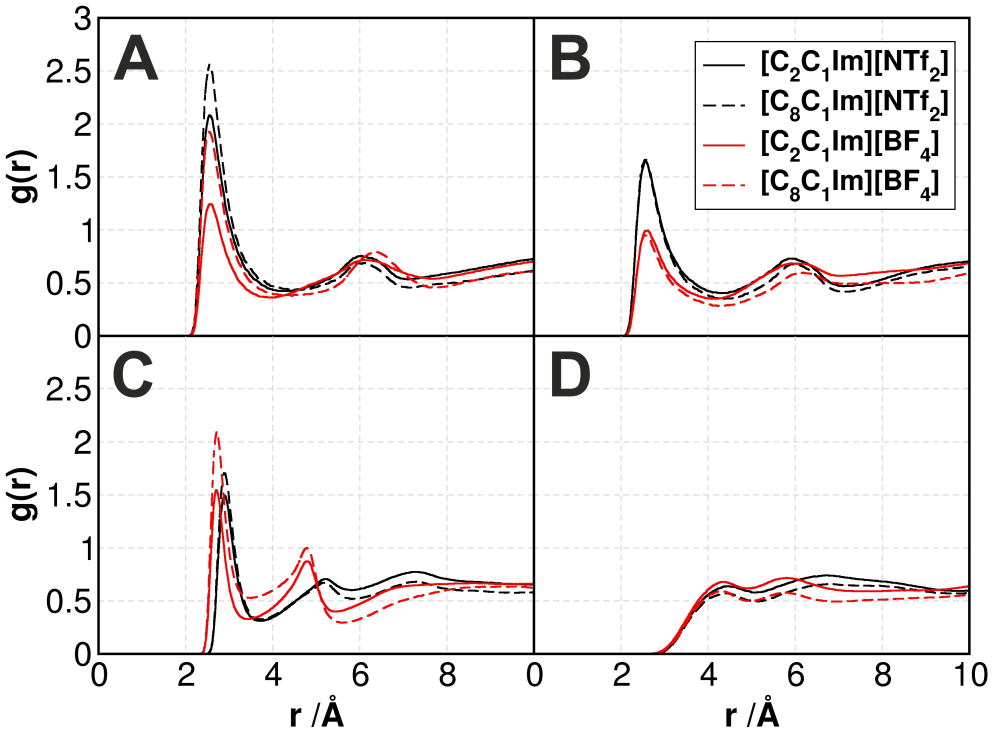


**Figure 5.8** Radial distribution functions, representing the interactions of the ionic liquid solvents with the oxidized nanoplastic particle. **A**: interactions between the -OH oxygen atoms of the hydroxyl-substituted polyethylene and the H2 hydrogen atom of the imidazolium ring; **B**: interactions between the -CHO oxygen atoms of the formyl-substituted polyethylene and the H2 hydrogen atom of the imidazolium ring; **C**: interactions between the -OH oxygen atoms of the hydroxyl substituted polyethylene and the oxygen or fluorine atoms of the anions; **D**: interactions between the -CHO oxygen atoms of the formyl-substituted polyethylene and the oxygen or fluorine atoms of the anions.

since the ions that constitute the IL extractant can orient themselves at the surface of the PNP in a manner that they maximize the like-like interactions. To verify this hypothesis, we modified the surface of the PNPs, and decorated it with polar groups, which are consistent with possible oxidation processes.[300,301] In one set of simulations -OH groups were added at 49 randomly chosen interfacial sites, while in another set -CHO substituents were introduced at the same sites. In case of the shorter side chains it is clearly possible for these polar groups to be covered by the polar domain, since the overwhelming majority of the liquid consists of the ionic moieties (see $r^{\mathrm{N}}$ in Table 5.3). In case of the longer chains, however, one could argue that through the solvation of the PNP surface by the long alkyl groups of the IL cation the ionic moieties do not have access to the polar hydroxyl or formyl groups, and thereby their stabilization is not possible. According to our simulations, however, all these oxidized regions are covered with a high concentration of the polar domain of the IL (Figure 5.7). According to the radial distribution functions (RDFs, Figure 5.8A-B), the strongest[306] hydrogen bond donor site of the imidazolium cation, at position 2 of the ring, can form hydrogen bonds with the oxygen atom of both functional groups considered here. Since the [$BF_4$] anion is a significantly stronger hydrogen bond acceptor than the [$NTf_2$], the ring hydrogen atoms of the latter kind of ILs are more accessible for interaction with the oxidized groups, shown by the higher $g(r)$ values for the corresponding peaks. In fact, in case of the -CHO groups, the first peaks barely reach the $g(r) = 1$ value, although it has to be mentioned here that due to the limited spatial accessibility of the sites — hindered by the plastic chains and the bulk of the PNP itself — these values can already by considered statistically relevant. Furthermore, the hydrogen bond donor capacity of the -OH groups attracts the anions (Figure 5.8C). In agreement with the trends in hydrogen bond acceptor strength, the [$BF_4$] anions aggregate more at these sites. The RDF peaks indicate that the association of the polar moieties of the IL to the oxidized functional groups of the PNP is roughly independent of the side chain length, as the slight increase for the longer side chains can be partly attributed to the lower concentration of polar group in a unit volume of the IL, which causes through dilution effects an increase in the peak heights when calculating the $g(r)$. Therefore, taking into consideration the high degree of oxidation in waste plastic,[300,301] ILs should

be excellent solvents for PNP extraction from realistic environmental samples.

Regarding the phase transfer process, the side chains and the corresponding microheterogeneity raises further questions, which have to be considered. ILs are known to form distinct structures at interfaces, including those with water.[49,307–310] At the aqueous interface, ILs present their polar moieties towards the water. Such a highly charged and polar interface could be considered as a barrier for the phase transfer of the non-polar PNP, since it has to overcome the non-favorable interactions with the polar groups before arriving in the stabilizing bulk IL media. For this reason, and to further understand the extraction process, we modeled the phase transfer of the PNP from an aqueous phase to an IL phase for two example ILs: $[C_2C_1Im][NTf_2]$ and $[C_8C_1Im][NTf_2]$.

Moving the particle slowly from one phase to the other, the structural changes that lead to the phase transfer can be tracked. In the beginning of the simulation, with the particle being far away from the interface within the bulk of the aqueous phase, the structure of the IL-water interface can be observed. In $[C_8C_1Im][NTf_2]$, this region is structured in two ways: Firstly, the IL ions point their polar part towards the aqueous phase, to maximize the Coulombic interactions between the IL and water (Figure 5.9 upper left). Secondly, the microheterogeneity of the IL can be recognized already at this region, exhibiting also some non-polar moieties directly underneath the first layer of the polar domain at the interface (Figure 5.9 lower left).

Already at a larger distance from the ionic liquid phase, the PNP attracts some $[C_8C_1Im]$ cations, which are then adsorbed at its surface within the aqueous phase, forming a partial micelle, as expected from an amphiphilic molecule. As the particle is moved closer to the IL, the water-IL interface is deformed, so that the water-PE surface with an unfavorable mismatch of polar and non-polar interactions can be minimized (see second panel from the left, Figure 5.10). As the PNP approaches the IL even more, the IL interface at the particle rearranges, so that the non-polar moieties of the IL cations directly adjacent to the water/IL interface can get in contact with the polyethylene (Figure 5.9 upper and lower right). In other words, the interfacial IL cations reorient in a manner that they can point their non-polar side chains towards the approaching plastic. In the light of the above results, if the polyethylene surface should contain any oxidized groups

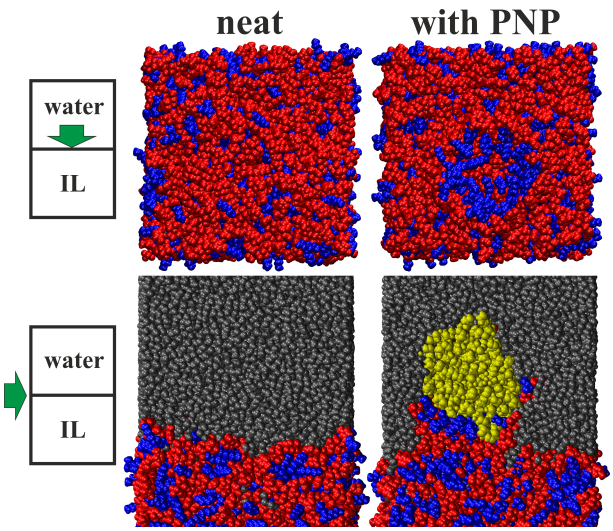


**Figure 5.9** Domain structure of the $[C_8C_1Im][NTf_2]$/water interface (blue: non-polar; red: polar; yellow: polyethylene; grey: water; for the color definitions, see Figure 5.2). Structural rearrangement of the IL ions upon the presence of a polyethylene nanoparticle. Note that in the top right panel the plastic nanoparticle (omitted for visibility) changes the surface structure, making the predominantly polar surface mostly non-polar through the rearrangement of IL ions.

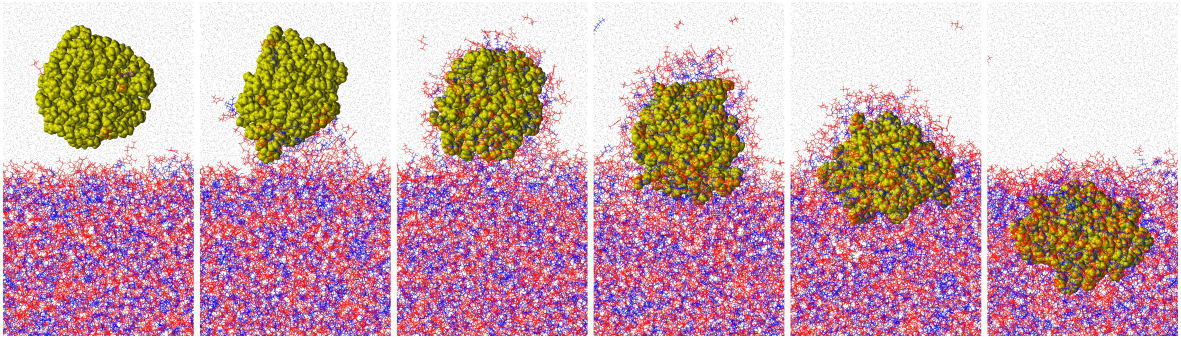

**Figure 5.10** Phase transfer of a polyethylene nanoparticle from aqueous solution to $[C_8C_1Im][NTf_2]$ (blue: non-polar; red: polar; yellow: polyethylene; grey: water; for the definitions, see Figure 5.2).

on its surface due to natural oxidation processes, at this point in the extraction process the PNP surface could act as a perfect template for the IL, and could trigger changes in the surface structure that are ideal for the stabilization and phase transfer of the plastic. Thus, the polar functional groups of the oxidized PNP could be solvated by the polar domain, while the non-polar groups could exploit the presence of the non-polar domain to facilitate the phase transfer. As the particle moves even closer to the IL (Figure 5.10),

the ions start to surround it, forming a micelle, even before the PNP would be fully submerged within the IL phase. This encompassed structure moves deeper into the IL, and while the surface starts to reorder to resemble the original structure, the polymer chains of the particle begin their disentanglement, as described above.

Due to the lack of microheterogeneity in $[C_2C_1Im][NTf_2]$, the interface does not exhibit the aforementioned structural features, and thereby the transfer of the PNP does not involve such severe reorientation of ions. The shorter side chain of the cation results in the partial mixing of the two phases, i.e., a higher water content in the ionic liquid phase. This finding is in good agreement with earlier experiments on the phase separation behavior of IL/water mixtures.[39]

The energetics of the process can also be estimated through the present simulations. The free energy profile does not show any barriers with either of the two ILs considered here (see Figure 7.8 in the appendix), which means that the phase transfer should not be kinetically hindered. This important result is in agreement with the structural changes observed above regarding the spontaneous reorientation of the IL ions at the interface upon the arrival of the PNP. In accordance with the findings above, which showed a more intensive IL-PNP interplay in case of longer side chains at the imidazolium cation, the phase transfer is significantly more exothermic for $[C_8C_1Im][NTf_2]$ as extractant ($-73$ kcal mol$^{-1}$) than for $[C_2C_1Im][NTf_2]$ ($-12$ kcal mol$^{-1}$).

## 5.4 Conclusion

In this study we suggest considering ionic liquids (ILs) as extractants for the removal of nanoplastics (PNPs) from aqueous solutions. By altering the length of the alkyl side chain length of the IL, or by changing the anions, the strength of the interactions between the solvent and the PNP can be tuned. The polymer chains of the plastic particle partially disentangle into a loosely associated structure, in order to increase the contact surface area with the solvent. However, as opposed to non-polar molecular solvents, the particle does not disintegrate into individual chains in most of the tetrafluoroborate and bis(trifluoromethylsulfonyl)imide ILs. The only exception was $[C_8C_1Im][NTf_2]$, showing

that by varying the side chain length and the anion, the stability of the particles, i.e. their disintegration can be controlled and adjusted to the given aims. We also demonstrated that due to the amphiphilic nature of ILs, the interfacial polar groups of partially oxidized nanoplastics can be also solvated by the suitable building blocks of the IL: The non-polar regions of the plastic can interact with the alkyl side chains, whereas the polar regions with the ionic head groups through hydrogen bonding. Accordingly, ILs should extract plastic nanoparticles (nanoplastics) with varying complex structures, which result from the interplay of these compounds with air, sunlight, and other environmental effects.

The interfacial microheterogeneous structure of $[C_8C_1Im][NTf_2]$ does not hinder the phase transfer. The layering of the interfacial region of the IL, presenting the polar regions of the extractant to the aqueous solution, is altered by the PNP. The cations at the interface flip, turning their alkyl chains towards the plastic in order to minimize unlike and maximize like interactions, resulting in a thermodynamically and kinetically favorable phase transfer. This reorientation also shows that if the surface plastic would be decorated with polar substituents or substances — through adsorption or oxidation processes — the IL surface could adjust to their presence as to a template, that both polar and non-polar functionalities could benefit from the interaction with the extractant ions. The IL ions were observed to create a micelle around the PNP at the water/IL interface, stabilizing the plastic even before the phase transition is completed. These results clearly indicate that employing ILs can indeed lead to promising processes to handle nanoplastic contamination where it is most necessary.

## Acknowledgements

RE and SG acknowledge the BMBF under the LuCaMag project 03EK3051A for financial support.

# 6 Summary and outlook

For this thesis, computational studies were carried out on ionic liquids (ILs), salts that are liquid at ambient temperatures and, thus, consist of mobile ions, in order to investigate structural features of these solvents relevant to their use as reaction media for the material synthesis as well as to their use as extractants. Much emphasis was placed on understanding the microheterogeneous structure forming in ILs, i.e. the segregation of polar and non-polar domains on the molecular level, and its impact and effects on the solvation of different molecules, as well as its potential to function as structure-directing or templating agent. In particular, the introduction of hydrophobic units in form of alkyl groups of different lengths leads to a tunability of the microheterogeneous behavior of the IL and thus makes them interesting candidates as potential reaction media and extractants.

Even though ILs have already been successfully used for both mentioned applications, and could thereby even improve the according processes especially in terms of resource-efficiency and sustainability, the drastic variations of properties based on the complexity of inter-ionic interactions within ILs demands for further fundamental investigations of their structure-property correlations, in order to achieve a more directed inset of ILs for an even broader range of applications. For this purpose, a combination of state-of-the-art classical molecular dynamics (MD) simulations, ab initio molecular dynamics (AIMD) simulations and static quantum chemical calculations, together with appropriate analysis tools that are capable of capturing the complex structural effects and allow for their quantification, were conducted in this thesis. Given the relevance of these investigations, it is believed that the findings reported herein will contribute to the general molecular level understanding of ILs.

From carrying out an exhaustive theoretical study on a $Te_4Br_2$ molecule dissolved in two different ionic liquids, 1-ethyl-3-methylimidazolium chloride ($[C_2C_1Im][Cl]$, system **A**) and 1-ethyl-3-methylimidazolium chloride mixed with aluminum chloride

($[C_2C_1Im][Cl]\cdot 1.3AlCl_3$, system **B**), it was achieved to elucidate the IL's degree of microheterogeneity and the role of $AlCl_3$, their effects on the solvent structure and the solvation of the $Te_4Br_2$ molecule, as well as the first steps of the reaction of the $Te_4Br_2$ molecule to eventually form the desired $Te_2Br$ material.

Even though it was expected to detect no noteworthy microheterogeneity, the short ethyl side chains attached to the imidazolium cations led to the formation of a microheterogeneous structure within system **A**, i.e., dispersed nonpolar units within the connected, three-dimensional polar network, which can be traced back to the smaller anions as compared to system **B**. In system **B**, in contrast, it was observed that the $AlCl_3$ forms larger anionic species, exceeding the size of simple chloride anions by far. Apart from a few "free" chloride atoms, 89.4% $Al_1$ ($AlCl_3$ and $AlCl_4^-$) clusters, 8.5% $Al_2$ ($Al_2Cl_7^-$) and 2.1% $Al_3$ ($Al_3Cl_{10}^-$) clusters were found.

For the $Te_4Br_2$ molecule dissolved in both ILs, significant Te-Br-bond elongations compared to gas-phase simulations were detected, inferring a solvation effect of the IL and a tendency towards the formation of a more ionic Te-Br species. However, while in system **A** the $Te_4Br_2$ molecule stretches slightly but does not undergo any structural change, only in system **B** a rearrangement occurs due to a bromide abstraction by a former anionic Al-species, which changes into an $AlCl_3$ species before the abstraction. After the abstraction, the $Te_4Br_2$ molecule is converted from an open form into a charged square-like species. The second Br remains at the $[Te_4]^{2+}$, but jumps between two Te atoms. Overall, these findings are in accordance with the proposed reaction mechanism for the formation of tellurium polycations in Lewis-acidic media via halide abstraction and subsequent redox reaction or rearrangement.

Moreover, the described reaction and rearrangement affect the solvation of the remaining $Te_4Br^+$ ion in the liquid. With the separated $Br^-$ species being strongly bound within an $AlCl_3Br^-$ anion, the Br atom of the $Te_4Br^+$ cation now perceives the presence of the neighboring Cl atoms. Due to the increased microheterogeneity in system **A**, the Br atoms of the $Te_4Br_2$ molecule are much more solvated by the terminal carbon atoms, i.e., the nonpolar units in this liquid, as compared to system **B**. This opens the possibility for a structure-directing effect, caused by the nonpolar groups.

As an extension to this study it would be interesting to execute further simulations for ILs with longer side chains, like for example $[C_xC_1Im][Cl]$ with x = 4, 6, 8, in order to receive a better understanding of the influence of increasing microheterogeneity on the solvation of the $Te_4Br_2$ molecule and its reactivity. Additionally, considering tellurium bromide particles or clusters of different sizes could potentially yield more information about the real crystallization behavior to eventually form the $Te_2Br$ material.

For investigating a possible structure-directing or template effect emanating from the microheterogeneous structure of ionic liquids in more detail, a systematic study was conducted using simple model systems. Two alcohols, *n*-butanol and *n*-dodecanol, were dissolved in 1-alkyl-3-methylimidazolium bis(trifluoromethylsulfonyl)imide ILs, varying the alkyl side chains from ethyl to butyl, hexyl and octyl groups ($[C_xC_1Im][NTf_2]$ with x = 2, 4, 6, 8). All types of analyses performed, starting from a purely visual inspection of selected simulation snapshots, carrying out a domain analysis and calculating spatial and combined distribution functions, showed an increasing segregation of the nonpolar from polar moieties of the IL as the side chain became longer. Moreover, a clear tendency was detected that within this microheterogeneous structure the IL cations order in a specific, parallel way, providing a direct proof for the qualitative description of microheterogeneous ILs being similar to surfactants in forming a non-spherical micelle-like structure.

Taking into account the alcohol molecules, it was observed that these tend to aggregate in the ILs with shorter side chains, while they show an increasing degree of dispersion in the liquid upon moving towards the ILs possessing longer alkyl tails. Interestingly, next to their association, the orientation of the alcohol molecules changes as well with the different degrees of microheterogeneity in the liquid, meaning that the increasing order within the ILs comprising longer side chains is imprinted in their alignment in the liquid. In particular, the alkyl chain of the alcohol stretches out parallel to the alkyl groups of the IL cations, while the polar part of the alcohol molecule mostly anchors to the polar network of the IL through strong polar-polar interactions. This behavior changes in degree, but does not dissipate when exchanging *n*-dodecanol for *n*-butanol, despite the shorter side chain. Instead, the arrangement of the alcohol molecules is primarily determined by the structure of the IL itself, indicating an unambiguous template effect

of the ionic liquid on the solutes in it.

The observed structure-directing effect from the IL to the solute molecules offers great potential for practical applications. By the simple change of the solvent, it is possible to manipulate the orientation of, for example, a reactant, i.e., forcing it to assume a certain conformation or collide in the solution in a certain manner, which can enhance some chemical processes in the liquid, while suppressing others, potentially leading to the formation of new products. Thereby, carrying out molecular dynamics simulations and subsequently performing suitable analyses, will not only help to interpret regioselectivities of reactions in ILs that have already been explored experimentally, but it will also enable the consciously design of solvent systems for reactions with the aim to reach higher selectivities. In that regard, stereoselectivity and chirality are also highly interesting topics, since the introduction of chiral microheterogeneous ILs, which are capable of acting as template, might increase the efficiency of the synthesis of the desired products. Moreover, it is thinkable that the mesoscopic structure of the liquid can be imprinted directly into the morphology of different compounds, like inorganic materials or (organic) polymers, potentially resulting in products with completely new properties.

The amphipilic nature of distinct or accordingly functionalized ionic liquids that leads to the formation of a microheterogeneous structure can as well make these solvents sufficiently hydrophobic for extracting substances from an aqueous medium. This opens the perspective for considering ILs as extractants for the removal of plastic nanoplastics (PNPs) from aqueous solutions. This task represents none less than one of the most severe and concerning problems of our time, which clearly highlights the enormous motivation to study this subject in more detail.

To do so, the solvation of pristine and oxidized polyethylene nanoparticles (composed of 16 coiled $C_{72}H_{144}$ chains) was characterized in sets of the ionic liquids 1-alkyl-3-methylimidazolium bis(trifluoromethylsulfonyl)imide and 1-alkyl-3-methylimidazolium tetrafluoroborate ($[C_xC_1Im][NTf_2]$ with x = 2, 4, 6, 8 and $[C_xC_1Im][BF_4]$ with x = 2, 8), and compared to molecular solvents with different polarity, i.e., saline water, ethanol, tetrahydrofuran and toluene. Subsequently, an extraction process was modeled by simulating the phase transfer of a polyethylene nanoparticle from a saline water phase to an

IL phase (at the examples of $[C_2C_1Im]$- and $[C_8C_1Im][NTf_2]$).

In case of the molecular solvents it was found that depending on the degree of polarity (from polar to nonpolar: saline water > ethanol > tetrahydrofuran > toluene), the PNP behaves quite differently. In the two polar solvents, saline water and ethanol, the polymer chains stay aggregated, but an increased surface area in the latter solvent indicates a loss of their compact structure in order to expose more of the polymers to the solvent. In the two nonpolar solvents, tetrahydrofuran and toluene, a dissociation of the PNP particle into separate chains was observed, with the effect being significantly stronger in the case of toluene.

Turning to the ionic liquids, it was observed that by altering the length of the alkyl side chain of the IL, or by changing the anion, the strength of the interactions between the solvent and the PNP can be tuned. In general, the pristine plastic particle tends to disentangle into a loosely associated structure, in order to increase the contact surface area with the solvent. However, in contrast to nonpolar molecular solvents, tetrahydrofuran and toluene, the particle does not disintegrate into individual chains in most of the tetrafluoroborate and bis(trifluoromethylsulfonyl)imide ILs. The only exception is $[C_8C_1Im][NTf_2]$, showing that by varying the side chain length and the anion, the stability of the particles, i.e. their disintegration can be controlled and adjusted.

In case of the partially oxidized nanoplastics, which were modeled to take into account the natural interplay of these compounds with air, sunlight, and other environmental effects, it was demonstrated that due to the amphiphilic nature of ILs, the interfacial polar groups of the particles can be solvated by suitable building blocks of the IL as well: the nonpolar regions of the plastic interact with the alkyl side chains attached to the cations, whereas the polar units orient towards the cationic head groups and anions through hydrogen bonding. This indicated that ILs should be capable of extracting PNPs with varying complex structures.

The simulation of an extraction process showed that the interfacial microheterogeneous structure of $[C_8C_1Im][NTf_2]$ does not hinder the phase transfer. Within the extraction process, the layering of the IL's interfacial region, which initially presents their polar entities to the aqueous solution, is altered by the PNP. As the particle approaches, the

cations at the interface flip, turning their alkyl chains towards the plastic in order to minimize unlike and maximize alike interactions, resulting in a thermodynamically and kinetically favorable phase transfer. Due to the shorter ethyl side chain this effect is much weaker, but still favorable for $[C_2C_1Im][NTf_2]$ ($-73$ kcal mol$^{-1}$ for $C_8$ vs. $-12$ kcal mol$^{-1}$ for $C_2$). The reorientation of the IL additionally indicates that if the plastic surface was decorated with polar substituents or substances — through oxidation or adsorption processes — the IL surface could adjust to their presence as to a template, so that both polar and nonpolar functionalities could benefit from the interaction with the extractant ions. In the course of the phase transfer, the IL ions were further observed to create a micelle around the PNP at the water/IL interface, stabilizing the plastic even before the phase transition is completed. Lastly, this encompassed structure moves deeper into the IL, and while the surface starts to reorder to resemble the original structure, the polymer chains of the particle begin their disentanglement, as described above. These results clearly indicate that employing ILs can indeed lead to promising processes to handle nanoplastic contamination where it is most necessary.

In summary, the results presented in this thesis aim to further elucidate the special structural properties of ionic liquids and to offer guidance for the tunability of these structural features for their application-oriented adjustment. State-of-the-art ab initio and classical molecular dynamics simulations were employed in combination with selected and suitable analysis tools to provide a general molecular-level understanding of the underlying diverse interactions governing these solvents and determining their structural properties. With this contribution it is envisaged and hoped to help guiding the rational and systematic design of novel IL-based solvents and to motivate further comprehensive investigations on the structural properties of ILs, so that new strategies can be conceived and established to counteract the global climate change and to preserve the world's oceans. Drop by drop.

# 7 Appendix

## 7.1 Further simulation details

### 7.1.1 Ensembles and temperature-control

Seen from the statistical physics point of view, an MD simulation produces different microscopic configurations of the simulated system, which possess identical macroscopic and thermodynamic properties if they are in statistical equilibrium. The collection of these different microscopic states is denoted as thermodynamic ensemble. Based on this, it is possible to derive different thermodynamic properties of the systems as ensemble averages by applying the laws of classical or quantum mechanics. It can be distinguished between the following thermodynamic ensembles:

- Microcanolical ensemble (NVE): describes a closed system with a constant number of particles $N$, a constant volume $V$ and a constant inner energy $E$.
- Canonical ensemble (NVT): describes a closed system with a constant number of particles $N$, a constant volume $V$ and a constant temperature $T$.
- Macrocanonical ensemble ($\mu$VT): describes an open system with a constant chemical potential $\mu$, a constant volume $V$ and a constant temperature $T$.
- Isothermal–isobaric ensemble (NPT): describes a closed system with a constant number of particles $N$, a constant pressure $P$ and a constant temperature $T$.

Depending on the choice of the ensemble, the interactions between a system and its environment are determined.

Since MD simulations based on the Newtonian equation of motion conserve the total energy of a system, a trajectory in the microcanolical (NVE) ensemble is generated.

For the comparison with experimental data, however, where usually the temperature is controlled, simulations in the canonical (NVT) ensemble might be desired. For this purpose, a thermostat is applied, for which the Nosé-Hoover thermostat represents the probably most common choice.[211,212,291] Here, a heat bath is added to the simulation, which introduces an additional degree of freedom to the system. For the heat bath, an additional potential is used, so that the original degrees of freedom still sample the NVT ensemble. To handle more complex systems, later this concept has been extended to the Nosé-Hoover thermostat chain,[292] where the initial heat bath is coupled to another heat bath.

### 7.1.2 Starting conditions and system equilibration

For solving the Newtonian equation of motion, first a staring configuration (at time $t = 0$) of the system to be simulated has to be defined. For this purpose the particles are usually placed on lattice points of a regular three-dimensional lattice, because a random distribution could lead to “hot spots”, so configurations, where two or more atoms are too close to each other, leading to unfavorable energies. The creation of this starting geometry can be carried out, for example, by using the program PACKMOL.[208,209] The only requirements are the structures of one molecule of each type and the dimensions of the resulting simulation box. Depending on the number of molecules to be simulated, it is advisable to select the box dimensions according to the experimental density of the system (if available), so that the system is already as close as possible to the ”real“ system.

Even though PACKMOL guarantees reasonable starting geometries for the subsequent simulation, these geometries are usually still far from an equilibrated state of the system. Thus, it is common to perform a previous equilibration run until the system is sufficiently equilibrated. Of course, the length of this equilibration run depends on the system, but a common ”trick“ to reduce its duration is to increase the temperature and thus the dynamics in the system. Moreover, in case of an AIMD simulation, it is convenient to apply an individual Nosé-Hoover thermostat chain to each degree of freedom in the system, which is denoted as *massive thermostat* and helps to excite even stiff vibrations, thus, reducing the equilibration time significantly. In order to monitor whether a system is equilibrated

or not, usually certain system properties are evaluated regularly, and the system is considered to be equilibrated if these properties become stable, i.e., their oscillations over time become tolerably small or vanish at all. Appropriate properties for monitoring are, e.g., thermodynamic properties, like the total energy, temperature and pressure, or structural properties, like the order parameter and the mean square displacement. After the equilibration run the actual production run is started, which is used to subsequently evaluate the desired system properties.

### 7.1.3 Periodic boundary conditions

In order to be able to calculate macroscopic properties of bulk-systems, like liquids, but at the same time reduce the number of particles and thus, the computational effort required as much as possible, MD simulations are usually performed under periodic boundary conditions (PBCs). Here, the initial simulation box is surrounded by identical copies of itself, so that there are no direct boundaries anymore. If one particle leaves the initial box in the course of the simulation, another identical particle enters the box from the exact opposite side of the simulation box. In this way, the number of particles remains conserved over time. Depending on the system to be simulated, the simulation box can have different shapes, the most common shape is cubic, but orthorombic, or other shapes are possible as well, as long as the translation operation can fill the whole space without any voids.

## 7.2 Supporting information to chapter 4

### 7.2.1 Investigated systems

**Table 7.1** Model systems composed of different ILs $[C_xC_1Im][NTf_2]$ mixed together with alcohols $H_{2y+1}C_yOH$, investigated by classical simulations. In each case, 250 ion pairs of the IL and 50 alcohol molecules were taken into consideration. In the course of the simulations adjusted box constants $a$ and densities $\rho$ are shown.

| IL | ALC | $a$/ | $\rho$/ |
|---|---|---|---|
| x = | y = | pm | g cm$^{-3}$ |
| 2 | 12 | 5118.85 | 1.326415 |
| 4 | 12 | 5308.72 | 1.266983 |
| 6 | 12 | 5481.96 | 1.221330 |
| 8 | 12 | 5646.63 | 1.182265 |
| 2 | 4 | 4961.60 | 1.380274 |
| 4 | 4 | 5160.02 | 1.311876 |
| 6 | 4 | 5347.11 | 1.255128 |
| 8 | 4 | 5513.22 | 1.214575 |

### 7.2.2 Simulation details

For the description of the IL cations and anions intra- and intermolecular interactions the force field parameters were chosen according to Canongia Lopes and Pádua, who developed the parameters based on the OPLS-AA/AMBER framework and on the OPLS-AA model, which is oriented towards the calculation of equilibrium thermodynamic and structural properties.[59,60] The charges of the cations and anions were scaled by a factor of 0.8 since this has shown a more reasonable representation of mass transport properties of ILs. The parameters for the alcohol molecules were chosen according to Jorgensen et al., which are based on the OPLS-AA model as well and serve to describe the interactions of organic molecules and peptides.[142]

In order to obtain Lennard-Jones cross terms, the Lorentz-Berthelot mixing rules were

applied.[136,311] All non-bonded interactions between the atoms were restricted to a cutoff radius of 16 Å.

The components of the systems presented in Table 7.1 were built using the software package MOLDEN (version 5.4).[312] The initial start geometries of the simulation boxes were generated with the aid of the program PACKMOL (version 16.228).[208,209] Each system was simulated under periodic boundary conditions in order to avoid border/edge effects using the molecular dynamics simulator LAMMPS (version from the 14$^{\text{th}}$ May 2016).[144] The simulations were performed at a temperature of 400 K and a pressure of 1 bar, which was controlled by applying the Nosé–Hoover chain thermostat and the Nosé–Hoover barostat, respectively, using a time step of 0.5 fs.[211,291,292] The simulation runs were composed of eight steps, which are described briefly in the following:

1. Energy minimization of the whole system by adjusting the atom coordinates iteratively. Here, a tolerance for the energy and the forces of 1.0e$^{-4}$ and 1.0e$^{-6}$, respectively, was used with maximum 500 iterations of the minimizer and maximum 5000 energy/force evaluations.

2. Deformation of the simulation box over 300000 steps in the NVE ensemble to adjust the starting geometry of the system to an initial density calculated according to a new group contribution method for pure ILs at different temperatures.[313]

3. Pre-equilibration of the system over another 300000 steps in the NVE ensemble with the previous adjusted density.

4. Relaxation of the system over 500000 steps in the NPT ensemble to correct the density and derive the theoretical density.

5. Another 500000 steps in the NPT ensemble over which the box volume is averaged to yield the final theoretical density.

6. Short run over 10000 steps in the NVT ensemble to adjust the simulation box to the averaged box volume and final theoretical density.

7. Equilibration of the system over 3000000 steps in the NVT ensemble.

8. Production run: First 9900000 steps printing out the atoms coordinates every 1000$^{th}$ step for the investigation of structural properties (long trajectory), second further 100000 steps printing out the atoms coordinates every step for the investigation of dynamic properties (short trajectory).

### 7.2.3 Spatial distribution functions

**Table 7.2** Isovalue ranges ($I_{min}$ - $I_{max}$) and chosen isovalues $I$ for SDFs isosurfaces. In case of the $[C_8C_1Im]^+$ cation, 90.58 % from the upper limit of the ranges for each subset were taken as final isovalue, while for the alcohol in both $[C_8C_1Im][NTf_2]$ and $[C_2C_1Im][NTf_2]$, 90.86 % were chosen.

| | $[C_8C_1Im]^+$ ($[C_8C_1Im][NTf_2]$) | | | *n*-dodecanol ($[C_8C_1Im][NTf_2]$) | | | *n*-dodecanol ($[C_2C_1Im][NTf_2]$) | | |
|---|---|---|---|---|---|---|---|---|---|
| Color | $I_{min}$ | $I_{max}$ | $I$ | $I_{min}$ | $I_{max}$ | $I$ | $I_{min}$ | $I_{max}$ | $I$ |
| red | $2.13 \cdot 10^{-6}$ | 1.98 | 1.79 | $1.18 \cdot 10^{-6}$ | 2.66 | 2.42 | 0 | 3.17 | 2.88 |
| orange | $5.51 \cdot 10^{-6}$ | 3.15 | 2.86 | 0 | 2.01 | 1.83 | 0 | 2.81 | 2.56 |
| green | $1.24 \cdot 10^{-5}$ | 1.94 | 1.76 | $1.17 \cdot 10^{-7}$ | 1.60 | 1.45 | 0 | 2.72 | 2.47 |
| blue | $2.74 \cdot 10^{-6}$ | 0.42 | 0.38 | $5.04 \cdot 10^{-8}$ | 0.44 | 0.40 | 0 | 0.59 | 0.54 |
| yellow | $3.53 \cdot 10^{-6}$ | 0.41 | 0.37 | $2.72 \cdot 10^{-6}$ | 1.11 | 1.00 | 0 | 1.27 | 1.16 |

The spatial distribution functions (SDFs) represent the three-dimensional density distribution of the previously defined subsets around a given reference molecule and are therefore used to study details of the spatial structure of either the ILs cation or the alcohol within the mixture. In the case of the $[C_8C_1Im]^+$ cation, the reference plane was built considering the nitrogen atom carrying the octyl side chain as origin, locating the terminal carbon atom of the octyl chain on the x-axis and the carbon atom between the two nitrogen atoms of the imidazolium ring on the x-y-plane, while for the *n*-dodecanol molecule, the oxygen atom represented the origin, the carbon atom bound to the oxygen atom was located on the x-axis and one of the hydrogen atoms bound to the aforementioned carbon atom was placed on the x-y-plane. The colors were chosen according to the colors for the subsets defined for the snapshots, only the cationic head group and the anion are distinct now: P-IL (Cat), red; P-IL (An), orange; N-IL, green; P-A, yellow;

N-A, blue. The visualization of the density distribution of a particular subset around a molecule can be achieved by generating isosurfaces with the aid of the program VMD.[165] Here, the extend of the isosurface can be controlled by the so-called isovalue, which has to lie within a certain range. In general a high isovalue leads to an isosurface considering only the density distribution of a subset very close to the observed molecule, while a value approaching zero considers the density within the whole simulation box. The range is dependent on the number of molecules and atoms contributing to the density distribution, which is why for the alcohol subsets the range is significantly smaller than for the IL subsets. To nevertheless reach a comparable density representation, for each subset we considered the same percentage from the upper value limit of each range (cf. Table 7.2).

### 7.2.4 Domain analysis

Next to the domain count and averaged percentual surface coverages described in section 2, the domain analysis also yields information about the domain volume and surface, as well as the isoperimetric quotient, presented in Table 7.3 and Table 7.4. The isoperimetric quotient provides a measure of the deviation of the domains from a spherical shape. If a domain has the shape of a sphere, its isoperimetric quotient will be 1; otherwise, it will be smaller than 1. A deviation from unity describes the asphericity of the domain.

### 7.2.5 Angular distribution functions

Figure 7.1 shows the angular distribution functions (ADFs) for the alkyl side chains attached to the ILs cations (left plots) and for the cation's side chains and the alkyl chains of the alcohols (right plots) for the systems containing *n*-dodecanol (upper plots) and *n*-butanol (lower plots) for the different ILs. The ADFs were calculated only considering distances within the first solvation shells (between 0 and 800 pm, cf. first minimum of RDFs in Figure 7.2).

**Table 7.3** Domain analysis and surface coverage from Voronoi analysis for different ILs $[C_xC_1Im][NTf_2]$ mixed together with alcohols $H_{2y+1}C_yOH$. The isoperimetric quotients $Q^{iper}$, domain sizes and surface coverages emanating from the different subsets P and N are shown.

| IL | ALC | $Q^{iper}$ | | P size | | N size | |
|---|---|---|---|---|---|---|---|
| x = | y = | P | N | $V/Å^3$ | $A/Å^2$ | $V/Å^3$ | $A/Å^2$ |
| 2 | 12 | 0.06 | 0.42 | 106378 | 27660 | 562 | 561 |
| 4 | 12 | 0.03 | 0.28 | 106205 | 36167 | 9510 | 8006 |
| 6 | 12 | 0.02 | 0.04 | 105715 | 40977 | 45062 | 32001 |
| 8 | 12 | 0.02 | 0.01 | 102334 | 42673 | 69762 | 42264 |
| 2 | 4 | 0.11 | 0.36 | 106125 | 22345 | 198 | 277 |
| 4 | 4 | 0.04 | 0.31 | 106235 | 32420 | 4656 | 4844 |
| 6 | 4 | 0.02 | 0.07 | 106549 | 38390 | 31092 | 25779 |
| 8 | 4 | 0.02 | 0.02 | 105985 | 42226 | 54366 | 37643 |

| IL | ALC | P coverage | | N coverage | |
|---|---|---|---|---|---|
| x = | y = | P | N | P | N |
| 2 | 12 | 73.5 | 26.5 | 75.8 | 24.2 |
| 4 | 12 | 66.3 | 33.7 | 68.1 | 31.9 |
| 6 | 12 | 62.1 | 37.9 | 62.1 | 37.9 |
| 8 | 12 | 59.4 | 40.6 | 55.8 | 44.2 |
| 2 | 4 | 78.3 | 21.7 | 87.9 | 12.1 |
| 4 | 4 | 69.9 | 30.1 | 80.5 | 19.5 |
| 6 | 4 | 64.8 | 35.2 | 71.6 | 28.4 |
| 8 | 4 | 61.3 | 38.7 | 64.5 | 35.5 |

### 7.2.6 Radial distribution functions and number integrals

To characterize the typical structural motives within the systems, radial distribution functions (RDFs) and number integrals (NIs) are calculated and discussed in the following.

Figure 7.2 shows the radial distribution functions (RDFs) and number integrals (NIs) for selected relevant distances, namely between the terminal carbon atoms of the alkyl side chains attached to the cations ($C_{term}$ (Cat) - $C_{term}$ (Cat), left plots) and between

**Table 7.4** Domain analysis for different ILs $[C_xC_1Im][NTf_2]$ mixed together with alcohols $H_{2y+1}C_yOH$. The isoperimetric quotients $Q^{iper}$ and the domain sizes emanating from the different subsets P, N, P-IL, N-IL, P-A and N-A are shown.

| IL | ALC | $Q^{iper}$ | | | |
|---|---|---|---|---|---|
| x = | y = | P-IL | N-IL | P-A | N-A |
| 2 | 12 | 0.05 | 0.42 | 0.49 | 0.23 |
| 4 | 12 | 0.03 | 0.30 | 0.49 | 0.23 |
| 6 | 12 | 0.02 | 0.24 | 0.49 | 0.25 |
| 8 | 12 | 0.01 | 0.04 | 0.49 | 0.25 |
| 2 | 4 | 0.09 | 0.40 | 0.48 | 0.40 |
| 4 | 4 | 0.03 | 0.31 | 0.49 | 0.42 |
| 6 | 4 | 0.02 | 0.16 | 0.49 | 0.42 |
| 8 | 4 | 0.02 | 0.02 | 0.50 | 0.43 |

| IL | ALC | P-IL size | | N-IL size | | P-A size | | N-A size | |
|---|---|---|---|---|---|---|---|---|---|
| x = | y = | $V/Å^3$ | $A/Å^2$ | $V/Å^3$ | $A/Å^2$ | $V/Å^3$ | $A/Å^2$ | $V/Å^3$ | $A/Å^2$ |
| 2 | 12 | 103653 | 28187 | 80 | 126 | 68 | 104 | 2526 | 1985 |
| 4 | 12 | 103743 | 36336 | 928 | 1027 | 68 | 103 | 1852 | 1471 |
| 6 | 12 | 103788 | 41127 | 10442 | 9196 | 67 | 102 | 1507 | 1226 |
| 8 | 12 | 103850 | 44062 | 42507 | 31394 | 68 | 103 | 1397 | 1147 |
| 2 | 4 | 103382 | 23383 | 86 | 136 | 69 | 105 | 166 | 206 |
| 4 | 4 | 103472 | 32996 | 1397 | 1529 | 66 | 102 | 152 | 190 |
| 6 | 4 | 103778 | 38568 | 17876 | 15369 | 68 | 103 | 157 | 195 |
| 8 | 4 | 103569 | 42275 | 49056 | 35094 | 66 | 101 | 148 | 184 |

the terminal carbon atoms of the alcohols and the terminal carbon atoms of the cations ($C_{term}$ (Alc) - $C_{term}$ (Cat), right plots), for *n*-dodecanol (upper plots) and *n*-butanol (lower plots) in the different ILs.

For the $C_{term}$ (Cat) - $C_{term}$ (Cat) distances, the RDFs and NIs exhibit similar courses, indicating that independent of the size of the alcohols the $C_{term}$ (Cat) - $C_{term}$ (Cat) distances and their correlations are equal for the same ILs. In each case, the first maximum is located around 420 pm and shows a slow decrease until the first minimum, which is located between 700 and 750 pm for $[C_xC_1Im][NTf_2]$ with x = 4, 6 and 8 and

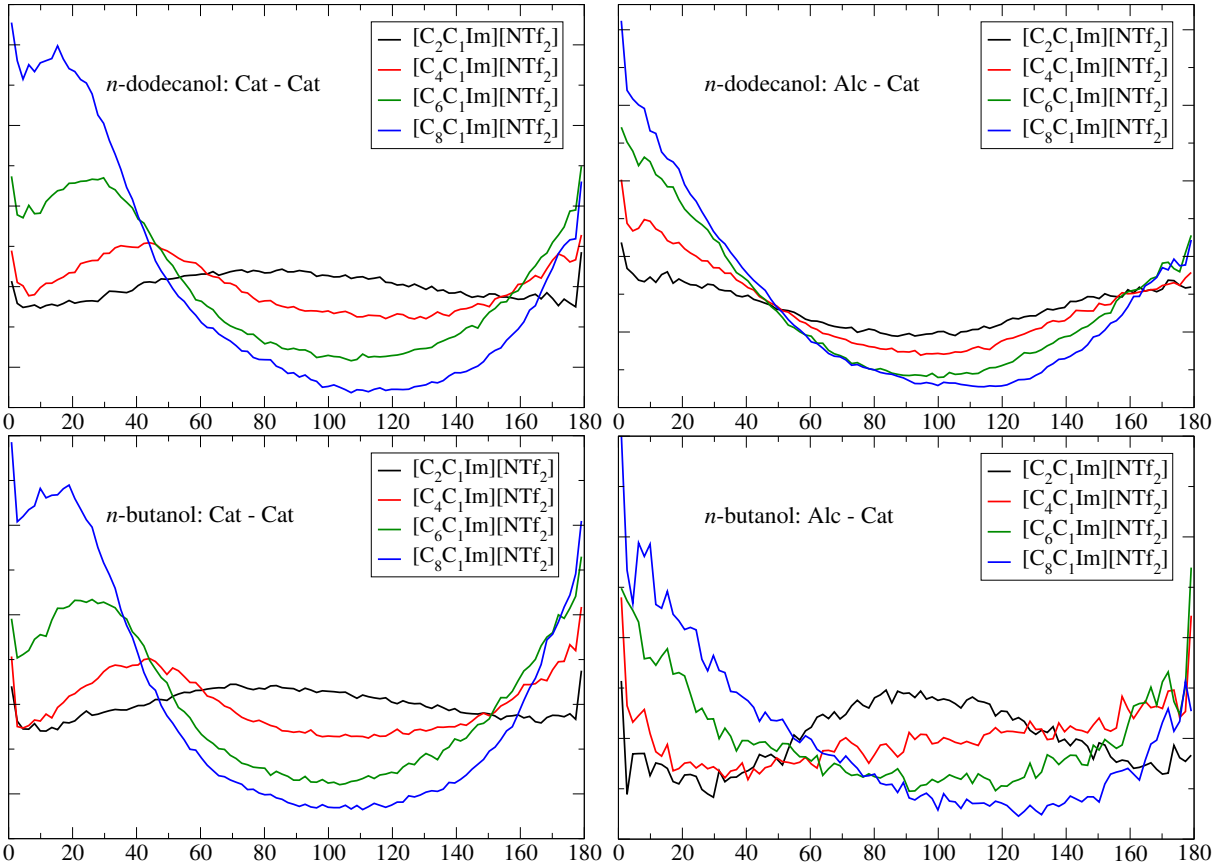


**Figure 7.1** ADFs between alkyl side chains for *n*-dodecanol (upper plots) and *n*-butanol (lower plots) in different ILs, using a distance criterion of 800 pm.

around 650 pm for $[C_2C_1Im][NTf_2]$. The correlations between the $C_{term}$ (Cat) atoms are strongest for $[C_8C_1Im][NTf_2]$ and decrease with decreasing size of the alkyl side chains. For $[C_2C_1Im][NTf_2]$ the first maximum even lies underneath g(r) = 1. The coordination numbers for the $C_{term}$ (Cat) atoms within their first solvation shells, resulting from the NIs at the particular RDFs minimum, amount for approximately 2.6 for $[C_8C_1Im][NTf_2]$, 2.3 for $[C_6C_1Im][NTf_2]$, 1.8 for $[C_4C_1Im][NTf_2]$ and 1.3 for $[C_2C_1Im][NTf_2]$. This indicates a stronger agglomeration behavior for the $C_{term}$ (Cat) atoms of the ILs with longer side chains.

A similar behavior can be observed for the $C_{term}$ (Alc) - $C_{term}$ (Cat) RDFs and NIs. The RDFs first maxima are located at approximately 420 pm and the curves show a slow decrease to the first minimum. The trend of an increasing correlation between the terminal carbon atoms with increasing chain length of the cations can be seen as well, even though, the differences are much smaller for the systems containing the short chain

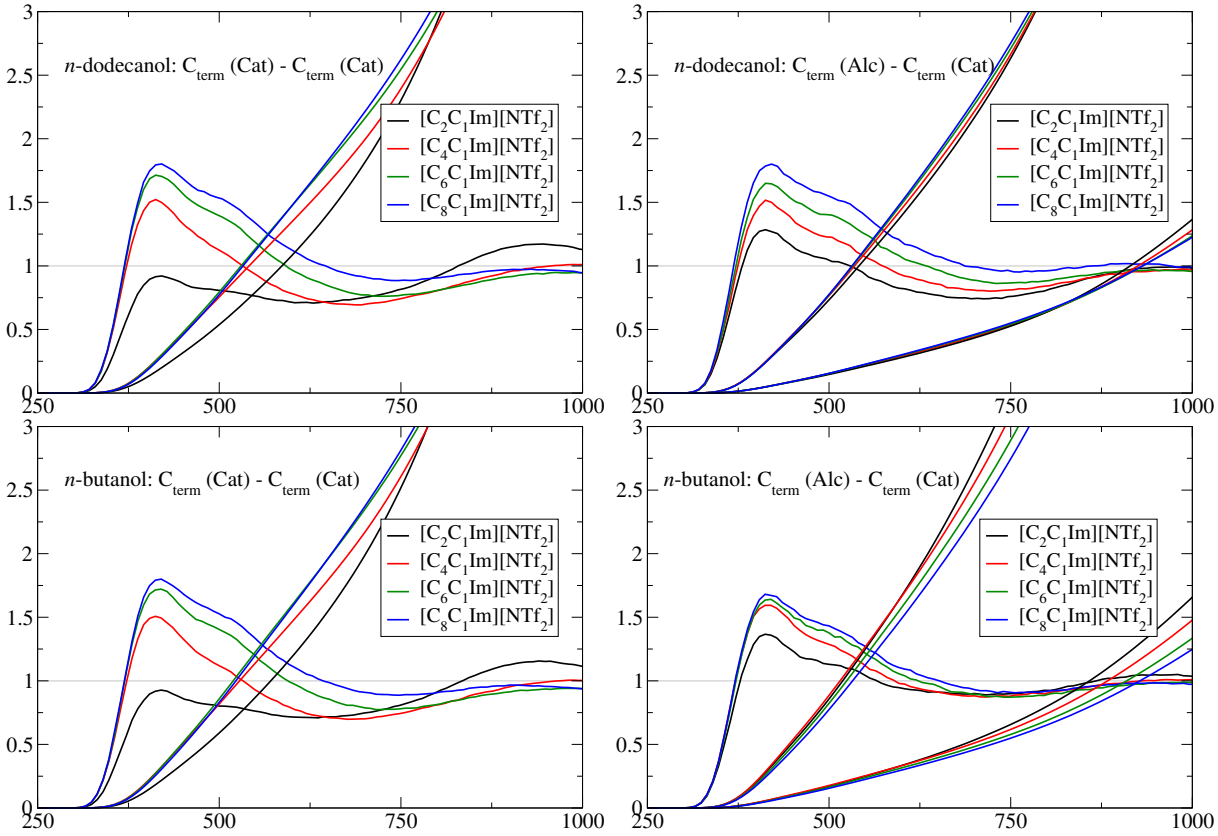


**Figure 7.2** RDFs and NIs between alkyl side chains for *n*-dodecanol (upper plots) and *n*-butanol (lower plots) in different ILs. For the right plots, the steeper NIs represent the distances defined from the terminal carbon atom of the alcohol $C_{term}$ (Alc) to the terminal carbon atom of the respective cation $C_{term}$ (Cat), while the more flat NIs represent the $C_{term}$ (Cat) $\rightarrow$ $C_{term}$ (Alc) distances.

alcohol *n*-butanol. This again indicates a stronger agglomeration behavior for longer side chains. The only differences arise from a stronger $C_{term}$ (Alc) - $C_{term}$ (Cat) correlation for $[C_2C_1Im][NTf_2]$, which show a first peak that lies above g(r) = 1. This is due to the fact that the alcohols are much more flexible than the rather short ethyl side chain of the $[C_2C_1Im]^+$ cation, allowing for an easier orientation of the polar and non-polar units of the molecules and therefore leading to an increased correlation. This of course also reflects in the NIs. For both alcohols, the steeper NIs represent the distances defined from $C_{term}$ (Alc) to $C_{term}$ (Cat) and the flat ones the distances from $C_{term}$ (Cat) to $C_{term}$ (Alc). This immediately indicates a higher coordination number of the $C_{term}$ (Cat) atoms around the $C_{term}$ (Alc) atoms than of the $C_{term}$ (Alc) atoms around the $C_{term}$ (Cat) atoms, which is simply due to the higher number of 250 cations in the systems compared

to only 50 alcohol molecules.

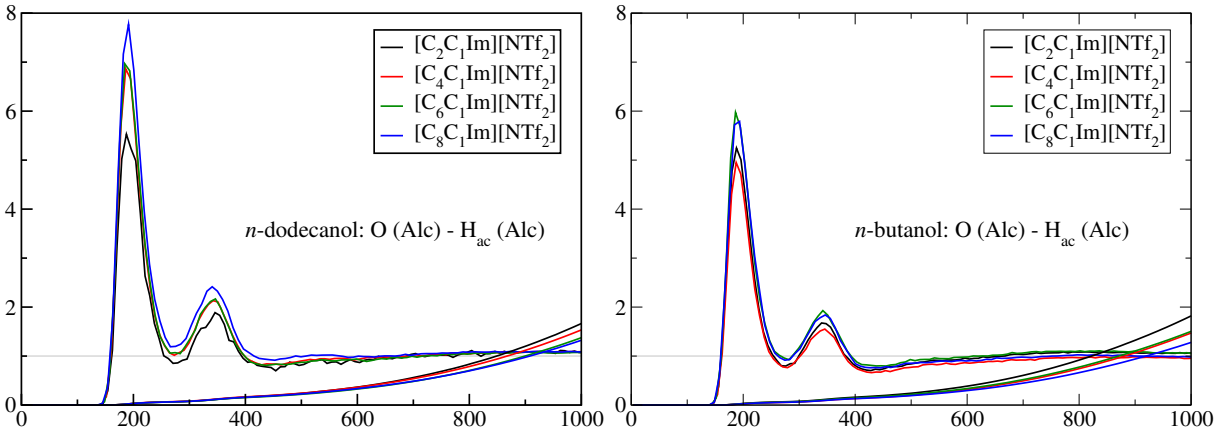


**Figure 7.3** RDFs and NIs for *n*-dodecanol (left) and *n*-butanol (right) in different ILs, showing hydrogen-bonding between the alcohol molecules.

In addition, Figure 7.3 shows the intermolecular RDFs and NIs for the alcohols oxygen atoms and acidic hydrogen atoms for *n*-dodecanol (left) and *n*-butanol (right) in the different ILs $[C_xC_1Im][NTf_2]$. In all cases a first sharp peak occurs at around 200 pm, indicating hydrogen bonding between the OH groups of the alcohol molecules.

# 7.3 Supporting information to chapter 5

## 7.3.1 Surface area development

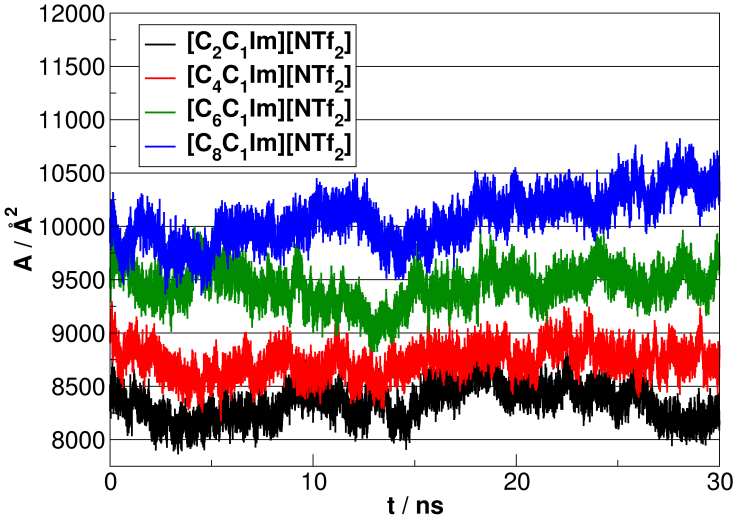


**Figure 7.4** Changes in the surface area $A$ of the PNP versus simulation time in $NTf_2$ ionic liquids, starting from the globular polyethylene PNP.

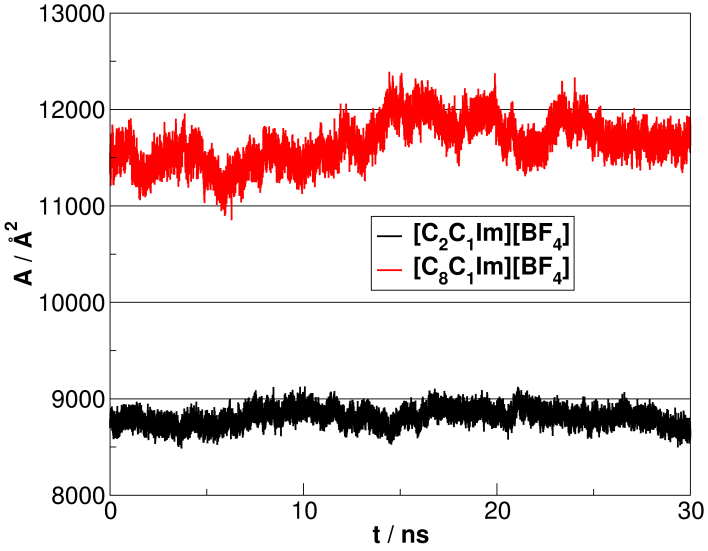


**Figure 7.5** Changes in the surface area $A$ of the PNP versus simulation time in $BF_4$ ionic liquids, starting from the globular polyethylene PNP.

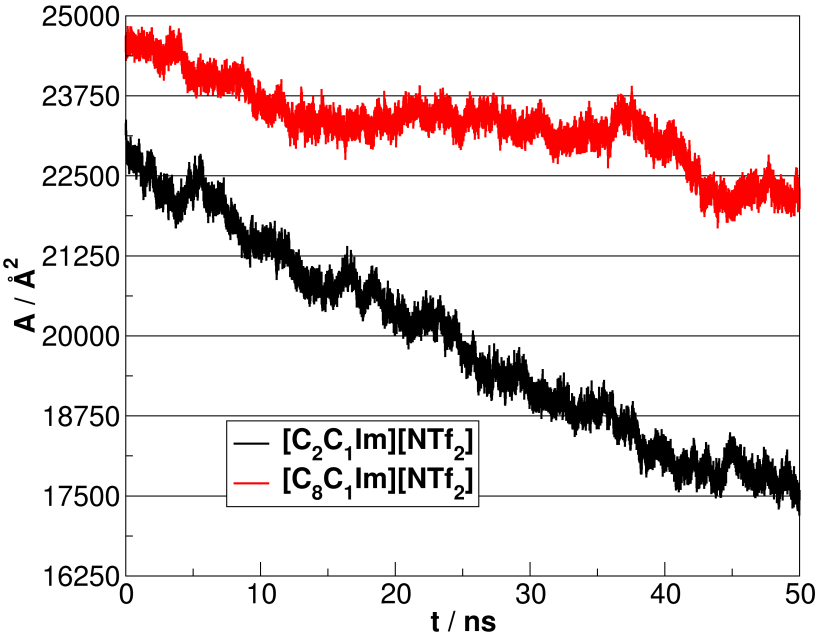


**Figure 7.6** Changes in the surface area $A$ of the PNP versus simulation time in $NTf_2$ ionic liquids, starting from the randomly distributed, dissociated chains.

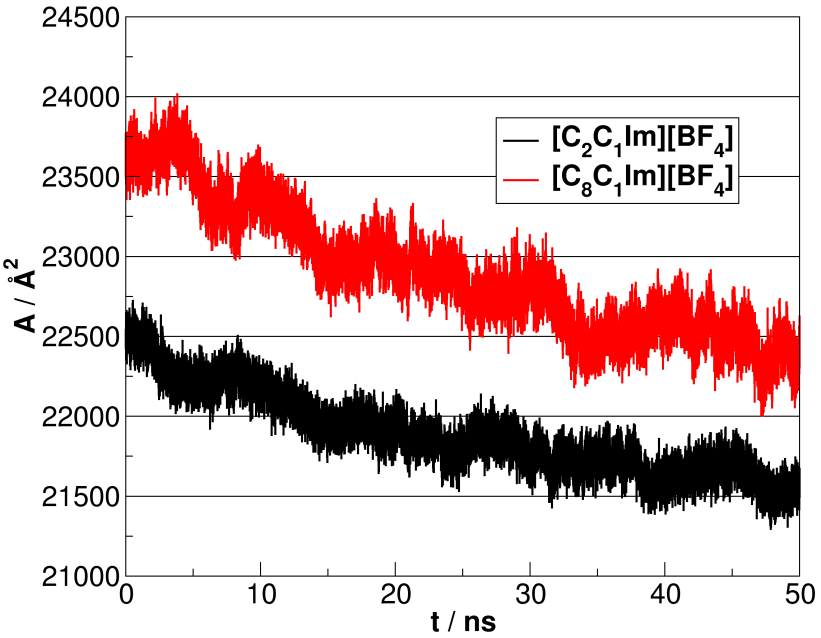


**Figure 7.7** Changes in the surface area $A$ of the PNP versus simulation time in $BF_4$ ionic liquids, starting from the randomly distributed, dissociated chains.

### 7.3.2 Free energy development

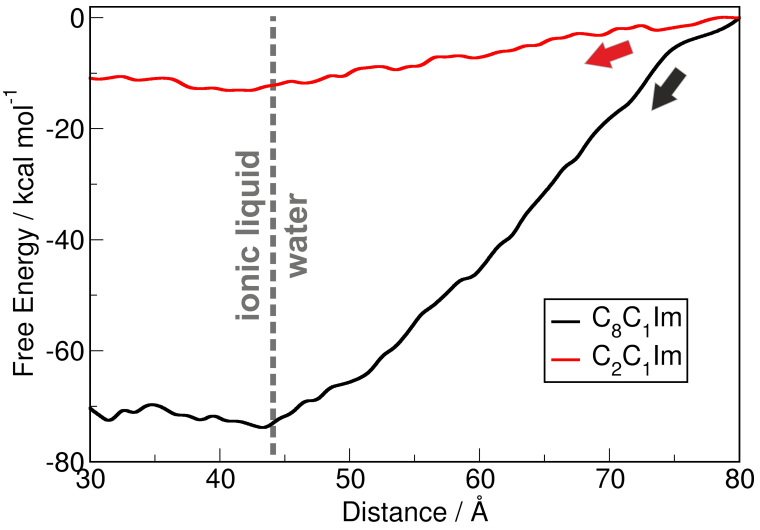


**Figure 7.8** Free energy curves of the phase transfer of the PNP particle from the aqueous phase (right) to the ionic liquid phase (left), obtained from umbrella sampling simulations. The particle was initially situated in the aqueous phase, and gradually moved toward the center of mass of the ionic liquid phase, across the liquid-liquid interface. The location of the particle is defined by the Z component of the distance vector connecting the center of mass of the plastic and that of the ionic liquid phase. The particle crosses the interface at a distance of ca. 44 Å.

# Bibliography


[1] United Nations - THE 17 GOALS - Sustainable Development. `https://sdgs.un.org/goals`, Accessed: 2021-03-25.

[2] Walden, P. *Bull. Acad. Imper. Sci.(St. Petersburg)* **1914**, *1800*, 405–422.

[3] Hurley, F. H.; Wier, T. P. *J. Electrochem. Soc.* **1951**, *98*, 207–212.

[4] Fry, S. E.; Pienta, N. J. *J. Am. Chem. Soc.* **1985**, *107*, 6399–6400.

[5] Boon, J. A.; Levisky, J. A.; Pflug, J. L.; Wilkes, J. S. *J. Org. Chem.* **1986**, *51*, 480–483.

[6] Earle, M. J.; Seddon, K. R. *Pure Appl. Chem.* **2000**, *72*, 1391–1398.

[7] Urahata, S. M.; Ribeiro, M. C. C. *J. Chem. Phys.* **2004**, *120*, 1855–1863.

[8] Wang, Y.; Voth, G. A. *J. Am. Chem. Soc.* **2005**, *127*, 12192–12193.

[9] Canongia Lopes, J. N.; Pádua, A. A. H. *J. Phys. Chem. B* **2006**, *110*, 3330–3335.

[10] Wang, Y.; Voth, G. A. *J. Phys. Chem. B* **2006**, *110*, 18601–18608.

[11] Triolo, A.; Russina, O.; Bleif, H.-J.; Di Cola, E. *J. Phys. Chem. B* **2007**, *111*, 4641–4644.

[12] Weber, H.; Hollóczki, O.; Pensado, A. S.; Kirchner, B. *J. Chem. Phys.* **2013**, *139*, 084502.

[13] Kirchner, B.; Hollóczki, O.; Canongia Lopes, J. N.; Pádua, A. A. H. *WIREs Comp. Mol. Sci.* **2014**, 202–214.

[14] Hollóczki, O.; Macchiagodena, M.; Weber, H.; Thomas, M.; Brehm, M.; Stark, A.; Russina, O.; Triolo, A.; Kirchner, B. *ChemPhysChem* **2015**, *16*, 3325–3333.

[15] Brehm, M.; Weber, H.; Thomas, M.; Hollóczki, O.; Kirchner, B. *ChemPhysChem* **2015**, *16*, 3271–3277.

[16] Russina, O.; Lo Celso, F.; Di Michiel, M.; Passerini, S.; Appetecchi, G. B.; Castiglione, F.; Mele, A.; Caminitia, R.; Triolo, A. *Faraday Discuss.* **2013**, *167*, 499–513.

[17] Pereiro, A. B.; Pastoriza-Gallego, M. J.; Shimizu, K.; Marrucho, I. M.; Canongia Lopes, J. N.; Piñeiro, M. M.; Rebelo, L. P. N. *J. Phys. Chem. B* **2013**, *117*, 10826–10833.

[18] Zahn, S.; Uhlig, F.; Thar, J.; Spickermann, C.; Kirchner, B. *Angew. Chem.* **2008**, *120*, 3695–3697.

[19] Zahn, S.; Bruns, G.; Thar, J.; Kirchner, B. *Phys. Chem. Chem. Phys.* **2008**, *10*, 6921–6924.

[20] Zahn, S.; Kirchner, B. *J. Phys. Chem. A* **2008**, *112*, 8430–8435.

[21] Izgorodina, E. I.; Bernard, U. L.; MacFarlane, D. R. *J. Phys. Chem. A* **2009**, *113*, 7064–7072.

[22] Pensado, A. S.; Brehm, M.; Thar, J.; Seitsonen, A. P.; Kirchner, B. *ChemPhysChem* **2012**, *13*, 1845–1853.

[23] Grimme, S.; Hujo, W.; Kirchner, B. *Phys. Chem. Chem. Phys.* **2012**, *14*, 4875–4883.

[24] Malberg, F.; Pensado, A. S.; Kirchner, B. *Phys. Chem. Chem. Phys.* **2012**, *14*, 12079–12082.

[25] Gehrke, S.; von Domaros, M.; Clark, R.; Hollóczki, O.; Brehm, M.; Welton, T.; Luzar, A.; Kirchner, B. *Faraday Discuss.* **2017**, *206*, 219–245.

[26] Dupont, J. *Acc. Chem. Res.* **2011**, *44*, 1223–1231.

[27] Cooper, E. R.; Andrews, C. D.; Wheatley, P. S.; Webb, P. B.; Wormald, P.; Morris, R. E. *Nature* **2004**, *430*, 1012–1016.

[28] Seel, C.; Parham, A. H.; Safarowsky, O.; Hübner, G. M.; Vögtle, F. *J. Org. Chem.* **1999**, *64*, 7236–7242.

[29] Hübner, G. M.; Gläser, J.; Seel, C.; Vögtle, F. *Angew. Chem. Int. Ed.* **1999**, *38*, 383–386.

[30] Schalley, C. A.; Weilandt, T.; Brüggemann, J.; Vögtle, F. *Templates in Chemistry I*; Springer Berlin Heidelberg: Berlin, Heidelberg, 2004; pp 141–200.

[31] Cooper, E. R.; Andrews, C. D.; Wheatley, P. S.; Webb, P. B.; Wormald, P.; Morris, R. E. *Nature* **2004**, *430*, 1012–1016.

[32] Parnham, E. R.; Morris, R. E. *Acc. Chem. Res.* **2007**, *40*, 1005–1013.

[33] Freudenmann, D.; Wolf, S.; Wolff, M.; Feldmann, C. *Angew. Chem. Int. Ed.* **2011**, *50*, 11050–11060.

[34] Wolff, M.; Feldmann, C. *Z. Anorg. Allg. Chem.* **2009**, *635*, 1179–1186.

[35] Okrut, A.; Feldmann, C. *Z. Anorg. Allg. Chem.* **2006**, *632*, 409–412.

[36] Gaudet, M. V.; Peterson, D. C.; Zaworotko, M. J. *J. Incl. Phenom. Macrocycl. Chem.* **1988**, *6*, 425–428.

[37] Blanchard, L. A.; Brennecke, J. F. *Ind. Eng. Chem. Res.* **2001**, *40*, 287–292.

[38] Holbrey, J. D.; Reichert, W. M.; Nieuwenhuyzen, M.; Sheppard, O.; Hardacre, C.; Rogers, R. D. *Chem. Commun.* **2003**, 476–477.

[39] Freire, M. G.; Neves, C. M. S. S.; Carvalho, P. J.; Gardas, R. L.; Fernandes, A. M.; Marrucho, I. M.; Santos, L. M.; Coutinho, J. A. *J. Phys. Chem. B* **2007**, *111*, 13082–13089.

[40] Appetecchi, G. B.; Scaccia, S.; Tizzani, C.; Alessandrini, F.; Passerini, S. *J. Electrochem. Soc.* **2006**, *153*, A1685.

[41] Freire, M. G.; Carvalho, P. J.; Gardas, R. L.; Marrucho, I. M.; Santos, L. M.; Coutinho, J. A. *J. Phys. Chem. B* **2008**, *112*, 1604–1610.

[42] Jiao, T.; Zhuang, X.; He, H.; Zhao, L.; Li, C.; Chen, H.; Zhang, S. *Green Chem.* **2015**, *17*, 3783–3790.

[43] Othman, Z. S.; Hassan, N. H.; Zubairi, S. I. *Progress and Developments in Ionic Liquids*; IntechOpen, 2017.

[44] Mabaso, M. H.; Redhi, G. G.; Moodley, K. G. *S. Afr. J. Chem.* **2012**, *65*, 145–149.

[45] Ventura, S. P.; e Silva, F. A.; Quental, M. V.; Mondal, D.; Freire, M. G.; Coutinho, J. A. *Chem. Rev.* **2017**, *117*, 6984–7052.

[46] Han, D.; Row, K. H. *Molecules* **2010**, *15*, 2405–2426.

[47] Schröder, C. *Ionic Liquids II*; Springer, 2017; pp 127–152.

[48] Tian, J.; Fu, S.; Zhang, C.; Lucia, L. A. *BioResources* **2015**, *10*, 4099–4109.

[49] Sieffert, N.; Chaumont, A.; Wipff, G. *J. Phys. Chem. C* **2009**, *113*, 10610–10622.

[50] Vereycken, W.; Riaño, S.; Van Gerven, T.; Binnemans, K. *ACS Sust. Chem. Eng.* **2020**, *8*, 8223–8234.

[51] Vander Hoogerstraete, T.; Wellens, S.; Verachtert, K.; Binnemans, K. *Green Chem.* **2013**, *15*, 919–927.

[52] Hutter, J.; Curioni, A. *ChemPhysChem* **2005**, *6*, 1788–1793.

[53] Hutter, J.; Curioni, A. *Parallel Comput.* **2005**, *31*, 1–17.

[54] Plechkova, N. V.; Seddon, K. R. *Chem. Soc. Rev.* **2008**, *37*, 123–150.

[55] Zheng, W.; Mohammed, A.; Hines Jr, L. G.; Xiao, D.; Martinez, O. J.; Bartsch, R. A.; Simon, S. L.; Russina, O.; Triolo, A.; Quitevis, E. L. *J. Phys. Chem. B* **2011**, *115*, 6572–6584.

[56] Bhargava, B.; Balasubramanian, S.; Klein, M. L. *Chem. Commun.* **2008**, 3339–3351.

[57] Maginn, E. J. *J. Phys. Condens. Matter* **2009**, *21*, 373101.

[58] Kirchner, B. *Ionic liquids*; Springer, 2008; pp 213–262.

[59] Canongia Lopes, J. N.; Deschamps, J.; Pádua, A. A. *J. Phys. Chem. B* **2004**, *108*, 2038–2047.

[60] Canongia Lopes, J. N.; Pádua, A. A. *J. Phys. Chem. B* **2004**, *108*, 16893–16898.

[61] Pádua, A. A.; Costa Gomes, M. F.; Canongia Lopes, J. N. *Acc. Chem. Res.* **2007**, *40*, 1087–1096.

[62] Zhao, W.; Leroy, F.; Heggen, B.; Zahn, S.; Kirchner, B.; Balasubramanian, S.; Müller-Plathe, F. *J. Am. Chem. Soc.* **2009**, *131*, 15825–15833.

[63] Hollóczki, O.; Malberg, F.; Welton, T.; Kirchner, B. *Phys. Chem. Chem. Phys.* **2014**, *16*, 16880–16890.

[64] Kirchner, B.; Malberg, F.; Firaha, D. S.; Hollóczki, O. *J. Condens. Matter Phys.* **2015**, *27*, 463002.

[65] Gehrke, S.; Kirchner, B. *J. Chem. Eng. Data* **2019**, *65*, 1146–1158.

[66] Borodin, O.; Smith, G. D.; Henderson, W. *J. Phys. Chem. B* **2006**, *110*, 16879–16886.

[67] Lassègues, J.-C.; Grondin, J.; Talaga, D. *Phys. Chem. Chem. Phys.* **2006**, *8*, 5629–5632.

[68] Hardwick, L. J.; Holzapfel, M.; Wokaun, A.; Novák, P. *J. Raman Spectrosc.* **2007**, *38*, 110–112.

[69] Ray, P.; Vogl, T.; Balducci, A.; Kirchner, B. *J. Phys. Chem. B* **2017**, *121*, 5279–5292.

[70] Ray, P.; Balducci, A.; Kirchner, B. *J. Phys. Chem. B* **2018**, *122*, 10535–10547.

[71] Ray, P.; Balducci, A.; Kirchner, B. *J. Phys. Chem. B* **2019**, *123*, 2728–2728.

[72] Bühl, M.; Chaumont, A.; Schurhammer, R.; Wipff, G. *J. Phys. Chem. B* **2005**, *109*, 18591–18599.

[73] Bhargava, B. L.; Balasubramanian, S. *Chem. Phys. Lett.* **2006**, *417*, 486–491.

[74] Bhargava, B. L.; Balasubramanian, S. *J. Chem. Phys.* **2007**, *127*, 114510.

[75] Ghatee, M. H.; Ansari, Y. *J. Chem. Phys.* **2007**, *126*, 154502.

[76] Haskins, J. B.; Bauschlicher Jr, C. W.; Lawson, J. W. *J. Phys. Chem. B* **2015**, *119*, 14705–14719.

[77] Brehm, M.; Weber, H.; Pensado, A. S.; Stark, A.; Kirchner, B. *Phys. Chem. Chem. Phys.* **2012**, *14*, 5030–5044.

[78] Ingenmey, J.; Gehrke, S.; Kirchner, B. *ChemSusChem* **2018**, *11*, 1900–1910.

[79] Holloczki, O.; Firaha, D. S.; Friedrich, J.; Brehm, M.; Cybik, R.; Wild, M.; Stark, A.; Kirchner, B. *J. Phys. Chem. B* **2013**, *117*, 5898–5907.

[80] Firaha, D. S.; Kirchner, B. *J. Chem. Eng. Data* **2014**, *59*, 3098–3104.

[81] Firaha, D. S.; Kavalchuk, M.; Kirchner, B. *J. Solut. Chem.* **2015**, *44*, 838–849.

[82] Firaha, D. S.; Kirchner, B. *ChemSusChem* **2016**, *9*, 1591–1599.

[83] Thomas, M.; Brehm, M.; Kirchner, B. *Phys. Chem. Chem. Phys.* **2015**, *17*, 3207–3213.

[84] Blasius, J.; Elfgen, R.; Hollóczki, O.; Kirchner, B. *Phys. Chem. Chem. Phys.* **2020**, *22*, 10726–10737.

[85] Kirchner, B.; Blasius, J.; Alizadeh, V.; Gansäuer, A.; Hollóczki, O. *J. Phys. Chem. B* **2022**, *126*, 766–777.

[86] Brehm, M.; Kirchner, B. *J. Chem. Inf. Model.* **2011**, *51*, 2007–2023.

[87] Brehm, M.; Thomas, M.; Gehrke, S.; Kirchner, B. *J. Chem. Phys.* **2020**, *152*, 164105.

[88] Bedrov, D.; Piquemal, J.-P.; Borodin, O.; MacKerell Jr, A. D.; Roux, B.; Schröder, C. *Chemical reviews* **2019**, *119*, 7940–7995.

[89] Schödinger, E. *Ann. Phys.* **1926**, *79*, 361–376.

[90] Roothaan, C. C. J. *Rev. Mod. Phys.* **1951**, *23*, 69–89.

[91] Møller, C.; Plesset, M. S. *Phys. Rev.* **1934**, *46*, 618–622.

[92] Coester, F.; Kümmel, H. *Nucl. Phys.* **1960**, *17*, 477–485.

[93] Hohenberg, P.; Kohn, W. *Phys. Rev.* **1964**, *136*, B864.

[94] Kohn, W.; Sham, L. J. *Phys. Rev.* **1965**, *140*, A1133.

[95] Bloch, F. *Z. Phys.* **1929**, *52*, 555–600.

[96] Dirac, P. A. M. *Mathematical proceedings of the Cambridge philosophical society*; 1930; Vol. 26; pp 376–385.

[97] Metropolis, N.; Ulam, S. *J. Am. Stat. Assoc.* **1949**, *44*, 335–341.

[98] Metropolis, N.; Rosenbluth, A. W.; Rosenbluth, M. N.; Teller, A. H.; Teller, E. *J. Chem. Phys.* **1953**, *21*, 1087–1092.

[99] Vosko, S. H.; Wilk, L.; Nusair, M. *Can. J. Phys.* **1980**, *58*, 1200–1211.

[100] Slater, J. C. *Phys. Rev.* **1951**, *81*, 385.

[101] Becke, A. D. *Phys. Rev. A* **1988**, *38*, 3098.

[102] Lee, C.; Yang, W.; Parr, R. G. *Phys. Rev. B* **1988**, *37*, 785.

[103] Perdew, J. P.; Chevary, J. A.; Vosko, S. H.; Jackson, K. A.; Pederson, M. R.; Singh, D. J.; Fiolhais, C. *Phys. Rev. B* **1992**, *46*, 6671.

[104] Perdew, J. P.; Burke, K.; Ernzerhof, M. *Phys. Rev. Lett.* **1996**, *77*, 3865.

[105] Tao, J.; Perdew, J. P.; Staroverov, V. N.; Scuseria, G. E. *Phys. Rev. Lett.* **2003**, *91*, 146401.

[106] Becke, A. D. *J. Chem. Phys.* **1993**, *98*, 1372–1377.

[107] Stephens, P. J.; Devlin, F. J.; Chabalowski, C. F.; Frisch, M. J. *J. Phys. Chem.* **1994**, *98*, 11623–11627.

[108] Adamo, C.; Barone, V. *J. Chem. Phys.* **1999**, *110*, 6158–6170.

[109] Staroverov, V. N.; Scuseria, G. E.; Tao, J.; Perdew, J. P. *J. Chem. Phys.* **2003**, *119*, 12129–12137.

[110] Langreth, D. C.; Dion, M.; Rydberg, H.; Schröder, E.; Hyldgaard, P.; Lundqvist, B. I. *Int. J. Quantum Chem.* **2005**, *101*, 599–610.

[111] Sato, T.; Tsuneda, T.; Hirao, K. *Mol. Phys.* **2005**, *103*, 1151–1164.

[112] Von Lilienfeld, O. A.; Tavernelli, I.; Rothlisberger, U.; Sebastiani, D. *Phys. Rev. Lett.* **2004**, *93*, 153004.

[113] Sun, Y. Y.; Kim, Y.-H.; Lee, K.; Zhang, S. B. *J. Chem. Phys.* **2008**, *129*, 154102.

[114] Grimme, S. *J. Comput. Chem.* **2006**, *27*, 1787–1799.

[115] Grimme, S.; Antony, J.; Ehrlich, S.; Krieg, H. *J. Chem. Phys.* **2010**, *132*, 154104.

[116] Grimme, S.; Ehrlich, S.; Goerigk, L. *J. Comput. Chem.* **2011**, *32*, 1456–1465.

[117] Newton, I. *Philosophiae naturalis principia mathematica. Editio ultima.*; 1726.

[118] Alder, B. J.; Wainwright, T. E. *J. Chem. Phys.* **1957**, *27*, 1208–1209.

[119] Alder, B. J.; Wainwright, T. E. *J. Chem. Phys.* **1959**, *31*, 459–466.

[120] Alder, B. J.; Wainwright, T. E. *J. Chem. Phys.* **1960**, *33*, 1439–1451.

[121] Rahman, A. *Phys. Rev.* **1964**, *136*, 405–411.

[122] Verlet, L. *Phys. Rev.* **1967**, *159*, 98–103.

[123] Verlet, L. *Phys. Rev.* **1968**, *165*, 201–214.

[124] Nicolas, J. J.; Gubbins, K. E.; Streett, W. B.; Tildesley, D. J. *Mol. Phys.* **1979**, *37*, 1429–1454.

[125] Allen, M. P.; Tildesley, D. J. *Computer simulation of liquids*; Oxford university press, 1987.

[126] Van Gunsteren, W. F.; Berendsen, H. J. C. *Angew. Chem. Int. Ed.* **1990**, *29*, 992–1023.

[127] Jensen, F. *Introduction to computational chemistry*; John wiley & sons, 1999.

[128] Frenkel, D.; Smit, B. *Understanding molecular simulation: from algorithms to applications*; Elsevier, 2006; Vol. 1.

[129] Hülsmann, M. *Effiziente und neuartige Verfahren zur Optimierung von Kraftfeldparametern bei atomistischen Molekularen Simulationen kondensierter Materie*; Fraunhofer Verlag, 2012.

[130] Marx, D.; Hutter, J. *Ab initio molecular dynamics: basic theory and advanced methods*; Cambridge University Press, 2009.

[131] Hockney, R. W. *Methods Comput. Phys.* **1970**, *9*, 136–211.

[132] Potter, D. *An Introduction to Computational Physics*; John Wiley, London, 1972.

[133] Swope, W. C.; Andersen, H. C.; Berens, P. H.; Wilson, K. R. *J. Chem. Phys.* **1982**, *76*, 637–649.

[134] Lennard-Jones, J. E. *Proc. Phys. Soc.* **1931**, *43*, 461–483.

[135] Lorentz, H. A. *Ann. Phys.* **1881**, *248*, 127–136.

[136] Berthelot, D. *Compt. Rendus* **1898**, *126*, 1703–1706.

[137] Morse, P. M. *Phys. Rev.* **1929**, *34*, 57.

[138] Buckingham, R. A. *Proc. R. Soc. Lond. A Math. Phys. Sci.* **1938**, *168*, 264–283.

[139] de Coulomb, C. A. *Histoire de l'Académie Royale des Sciences* **1785**, 569–577.

[140] Breneman, C. M.; Wiberg, K. B. *J. Comput. Chem.* **1990**, *11*, 361–373.

[141] Weiner, S. J.; Kollman, P. A.; Case, D. A.; Singh, U. C.; Ghio, C.; Alagona, G.; Profeta, S.; Weiner, P. *J. Am. Chem. Soc.* **1984**, *106*, 765–784.

[142] Jorgensen, W. L.; Maxwell, D. S.; Tirado-Rives, J. *J. Am. Chem. Soc.* **1996**, *118*, 11225–11236.

[143] Kaminski, G.; Jorgensen, W. L. *J. Phys. Chem.* **1996**, *100*, 18010–18013.

[144] Plimpton, S. *J. Comput. Phys.* **1995**, *117*, 1–19.

[145] Car, R.; Parrinello, M. *Phys. Rev. Lett.* **1985**, *55*, 2471.

[146] Payne, M. C.; Joannopoulos, J. D.; Allan, D. C.; Teter, M. P.; Vanderbilt, D. H. *Phys. Rev. Lett.* **1986**, *56*, 2656.

[147] Arias, T. A.; Payne, M.; Joannopoulos, J. *Phys. Rev. Lett.* **1992**, *69*, 1077.

[148] Payne, M. C.; Teter, M. P.; Allan, D. C.; Arias, T.; Joannopoulos, a. J. *Rev. Mod. Phys.* **1992**, *64*, 1045.

[149] Clarke, L. J.; Štich, I.; Payne, M. C. *Comput. Phys. Commun.* **1992**, *72*, 14–28.

[150] Bolton, K.; Hase, W. L.; Peslherbe, G. H. *Modern Methods for Multidimensional Dynamics Computations in Chemistry*; World Scientific, 1998; pp 143–189.

[151] Tuckerman, M. E. *J. Condens. Matter Phys.* **2002**, *14*, R1297.

[152] CP2k developers group under the terms of the GNU General Public License; see `http://www.cp2k.org`.

[153] Lippert, G.; Hutter, J.; Parrinello, M. *Mol. Phys.* **1997**, *92*, 477–488.

[154] VandeVondele, J.; Krack, M.; Mohamed, F.; Parrinello, M.; Chassaing, T.; Hutter, J. *Comput. Phys. Commun.* **2005**, *167*, 103–128.

[155] Goedecker, S.; Teter, M.; Hutter, J. *Phys. Rev. B* **1996**, *54*, 1703–1710.

[156] Hartwigsen, C.; Goedecker, S.; Hutter, J. *Phys. Rev. B* **1998**, *58*, 3641–3662.

[157] Krack, M. *Theor. Chem. Acc.* **2005**, *114*, 145–152.

[158] VandeVondele, J.; Hutter, J. *J. Chem. Phys.* **2003**, *118*, 4365–4369.

[159] Hestenes, M. R.; Stiefel, E. *Methods of conjugate gradients for solving linear systems*; NBS Washington, DC, 1952; Vol. 49.

[160] Pulay, P. *J. Comput. Chem.* **1982**, *3*, 556–560.

[161] McQuarrie, D. A. *Statistical Mechanics*; University Science Books, 2000.

[162] Brehm, M.; Weber, H.; Pensado, A. S.; Stark, A.; Kirchner, B. *Z. Phys. Chem.* **2013**, *227*, 177–204.

[163] Gehrke, S.; Hollóczki, O. *Chem. Eur. J.* **2018**, *24*, 11594–11604.

[164] Elfgen, R.; Hollóczki, O.; Kirchner, B. *Acc. Chem. Res.* **2017**, *50*, 2949–2957.

[165] Humphrey, W.; Dalke, A.; Schulten, K. *J. Mol. Graph. Model.* **1996**, *14*, 33–38.

[166] Voronoi, G. *J. für Reine Angew. Math.* **1908**, *1908*, 198–287.

[167] Gellatly, B.; Finney, J. L. *J. Mol. Biol.* **1982**, *161*, 305–322.

[168] Rycroft, C. *Voro++: A three-dimensional Voronoi cell library in C++*; 2009.

[169] Bondi, A. v. *J. Phys. Chem.* **1964**, *68*, 441–451.

[170] Rowland, R. S.; Taylor, R. *J. Phys. Chem.* **1996**, *100*, 7384–7391.

[171] Mantina, M.; Chamberlin, A. C.; Valero, R.; Cramer, C. J.; Truhlar, D. G. *J. Phys. Chem. A* **2009**, *113*, 5806–5812.

[172] Thomas, M.; Brehm, M.; Fligg, R.; Vöhringer, P.; Kirchner, B. *Phys. Chem. Chem. Phys.* **2013**, *15*, 6608–6622.

[173] Thomas, M.; Brehm, M.; Hollóczki, O.; Kelemen, Z.; Nyulászi, L.; Pasinszki, T.; Kirchner, B. *J. Chem. Phys.* **2014**, *141*, 024510.

[174] Thomas, M.; Kirchner, B. *J. Phys. Chem. Lett.* **2016**, *7*, 509–513.

[175] Ma, Z.; Yu, J.; Dai, S. *Adv. Mater.* **2010**, *22*, 261–285.

[176] Reichardt, C.; Welton, T. *Solvents and solvent effects in organic chemistry*; John Wiley & Sons, 2011.

[177] Volkov, S. *Chem. Soc. Rev.* **1990**, *19*, 21–28.

[178] Afanasiev, P.; Geantet, C. *Coord. Chem. Rev.* **1998**, *178*, 1725–1752.

[179] Adams, C. J.; Bradley, A. E.; Seddon, K. R. *Aust. J. Chem.* **2001**, *54*, 679–681.

[180] Reichert, W. M.; Holbrey, J. D.; Vigour, K. B.; Morgan, T. D.; Broker, G. A.; Rogers, R. D. *Chem. Commun.* **2006**, 4767–4779.

[181] Morris, R. E. *Chem. Commun.* **2009**, 2990–2998.

[182] Ma, Z.; Yu, J.; Dai, S. *Adv. Mater.* **2010**, *22*, 261–285.

[183] Mudring, A.-V.; Tang, S. *Eur. J. Inorg. Chem.* **2010**, *2010*, 2569–2581.

[184] Taubert, A. In *Ionic Liquids*; Kirchner, B., Ed.; Springer Berlin Heidelberg, 2010; pp 127–159.

[185] Ahmed, E.; Ruck, M. *Coord. Chem. Rev* **2011**, *255*, 2892–2903.

[186] Vollmer, C.; Janiak, C. *Coord. Chem. Rev.* **2011**, *255*, 2039–2057.

[187] Ahmed, E.; Breternitz, J.; Groh, M. F.; Ruck, M. *CrystEngComm* **2012**, *14*, 4874–4885.

[188] Groh, M. F.; Wolff, A.; Grasser, M. A.; Ruck, M. *Int. J. Mol. Sci.* **2016**, *17*, 1452.

[189] Santner, S.; Heine, J.; Dehnen, S. *Angew. Chem. Int. Ed.* **2016**, *55*, 876–893.

[190] Gao, M.-R.; Yuan, J.; Antonietti, M. *Chem. Eur. J.* **2017**, *23*, 5391–5403.

[191] Welton, T. *Chem. Rev.* **1999**, *99*, 2071–2083.

[192] Rogers, R. D.; Seddon, K. R. *Science* **2003**, *302*, 792–793.

[193] Brennecke, J. F.; Rogers, R. D.; Seddon, K. R. *Ionic liquids IV. Not just solvents anymore.*; American Chemical Society: Washington, 2007.

[194] Hayes, R.; Warr, G. G.; Atkin, R. *Chem. Rev.* **2015**, *115*, 6357–6426.

[195] Bates, E.; Mayton, R.; Ntai, I.; Davis, J. *J. Am. Chem. Soc.* **2002**, *124*, 926–927.

[196] Cremer, T.; Kolbeck, C.; Lovelock, K.; Paape, N.; Wölfel, R.; Schulz, P.; Wasserscheid, P.; Weber, H.; Thar, J.; Kirchner, B.; Maier, F.; Steinrück, H.-P. *Chem. Eur. J.* **2010**, *16*, 9018–9033.

[197] McLean, B.; Li, H.; Stefanovic, R.; Wood, R. J.; Webber, G. B.; Ueno, K.; Watanabe, M.; Warr, G. G.; Page, A.; Atkin, R. *Phys. Chem. Chem. Phys.* **2015**, *17*, 325–333.

[198] Welton, T. *Green Chem.* **2011**, *13*, 225–225.

[199] Rabenau, A.; Rau, H.; Rosenstein, G. *Angew. Chem. Int. Ed.* **1970**, *9*, 802–803.

[200] Groh, M. F.; Mueller, U.; Ahmed, E.; Rothenberger, A.; Ruck, M. *Z. Naturforsch. B* **2013**, *68*, 1108–1122.

[201] Ahmed, E.; Beck, J.; Daniels, J.; Doert, T.; Eck, S. J.; Heerwig, A.; Isaeva, A.; Lidin, S.; Ruck, M.; Schnelle, W.; Stankowski, A. *Angew. Chem.* **2012**, *124*, 8230–8233.

[202] Ahmed, E.; Beck, J.; Daniels, J.; Doert, T.; Eck, S. J.; Heerwig, A.; Isaeva, A.; Lidin, S.; Ruck, M.; Schnelle, W.; Stankowski, A. *Angew. Chem. Int. Ed.* **2012**, *51*, 8106–8109.

[203] Ahmed, E.; Ahrens, E.; Heise, M.; Ruck, M. *Z. Anorg. Allg. Chem.* **2010**, *636*, 2602–2606.

[204] Schulz, C.; Daniels, J.; Bredow, T.; Beck, J. *Angew. Chem.* **2016**, *128*, 1188–1192.

[205] Schulz, C.; Daniels, J.; Bredow, T.; Beck, J. *Angew. Chem. Int. Ed.* **2016**, *55*, 1173–1177.

[206] Freudenmann, D.; Feldmann, C. *Z. Anorg. Allgem. Chem.* **2011**, *637*, 1481–1485.

[207] Couch, T. W.; Lokken, D. A.; Corbett, J. D. *Inorg. Chem.* **1972**, *11*, 357–362.

[208] Martinez, J. M.; Martinez, L. *J. Comput. Chem.* **2003**, *24*, 819–825.

[209] Martinez, L.; Andrade, R.; Birgin, E. G.; Martinez, J. M. *J. Comput. Chem.* **2009**, *30*, 2157–2164.

[210] VandeVondele, J.; Hutter, J. *J. Chem. Phys.* **2007**, *127*, 114105.

[211] Nosé, S. *J. Chem. Phys.* **1984**, *81*, 511–519.

[212] Hoover, W. G. *Phys. Rev. A* **1985**, *31*, 1695–1697.

[213] Gu, Z.; Brennecke, J. F. *J. Chem. Eng. Data* **2002**, *47*, 339–345.

[214] N. Yoshida, H. S. F. H., R. Ishizuka *J. Phys. Chem.* **2016**, *110*, 8451–8458.

[215] J. Urquidi, S. S. G. R., C.H. Cho *J. Mol. Struc.* **1999**, *485-486*, 363–371.

[216] Kirchner, B.; Ermakova, E.; Solca, J.; Huber, H. *Chem. Eur. J.* **1998**, *4*, 383–388.

[217] Solca, J.; Dyson, A. J.; Steinebrunner, G.; Kirchner, B.; Huber, H. *J. Chem. Phys.* **1998**, *108*, 4107–4111.

[218] Eichkorn, K.; Treutler, O.; Öhm, H.; Häser, M.; Ahlrichs, R. *Chem. Phys. Lett.* **1995**, *242*, 652–660.

[219] Neese, F. *WIREs Comput. Mol. Sci.* **2012**, *2*, 73–78.

[220] Weigend, F.; Ahlrichs, R. *Phys. Chem. Chem. Phys.* **2005**, *7*, 3297–3305.

[221] Grimme, S.; Brandenburg, J.; Bannwarth, C.; Hansen, A. *J. Chem. Phys.* **2015**, *143*, 054107.

[222] H.Kruse,; Grimme, S. *J.Chem.Phys.* **2016**, *136*, 154101.

[223] GNUPLOT, http://www.gnuplot.info/.

[224] XMGRACE, http://plasma-gate.weizmann.ac.il/Grace/.

[225] Russina, O.; Triolo, A. *Faraday Discuss.* **2012**, *154*, 97–109.

[226] Santos, C. S.; Annapureddy, H. V. R.; Murthy, N. S.; Kashyap, H. K.; Castner, E. W.; Margulis, C. J. *J. Chem. Phys.* **2011**, *134*, 064501.

[227] Kirchner, B.; Seitsonen, A. P. *Inorg. Chem.* **2007**, *46*, 2751–2754.

[228] Øye, H. A.; Jagtoyen, M.; Oksefjell, T.; Wilkes, J. *Mater. Sci. Forum* **1991**, *73*, 183–190.

[229] Hallett, J. P.; Liotta, C. L.; Ranieri, G.; Welton, T. *J. Org. Chem.* **2009**, *74*, 1864–1868.

[230] Lui, M. Y.; Crowhurst, L.; Hallett, J. P.; Hunt, P. A.; Niedermeyer, H.; Welton, T. *Chem. Sci.* **2011**, *2*, 1491–1496.

[231] Buenker, R. J.; Peyerimhoff, S. D. *Chem. Rev.* **1974**, *74*, 127–188.

[232] Beck, J. *Coord. Chem. Rev.* **1997**, *163*, 55–70.

[233] Canongia Lopes, J. N.; Costa Gomes, M. F.; Pádua, A. A. H. *J. Phys. Chem. B* **2006**, *110*, 16816–16818.

[234] Roth, C.; Appelhagen, A.; Jobst, N.; Ludwig, R. *ChemPhysChem* **2012**, *13*, 1708–1717.

[235] Shimomura, T.; Fujii, K.; Takamuku, T. *Phys. Chem. Chem. Phys.* **2010**, *12*, 12316–12324.

[236] Vaz, I. C. M.; Bhattacharjee, A.; Rocha, M. A. A.; Coutinho, J. A. P.; Bastos, M.; Santos, L. M. N. B. F. *Phys. Chem. Chem. Phys.* **2016**, *18*, 19267–19275.

[237] Seddon, K. R. *J. Chem. Tech. Biotechnol.* **1997**, *68*, 351–356.

[238] Firaha, D. S.; Thomas, M.; Hollóczki, O.; Korth, M.; Kirchner, B. *J. Chem. Phys.* **2016**, *145*, 204502.

[239] Welton, T. *Coord. Chem. Rev.* **2004**, *248*, 2459–2477.

[240] Plechkova, N. V.; Seddon, K. R. *Chem. Soc. Rev.* **2008**, *37*, 123–150.

[241] Maginn, E. J. *J. Phys. Condes. Matter* **2009**, *21*, 373101.

[242] Canongia Lopes, J. N.; Pádua, A. A. H. *J. Chem. Phys. B* **2006**, *110*, 16816–16818.

[243] Spickermann, C.; Felder, T.; Schalley, C. A.; Kirchner, B. *Chem. Eur. J.* **2008**, *14*, 1216–1227.

[244] Maginn, E. J. *Acc. Chem. Res.* **2007**, *40*, 1200–1207.

[245] Mitrano, D. *Nat. Nanotechnol.* **2019**, *14*, 299.

[246] Lehner, R.; Weder, C.; Petri-Fink, A.; Rothen-Rutishauser, B. *Environ. Sci. Technol.* **2019**, *53*, 1748–1765.

[247] Thompson, R. C.; Olsen, Y.; Mitchell, R. P.; Davis, A.; Rowland, S. J.; John, A. W.; McGonigle, D.; Russell, A. E. *Science* **2004**, *304*, 838–838.

[248] Li, J.; Qu, X.; Su, L.; Zhang, W.; Yang, D.; Kolandhasamy, P.; Li, D.; Shi, H. *Environ. Pollut.* **2016**, *214*, 177–184.

[249] Bellas, J.; Martínez-Armental, J.; Martínez-Cámara, A.; Besada, V.; Martínez-Gómez, C. *Mar. Pollut. Bull.* **2016**, *109*, 55–60.

[250] Collard, F.; Gilbert, B.; Eppe, G.; Parmentier, E.; Das, K. *Arch. Environ. Contam. Toxicol.* **2015**, *69*, 331–339.

[251] Lusher, A.; Mchugh, M.; Thompson, R. *Mar. Pollut. Bull.* **2013**, *67*, 94–99.

[252] Lusher, A. L.; Hernandez-Milian, G.; O'Brien, J.; Berrow, S.; O'Connor, I.; Officer, R. *Environ. Pollut.* **2015**, *199*, 185–191.

[253] Kim, J.-S.; Lee, H.-J.; Kim, S.-K.; Kim, H.-J. *Environ. Sci. Technol.* **2018**, *52*, 12819–12828.

[254] Alimi, O. S.; Farner Budarz, J.; Hernandez, L. M.; Tufenkji, N. *Environ. Sci. Technol.* **2018**, *52*, 1704–1724.

[255] Oriekhova, O.; Stoll, S. *Environ. Sci. Nano* **2018**, *5*, 792–799.

[256] Bordós, G.; Urbányi, B.; Micsinai, A.; Kriszt, B.; Palotai, Z.; Szabó, I.; Hantosi, Z.; Szoboszlay, S. *Chemosphere* **2019**, *216*, 110–116.

[257] Al-Jaibachi, R.; Cuthbert, R. N.; Callaghan, A. *Biol. Lett.* **2018**, *14*, 20180479.

[258] Choy, C. A.; Robison, B. H.; Gagne, T. O.; Erwin, B.; Firl, E.; Halden, R. U.; et. al., *Scientific reports* **2019**, *9*, 1–9.

[259] Piccardo, M.; Renzi, M.; Terlizzi, A. *Marine Poll. Bull.* **2020**, *157*, 111317.

[260] Triebskorn, R.; Braunbeck, T.; Grummt, T.; Hanslik, L.; Huppertsberg, S.; Jekel, M.; et. al., *Trends Analyt. Chem.* **2019**, *110*, 375–392.

[261] Geyer, R.; Jambeck, J. R.; Law, K. L. *Sci. Adv.* **2017**, *3*, e1700782.

[262] Zhang, W.; Dong, Z.; Zhu, L.; Hou, Y.; Qiu, Y. *ACS Nano* **2020**,

[263] Hernandez, L. M.; Yousefi, N.; Tufenkji, N. *Environ. Sci. Technol. Lett.* **2017**, *4*, 280–285.

[264] Dawson, A. L.; Kawaguchi, S.; King, C. K.; Townsend, K. A.; King, R.; Huston, W. M.; Bengtson Nash, S. M. *Nat. Commun.* **2018**, *9*, 1001.

[265] Van Cauwenberghe, L.; Claessens, M.; Vandegehuchte, M. B.; Janssen, C. R. *Environ. Pollut.* **2015**, *199*, 10–17.

[266] Watermann, B.; Löder, M.; Herlyn, M.; Daehne, B.; Thomsen, A.; Gall, K. *Environ. Sci. Pollut. Res.* **2017**, *24*, 3352–3362.

[267] Kühn, S.; Van Werven, B.; Van Oyen, A.; Meijboom, A.; Rebolledo, E. L. B.; Van Franeker, J. A. *Mar. Pollut. Bull.* **2017**, *115*, 86–90.

[268] Zhao, S.; Zhu, L.; Li, D. *Sci. Total Environ.* **2016**, *550*, 1110–1115.

[269] Lwanga, E. H.; Vega, J. M.; Quej, V. K.; de los Angeles Chi, J.; del Cid, L. S.; Chi, C.; Segura, G. E.; Gertsen, H.; Salánki, T.; van der Ploeg, M. *Sci. Rep.* **2017**, *7*, 14071.

[270] Brun, N. R.; van Hage, P.; Hunting, E. R.; Haramis, A.-P. G.; Vink, S. C.; Vijver, M. G.; Schaaf, M. J.; Tudorache, C. *Commun. Biol.* **2019**, *2*, 382.

[271] Hollóczki, O.; Gehrke, S. *Sci. Rep.* **2019**, *9*, 16013.

[272] Hollóczki, O. *Int. J. Quantum Chem.* **2020**, *120*, e26372.

[273] Kihara, S.; van der Heijden, N. J.; Seal, C. K.; Mata, J. P.; Whitten, A. E.; Köper, I.; McGillivray, D. J. *Bioconjug. Chem.* **2019**, *30*, 1067–1076.

[274] Gopinath, P. M.; Saranya, V.; Vijayakumar, S.; Meera, M. M.; Ruprekha, S.; Kunal, R.; Pranay, A.; Thomas, J.; Mukherjee, A.; Chandrasekaran, N. *Sci. Rep.* **2019**, *9*, 8860.

[275] Wang, S.; Liu, M.; Wang, J.; Huang, J.; Wang, J. *Marine Poll. Bull.* **2020**, *158*, 111403.

[276] Machado, M. C.; Vimbela, G. V.; Silva-Oliveira, T. T.; Bose, A.; Tripathi, A. *PloS one* **2020**, *15*, e0232745.

[277] Prüst, M.; Meijer, J.; Westerink, R. H. *Part. Fibre Toxicol.* **2020**, *17*, 1–16.

[278] Brun, N. R.; Beenakker, M. M.; Hunting, E. R.; Ebert, D.; Vijver, M. G. *Nanotoxicology* **2017**, *11*, 1059–1069.

[279] Hollóczki, O.; Gehrke, S. *ChemPhysChem* **2020**, *21*, 9–12.

[280] Bochicchio, D.; Panizon, E.; Monticelli, L.; Rossi, G. *Sci. Rep.* **2017**, *7*, 6357.

[281] Sözener, Z. C.; Cevhertas, L.; Nadeau, K.; Akdis, M.; Akdis, C. A. *J. Allergy Clin. Immunol.* **2020**, *145*, 1517–1528.

[282] Zhang, Q.; Xu, E. G.; Li, J.; Chen, Q.; Ma, L.; Zeng, E. Y.; Shi, H. *Environ. Sci. Technol.* **2020**, *54*, 3740–3751.

[283] Cox, K. D.; Covernton, G. A.; Davies, H. L.; Dower, J. F.; Juanes, F.; Dudas, S. E. *Environ. Sci. Technol.* **2019**, *53*, 7068–7074.

[284] Hernandez, L. M.; Xu, E. G.; Larsson, H. C.; Tahara, R.; Maisuria, V. B.; Tufenkji, N. *Environ. Sci. Technol.* **2019**, *53*, 12300–12310.

[285] Nguyen, B.; Claveau-Mallet, D.; Hernandez, L. M.; Xu, E. G.; Farner, J. M.; Tufenkji, N. *Acc. Chem. Res.* **2019**, *52*, 858–866.

[286] Xiong, Y.; Zhao, J.; Li, L.; Wang, Y.; Dai, X.; Yu, F.; Ma, J. *Water Res.* **2020**, 116100.

[287] Hildebrandt, L.; Mitrano, D. M.; Zimmermann, T.; Pröfrock, D. *Front. Environ. Sci.* **2020**, *8*, 89.

[288] Ming, W.; Zhao, J.; Lu, X.; Wang, C.; Fu, S. *Macromolecules* **1996**, *29*, 7678–7682.

[289] Berendsen, H.; Grigera, J.; Straatsma, T. *J. Phys. Chem.* **1987**, *91*, 6269–6271.

[290] Good, R. J.; Hope, C. J. *J. Chem. Phys.* **1970**, *53*, 540–543.

[291] Nosé, S. *Mol. Phys.* **1984**, *52*, 255–268.

[292] Martyna, G. J.; Klein, M. L.; Tuckerman, M. *J. Chem. Phys.* **1992**, *97*, 2635–2643.

[293] Yoshida, S.; Hiraga, K.; Takehana, T.; Taniguchi, I.; Yamaji, H.; Maeda, Y.; Toyohara, K.; Miyamoto, K.; Kimura, Y.; Oda, K. *Science* **2016**, *351*, 1196–1199.

[294] Yang, J.; Yang, Y.; Wu, W.-M.; Zhao, J.; Jiang, L. *Environ. Sci. Technol.* **2014**, *48*, 13776–13784.

[295] Dimarogona, M.; Nikolaivits, E.; Kanelli, M.; Christakopoulos, P.; Sandgren, M.; Topakas, E. *Biochim. Biophys. Acta* **2015**, *1850*, 2308–2317.

[296] Ding, J.; Huang, Y.; Liu, S.; Zhang, S.; Zou, H.; Wang, Z.; Zhu, W.; Geng, J. *J. Hazard. Mat.* **2020**, 122693.

[297] Ma, Y.; Huang, A.; Cao, S.; Sun, F.; Wang, L.; Guo, H.; Ji, R. *Environ. Poll.* **2016**, *219*, 166–173.

[298] Bruce, W., Duncan; Cabry, P., Christopher; Lopes, N. C., José; Costen, M. L.; D'Andrea, L. a.; et al., *J. Phys. Chem. B* **2017**, *121*, 6002–6020.

[299] Xia, Y.; Zhou, J.-J.; Gong, Y.-Y.; Li, Z.-J.; Zeng, E. Y. *Environ. Poll.* **2020**, 115061.

[300] Rowenczyk, L.; Dazzi, A.; Deniset-Besseau, A.; Beltran, V.; Goudounèche, D.; et al., *Environ. Sci. Technol.* **2020**, *54*, 4102–4109.

[301] Bianco, A.; Sordello, F.; Ehn, M.; Vione, D.; Passananti, M. *Sci. Total Environ.* **2020**, 140413.

[302] Kelkar, V. P.; Rolsky, C. B.; Pant, A.; Green, M. D.; Tongay, S.; Halden, R. U. *Water Res.* **2019**, *163*, 114871.

[303] Tariq, M.; Carvalho, P. J.; Coutinho, J. A.; Marrucho, I. M.; Canongia Lopes, J. N.; Rebelo, L. P. *Fluid Ph. Equil.* **2011**, *301*, 22–32.

[304] Seddon, K. R.; Stark, A. S.; Torres, M. J. *ACS Symp. Ser.* **2004**, *819*, 34–49.

[305] Kirchner, B.; Hollóczki, O.; Canongia Lopes, J. N.; Pádua, A. A. H. *WIREs: Comp. Mol. Sci.* **2015**, *5*, 202–214.

[306] Weber, H.; Hollóczki, O.; Pensado, A. S.; Kirchner, B. *J. Chem. Phys.* **2013**, *139*, 084502.

[307] Sieffert, N.; Wipff, G. *J. Phys. Chem. B* **2006**, *110*, 13076–13085.

[308] Nishi, N.; Uruga, T.; Tanida, H. *J. Electroanal. Chem.* **2015**, *759*, 129–136.

[309] Chevrot, G.; Schurhammer, R.; Wipff, G. *Phys. Chem. Chem. Phys.* **2006**, *8*, 4166–4174.

[310] Chaumont, A.; Schurhammer, R.; Wipff, G. *J. Phys. Chem. B* **2005**, *109*, 18964–18973.

[311] Lorentz, H. *Ann. Phys.* **1881**, *248*, 660–661.

[312] Schaftenaar, G.; Noordik, J. H. *J. Comput.-Aided Mol. Design* **2000**, *14*, 123–134.

[313] Paduszynski, K.; Domanska, U. *Ind. Eng. Chem. Res.* **2011**, *51*, 591–604.

# Acknowledgements

At this point I would like to thank everyone who has supported me during the five years of my doctoral studies and thus enabled the completion of my doctorate:

My biggest thanks go to my doctor's mother, Prof. Dr. Barbara Kirchner, first of all for sharing your overwhelming scientific expertise and experiences with me, and for the opportunity to participate in studying such interesting topics like ionic liquids, while providing room to develop own ideas in a very pleasant working atmosphere. You always have an open ear for scientific and personal problems, even during stressful times, which I appreciate a lot and which cannot be taken for granted at all.

Also many thanks to Dr. Oldamur Hollóczki, for your great scientific expertise and for giving me the chance to participate in your interesting and up-to-date research about the global plastics contamination.

A special "thank you" goes to my coworkers from the Kirchner group and also from the whole Theoretical Chemistry Institute. We had a great time together, especially during our lunch breaks, in the social rooms and on the roof terrace of the Mulliken Center, including numerous fruitful and motivating scientific discussions and reciprocal support, and also a lot of fun. I will never forget it.

Many thanks go to the Max Planck Society, in particular the Institutes for Chemical Energy Conversion and Coal Research in Mülheim an der Ruhr, for financing three years of my doctorate time via the International Max Planck Research School on Reactive Structure Analysis for Chemical Reactions (IMPRS-RECHARGE), thereby giving me the opportunity to network with other young scientists and institutions and to learn about a multitude of fascinating research topics.

For the other two years of my doctoral studies I would like to thank the Priority Programme SPP 1708 titled "Material Synthesis near Room Temperature", established

by the German Research Foundation (DFG) and initiated by the group around Professor Michael Ruck, as well as the joint project “LuCaMag: Pathways to secondary Mg/Ca air batteries”, founded by the Federal Ministry of Education and Research (BMBF), for financial support.

Last but not least I want to thank my family, partner and friends for always and unconditionally giving me a strong backing through all of these years. I love you.

# Publications

Publications that represent the basis of this thesis:

1. **R. Elfgen**, O. Hollóczki, P. Ray, M. F. Groh, M. Ruck and B. Kirchner, *Theoretical Investigation of the $Te_4Br_2$ Molecule in Ionic Liquids*, Z. Anorg. Allg. Chem. (2017) 643, 41–52.
   DOI: 10.1002/zaac.201600342

2. **R. Elfgen**, O. Hollóczki and B. Kirchner, *A Molecular Level Understanding of Template Effects in Ionic Liquids*, Acc. Chem. Res. (2017), 50, 2949–2957.
   DOI: 10.1021/acs.accounts.7b00436

3. **R. Elfgen**, S. Gehrke and O. Hollóczki, *Ionic Liquids as Extractants for Nanoplastics*, ChemSusChem (2020) 13, 5449–5459.
   DOI: 10.1002/cssc.202001749

Further publications:

- R. Macchieraldo, L. Esser, **R. Elfgen**, P. Voepel, S. Zahn, B. M. Smarsly and B. Kirchner, *Hydrophilic Ionic Liquid Mixtures of Weakly and Strongly Coordinating Anions with and without Water*, ACS Omega (2018), 3, 8567–8582.
  DOI: 10.1021/acsomega.8b00995

- P. Ray, **R. Elfgen** and B. Kirchner, *Cation influence on heterocyclic ammonium ionic liquids: a molecular dynamics study*, Phys. Chem. Chem. Phys. (2019), 21, 4472–4486.
  DOI: 10.1039/C8CP07683A

- J. Blasius, **R. Elfgen**, O. Hollóczki and B. Kirchner, *Glucose in dry and moist ionic liquid: Vibrational circular dichroism, IR, and possible mechanisms*, Phys. Chem.

Chem. Phys. (2020), 22, 10726–10737.
DOI: 10.1039/C9CP06798A

- L. Esser, R. Macchieraldo, **R. Elfgen**, M. Sieland, B. Smarsly and B. Kirchner, *$TiCl_4$ Dissolved in Ionic Liquids from Ab Initio Molecular Dynamics Simulations*, Molecules (2021), 26, 79.
  DOI: 10.3390/molecules26010079

- A. Szabadi, **R. Elfgen**, R. Macchieraldo, F. L. Kearns, H. L. Woodcock, B. Kirchner and C. Schröder, *Comparison between ab initio and polarizable molecular dynamics simulations of 1-butyl-3-methylimidazolium tetrafluoroborate and chloride in water*, J. Mol. Liq. (2021), 337, 116521.
  DOI: 10.1016/j.molliq.2021.116521

- S. Taherivardanjani, **R. Elfgen**, W. Reckien, E. Suarez, E. Perlt and B. Kirchner, *Benchmarking the computational costs and quality of vibrational spectra from ab initio simulations*, Adv. Theory Simul. (2022), 5, 2100293.
  DOI: 10.1002/adts.202100293